eman ta zabal zazu

Universidad del País Vasco
Euskal Herriko Unibertsitatea

SPIN-RELATED PHENOMENA IN MAGNETIC AND SPIN-ORBIT COUPLED BOSE-EINSTEIN CONDENSATES

SHUHRAT N. MARDONOV

Departamento de Física Teórica e Historia de la Ciencia
Facultad de Ciencia y Tecnología
Universidad del País Vasco/Euskal Herriko Unibersitatea
(UPV/EHU)
LEIOA
Junio 2015

MEMORIA PRESENTADA PARA OPTAR AL GRADO DE
DOCTORA POR LA
UNIVERSIDAD DEL PAÍS VASCO/EUSKAL HERRIKO UNIBERTSITATEA

When asked "Dr. Einstein, why is it that when the mind of man has stretched so far as to discover the structure of the atom we have been unable to devise the political means to keep the atom from destroying us?" That is simple, my friend. It is because politics is more difficult than physics.

Albert Einstein

To my family - "Oilam uchun".

Acknowledgements

No matter how much time has passed, no matter what happens in the present, there are some things we can never assign to oblivion, memories we can never rub away. Appreciation is the highest form of prayer, for it acknowledges the presence of good wherever you shine the light of your thankful thoughts.

Though only my name appears on the cover of this Thesis, many people have contributed to it. I owe my gratitude to all those who have made these studies possible and because of whom my graduate experience has been one that I will cherish forever.

These years of most valuable, estimable, unforgettable, and exclusive period in my life at the esteemed University of Basque Country (UPV/EHU) will never rub away from my memory. I have greatly enjoyed my time with many respected people, particularly with my reputable colleagues and with my friends who offered me an unlimited and immeasurable support during this period. It is difficult for me to think about ending of my period in Bilbao and the time to fly back home.

There is a number of people without whom this Thesis might not have been completed, and to whom I am greatly indebted.

First and foremost I would like to express my deepest and unlimited appreciation to my supervisor, Prof. Evgeny Sherman. He supported and encouraged me even before my arrival and days I began working on my PhD Thesis at the UPV/EHU. I liked, when he said something like "It is a good result or it is impossible!" to encourage me to work hard. Ever since, Prof. Sherman has supported me not only guiding my research over the last three years, but also academically and emotionally through the bumpy road to finish this Thesis. And many thanks and gratefulness to my first supervisor Prof. Abdullah Rakhimov from Uzbekistan who has been the basic person on my academic way. I am grateful to the staff at the Samarkand Agricultural University of Uzbekistan for their support during my graduate study.

My sincere appreciation goes to Prof. Gonzalo Muga (UPV/EHU) for great discussions and support to all my works during this period, which was really important for me and my Thesis. Also, I am grateful to his students Sofia Martínez-Garaot, Sara Ibañez, and Mikel Palmero for their valuable comments, collaboration, and contribution to my work.

I am truly grateful to Prof. Michele Modugno (UPV/EHU) for his most valuable contribution, particularly for the enormous time he devoted to our collabo-

ration. My sincere acknowledgment goes to Prof. Andreas Schilling (University of Zurich) for collaboration and great experimental ideas for our work. Special thanks to Prof. Xi Chen and Dr. Yue Ban (Shanghai University) for their great collaboration and moral support.

I am proud that I have studied in the Basque Country, where the most basic source of my life energy resides: my sincere friends. I have amazing friends, unique in many ways, in Europe and outside. Their support has been unconditional all these years; they have given many things for me to be at the UPV/EHU, they have shared with me every great moment and supported me whenever I needed it.

I am also thankful to eASTANA Committee, who provide me with financial support for study in Bilbao, particularly to esteemed and most respected Prof. Alberto Oleaga.

Most importantly, none of this would have ever been possible without the love and patience of my family. My family whom this Thesis is dedicated to, has been a permanent source of love, support, and strength all these years. I would like to express my heart-felt gratitude to my mother, father, and mother in law. My extended family has aided and encouraged me throughout this endeavor.

I dedicate this Thesis
to my family,
my parents, and my wife.
I love you all dearly.

This Thesis has been financed by EU-funded Erasmus Mundus Action 2 eASTANA, "euroAsian Starter for Technical Academic Network Application" (Agreement No. 2001-2571/001-001-EMA2). Supported by the University of the Basque Country UPV/EHU, the Samarkand Agriculture Institute, and the Samarkand State University.

Contents

Publications

Journal Articles

- V. I. Yukalov, A. Rakhimov, and S. Mardonov
  Quasi-equilibrium mixture of itinerant and localized Bose atoms in optical lattice
  Laser Physics **21**, 264 (2011)

- A. Rakhimov, Sh. Mardonov, and E. Ya. Sherman
  Macroscopic properties of triplon Bose-Einstein condensates
  Annals of Physics **326**, 249 (2011)

- A. Rakhimov, Sh. Mardonov, E. Ya. Sherman, and A. Schilling
  The effects of disorder in dimerized quantum magnets in mean field approximations
  New Journal of Physics **14**, 113010 (2012)

- Sh. Mardonov, M. Palmero, M. Modugno, E. Ya. Sherman, and J. G. Muga
  Interference of spin-orbit coupled Bose-Einstein condensates
  Europhysics Letters **106**, 60004 (2014)

- Sh. Mardonov, E. Ya. Sherman, J. G. Muga, H.-W. Wang, Y. Ban, and Xi Chen
  Collapse of spin-orbit-coupled Bose-Einstein condensates
  Physics Review A **91**, 043604 (2015)

- Sh. Mardonov, M. Modugno, and E. Ya. Sherman
  Dynamics of a macroscopic spin qubit in spin-orbit coupled Bose-Einstein condensates
  Journal of Physics B: Atomic, Molecular and Optical Physics **48**, 115302 (2015).

- Sh. Mardonov, M. Modugno, and E. Ya. Sherman
  Spin dynamics of spin-orbit coupled Bose-Einstein condensate in a random potential
  Physical Review Letters, (2015) submitted.

Introduction

Bose-Einstein condensation (BEC) is one of the first phenomena predicted in macroscopic quantum physics. The striking feature of this effect is condensation in the momentum rather than in the coordinate space. At the transition temperature particles gradually begin to condense in the zero-momentum state. In the absence of interatomic interactions at $T = 0$ all particles have zero momentum. The first excellent application of the BEC theory taking into account weak interatomic interaction was liquid He, which demonstrated Bogoliubov sound-like excitations and superfluidity. In the 1960th the idea of Bose-Einstein condensation was applied to optically produced excitons in solids. The attempts to find new types of atomic condensates continued since it would be of a great interest to see condensates of other types of atoms, possible only at extremely low temperatures, where the quantum effects dominate the physics of the system. This was achieved by laser cooling technique, and Bose-Einstein condensates of alkali atoms were reported in 1995 by three research groups: E. Cornell and C. Wieman (from JILA), W. Ketterle (from MIT) and R. Hulet (from Rice University). These seminal results gave researches access to macroscopic quantum systems with adjustable properties, including control of the interatomic interaction. Thus, a rapidly developing field of a great interest for experimental and theoretical physics has been opened. New quantum phenomena seen on macroscopic scale such as the ability to control particles distribution in the momentum space, macroscopic interference, fascinating nonlinear properties, and many others, strongly modified the way of thinking of new generation of physicists.

The general phenomenon of Bose-Einstein condensation is very broad and constantly brings new results for new systems. A recent achievement is the discovery of the Bose-Einstein condensation of quasiparticles such as strongly nonequilibrium magnons (or equilibrium "triplons") in quantum and classical magnets and condensation of optical polaritons in quantum microcavities. Optically produced atomic condensates can be put in optical lattices, thus, exploring new fields related to solid-state physics phenomena. Very recently, it was found that although the atoms are bosons, they can be characterized by optically produced pseudospin 1/2. This pseudospin can be coupled to the momentum, leading to realization of spin-orbit coupled cold atomic gases and BECs. These novel types of BECs are studied in this Thesis.

The Thesis consists of four parts discussing different topics. The first part

(Chapters 1 and 2) deals with Bose-Einstein condensation of triplons in quantum magnets. In the first Chapter we address the macroscopic properties of the triplon BEC. We study in the Hartree-Fock-Bogoliubov approximation the speed of sound, specific heat, and magnetic susceptibility of the condensates. Here we show both the qualitative and quantitative importance of the anomalous averages, which allowed us to explain the available experimental results and predict new ones such as high-field instability. In the second Chapter we develop a theory of the disorder effects on the Bose-Einstein condensation of triplons taking extensively investigated $Tl_{1-x}K_xCuCl_3$ solid solution as a prototype for studies of specific properties. We consider different disorder-induced phases and demonstrate that, in addition to the effects of disorder, a renormalization of the system material parameters should be done to get agreement with the experiments. Second part (Chapter 3) deals with the cold bosons in optical lattices. In the third Chapter we analyze coexistence of delocalized and localized atoms in an optical lattice with an integer filling factor at zero temperature. We show that this coexistence is possible only in a quasiequilibrium regime and find conditions for realization of such a coexistence. In the third part (Chapter 4) two-dimensional BEC is considered. In the fourth Chapter 6 we address the systems of attracting atoms in the Feshbach resonance regime and study the dynamics and possible collapse of a quasi two-dimensional spin-orbit coupled BEC. We consider two different realizations of SOC such as the Rashba-like and the balanced Rashba-Dresselhaus and show how the collapse process depends on the type of the coupling. The presentation in the fourth part (Chapters 5-7) is related to one-dimensional realizations of BECs. In the fifth Chapter we concentrate on the role of the synthetic magnetic field in the macroscopic interference of one-dimensional spin-orbit coupled BECs. We explore different regimes of the interference and find that synthetic Zeeman-like magnetic field can strongly change the interference pattern. In the Chapter 6 we consider driven dynamics of a BEC-based macroscopic spin qubit and show that the anomalous velocity, arising due to the spin-orbit coupling (SOC), leads to nontrivial consequences in the ability of coherent spin manipulation. In addition, interatomic interactions play an important role in the spin dynamics. In Chapter 7 we consider the spin evolution of condensate in a random potential and study disorder-induced spin relaxation. We demonstrate that the BEC in a disordered potential can have spin relaxation mechanisms, which cannot be seen in solids, although these effects have been a topic of a strong interest for decades there. Extended conclusions will be presented at the end.

Part I

BOSE-EINSTEIN CONDENSATION IN QUANTUM MAGNETS

Chapter 1

Macroscopic properties of triplons in quantum magnets

Magnetic insulators can be characterized by a gap separating the singlet ground state from the lowest energy triplet, $S = 1$ excitation. If the gap can be closed by the Zeeman interaction in applied magnetic field the resulting $S_z = -1$ quasiparticles, triplons, can have concentrations sufficient to undergo the Bose-Einstein condensation transition. We consider macroscopic properties of the triplon Bose-Einstein condensates in the Hartree-Fock-Bogoliubov approximation taking into account the anomalous averages. We prove that these averages play qualitative role in the condensate properties. As a result, we show that with the increase in the external magnetic field at a given temperature, the condensate demonstrates an instability related to the appearance of nonzero phonon damping and a change in the characteristic dependence of the speed of sound on the magnetic field. The calculated magnetic susceptibility diverges when the external magnetic field approaches this instability threshold, providing a tool for the experimental verification of this approach.

1.1 Introduction

Macroscopic systems governed by quantum mechanics of interacting particles, with ensembles of cold atoms and quantum magnets being intensively investigated examples, attract a great deal of interest.

Triplet quasiparticles in magnetic insulators, being bosons with spin equal to one, can undergo the Bose-Einstein condensation transition [1–5]. An example of this kind of condensate is the systems far away from the equilibrium, where high concentration of spin excitations (magnons) is achieved by a strong resonant external magnetic field pumping [6]. At a sufficiently intense pumping, this type of condensation can occur at temperatures of the order of 100 K. Second example [7] is the magnons in superfluid He^3, where the magnetism appears due to the very small nuclear rather than electron magnetic moment. This condensation occurs at temperatures lower than 10^{-3} K. Third interesting example is presented by triplons, appearing if the gap in the triplet excitations spectrum separating it from the singlet ground state, can be closed by the Zeeman effect of the magnetic field [8, 9]. The field splits the spin $S = 1$ excitations into three branches with $S_z = 0, \pm 1$. When the Zeeman shift of the $S_z = -1$ branch exceeds the initial gap in the spectrum, a finite population of triplons, which can be considered as the reconstruction of the ground state, is formed even at zero temperature, as shown in Fig. 1.1. The Bose-Einstein condensation transition is seen as the transverse magnetization, which occurs if the field becomes higher than the critical one [10]. The Bose-Einstein condensation of triplons was experimentally first observed [11, 12] and thoroughly studied in the magnetic insulator $TlCuCl_3$ [12] where magnetic properties are due to the presence of noncompensated single-electron spins of Cu ions. Similar findings in a variety of other compounds followed shortly [13–17]. Recently, Bose-Einstein condensation of magnetic excitations was studied theoretically in compounds, where the magnetism is due to the spins of vanadium [18] or chromium [19] ions. These three dimensional systems with various degrees of anisotropy and easily tunable provide the researchers with new abilities to study the Bose-Einstein condensation, including the effects of disorder. The tunability is realized by easily changing the chemical potential with the external magnetic field $H_{\rm ext}$. The condensates were studied in a variety of magnetic fields up to the fields where the Zeeman effect strongly changes the properties of the systems due to the magnetization saturation.

Since the triplon Bose-Einstein condensation occurs in solids, it possesses at least three interesting features resulting from its coupling to the host lattice. First, it is directly influenced by the spin-orbit coupling inherent to the solid where it is located [20]. Second, the triplon Bose-Einstein condensation is coupled to phonons, and, therefore, can provide a test for the effects of decoherence and hysteresis due to the coupling to the lattice [22, 23]. Third, an external pressure applied to the crystal can strongly change the properties of the triplon Bose-Einstein condensation [24, 25]. In addition, the solid-state background for the triplon Bose-Einstein condensation makes it accessible by a variety of experimental techniques, not applicable for the atomic condensates.

Theoretical description of triplon Bose-Einstein condensation in relatively weak

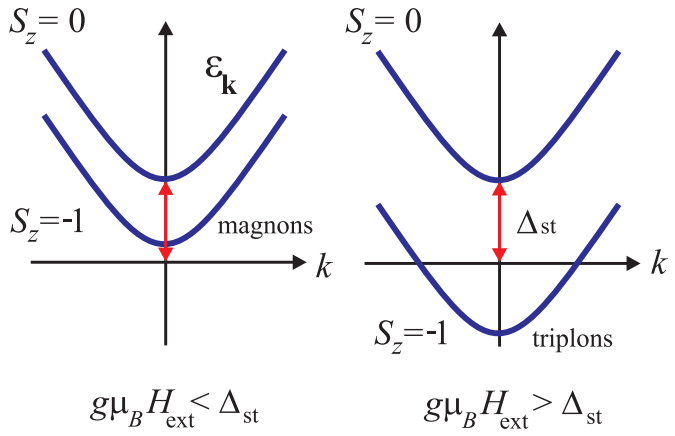

Figure 1.1: Evolution of the magnon states with the increase in the magnetic field. When the bottom of $S_z = -1$ band has negative energy, magnons (left panel) become "triplons" (right panel).

fields, where the Zeeman splitting is much less than the width of the triplon band in the Brillouin zone, and, correspondingly, concentration of triplons is small, can be done in terms of weakly interacting Bose gas theory. The observation of the sound-like Bogoliubov spin-flip mode, the fingerprint of the Bose-Einstein condensation in an interacting Bose gas, in the neutron scattering experiment [26] provided the strong support of this approach to the Bose-Einstein condensation of triplons.

Main tools for these studies are based on the approach usually referred to as the Hartree-Fock-Popov (HFP) approximation, neglecting the anomalous density terms. The drawback of this approximation is the prediction of a jump in the triplon density, and, in turn, in the sample magnetization across the transition temperature. Although this approach provides a good quantitative description of the specific heat, it is unclear whether it captures qualitatively all relevant physics of the condensate. For this reason it is interesting to study the behavior of the triplon Bose-Einstein condensation using a more accurate approach in order to see whether the analysis beyond the HFP approximation reveals new qualitative features.

It was in Ref. [27] shown that an extended version of the mean field approach (MFA) taking into account anomalous density terms in the condensate, improves the situation considerably [28]. The key part of this approach concentrates on finding the speed of sound-like Bogoliubov excitations in the Bose-Einstein condensation of interacting particles. This Hartree-Fock-Bogoliubov (HFB) approximation [29] leads to a continuous magnetization across the transition, in agreement with the experiment. By applying this approximation to the Bose-Einstein condensation of triplons we have shown that when the external magnetic field $H_{\rm ext}$ exceeds a critical value, $H_{\rm ext}^{\rm cr}$, the speed of sound becomes complex and the Bose-Einstein condensate undergoes an instability.

Another general feature clearly seen in the triplon Bose-Einstein condensation

is the dependence of its physics on the bare magnon dispersion $\varepsilon_{\mathbf{k}}$. The non-parabolic bare dispersion of magnons [23, 30–32] leads to a non-trivial dependence of the transition temperature T_c on the concentration $\rho \sim M(T, H_{\rm ext})$ and, hence, on $H_{\rm ext}$. The bare dispersion, being itself $H_{\rm ext}$-independent, determines the interplay of kinetic and potential energy of a macroscopic system, and, therefore, plays a crucial role in the Bose-Einstein condensation properties. The effects of the bare dispersion are clearly seen experimentally in $TlCuCl_3$ as the ρ-dependence $T_c \sim \rho^{\phi(\rho)}$. The exponent $\phi(\rho)$ approaches 2/3 at low concentrations (low $T_{\rm cr}$), [33] as expected for the parabolic $\varepsilon_k \sim k^2$, while at $T > 2.5$ K, $\phi(\rho)$ is close to 0.5. We will address the role of the dispersion below in the chapter and present simplified for the parabolic dispersion calculations.

In this Chapter we address the macroscopic properties of the Bose-Einstein condensation in terms of the speed of sound, specific heat, and magnetic susceptibility, in the HFB approximation and show both qualitative and quantitative importance of the anomalous averages. First, we outline main features of the HFB approximation, then we discuss the specific heat and magnetic susceptibility in this approximation and show the importance of the anomalous averages. Finally, we provide a detailed analysis of the instability caused by external magnetic field in terms of the speed of sound and magnetization. This instability is the qualitative effect, not expected if the anomalous averages are not taken into account.

1.2 The Hartree-Fock-Bogoliubov approximation

We begin with the Hamiltonian of triplons as a nonideal Bose gas with repulsive interaction:

$$\hat{H} = \int d^3r \left[\hat{\psi}^\dagger(\mathbf{r}) \left(\hat{K} - \mu \right) \hat{\psi}(\mathbf{r}) + \frac{U}{2} \left(\hat{\psi}^\dagger(\mathbf{r}) \hat{\psi}(\mathbf{r}) \right)^2 \right], \tag{1.1}$$

where $\hat{\psi}(\mathbf{r})$ is the bosonic field operator, U is the interaction strength, and $\hat{K}$ is the kinetic energy operator which defines the bare triplon dispersion $\varepsilon_{\mathbf{k}}$ in momentum space. Since the triplon Bose-Einstein condensation occurs in solids, we perform integration over the unit cell of the crystal with the corresponding momenta defined in the first Brillouin zone. Below the spectrum will be assumed isotropic: $\varepsilon_{\mathbf{k}} = \varepsilon(k)$. The parameter μ characterizes an additional direct contribution to the triplon energy due to the external field and being rewritten as

$$\mu = g\mu_B H_{\rm ext} - \Delta_{\rm st} \tag{1.2}$$

can be interpreted as a chemical potential of the $S_z = -1$ triplons [10]. In Eq. (1.2) g is the electron Landé factor, μ_B is the Bohr magneton and $\Delta_{\rm st}$ is the spin gap separating the singlet ground state from the lowest-energy triplet excitation (Fig. 1.1).

In general the Hamiltonian in (1.1) is invariant under global $U(1)$ gauge transformation

$$\hat{\psi}(\mathbf{r}) \to e^{i\alpha} \hat{\psi}(\mathbf{r}) \tag{1.3}$$

with α being a real number. However, this symmetry is broken in the condensed phase, where $T \leq T_{\rm cr}$, and restored for the normal phase, $T > T_{\rm cr}$. Note that in the experimental studies of Bose-Einstein condensation of atomic gases the density ρ (or equivalently, the total number of atoms) is fixed initially and the chemical potential μ should be calculated self-consistently, while in the case of triplon Bose-Einstein condensation the chemical potential is fixed by the magnetic field and the density is determined self-consistently by μ.

In this Chapter we adopt the units $k_B \equiv 1$ for the Boltzmann constant, $\hbar \equiv 1$ for the Planck constant, and $V \equiv 1$ for the unit cell volume. In these units the energies are measured in Kelvin, the mass m is expressed in K^{-1}, and the magnetic susceptibility χ for the magnetic fields measured in Tesla has the units of $\mathrm{K/T}^2$, the momentum and specific heat C_v are dimensionless. Particularly, the Bohr magneton is $\mu_B = \hbar e/2m_0c \approx 0.67$ K/T, where m_0 is the free electron mass, and e is the fundamental charge.

1.2.1 Condensate phase $T \leq T_{\rm cr}$

The spontaneous gauge symmetry breaking is the necessary and sufficient condition for Bose-Einstein condensation [29] and can be realized by the Bogoliubov shift in the field operator as

$$\hat{\psi}(\mathbf{r}) = \psi_0(\mathbf{r}) + \delta\hat{\psi}(\mathbf{r}), \tag{1.4}$$

where for the uniform case the function $\psi_0(\mathbf{r})$ is a constant defining the density of condensed particles as

$$\rho_0 = |\psi_0|^2. \tag{1.5}$$

Since by definition the average of $\hat{\psi}^\dagger(\mathbf{r})\hat{\psi}(\mathbf{r})$ is the total number of particles:

$$N = \int_V d^3r \langle \hat{\psi}^\dagger(\mathbf{r})\hat{\psi}(\mathbf{r})\rangle. \tag{1.6}$$

with the density of triplons per unit cell $\rho = N/V$, from normalization condition

$$\rho = \rho_0 + \rho_1 \tag{1.7}$$

one immediately obtains

$$\rho_1 = \frac{1}{V}\int_V d^3r \langle \delta\hat{\psi}^\dagger(\mathbf{r})\delta\hat{\psi}(\mathbf{r})\rangle. \tag{1.8}$$

Therefore the field operator $\delta\hat{\psi}(\mathbf{r})$ determines the density of uncondensed particles. Note that $\delta\hat{\psi}(\mathbf{r})$ and the condensate function should be considered as independent orthogonal variables:

$$\int d^3r \delta\hat{\psi}(\mathbf{r})\psi_0(\mathbf{r}) = 0. \tag{1.9}$$

Consequently, transforming to the momentum space

$$\delta\hat{\psi}(\mathbf{r}) = \sum_{\mathbf{k}} \hat{a}_{\mathbf{k}} e^{i\mathbf{kr}} \equiv \int \frac{d^3k}{(2\pi)^3}\hat{a}_{\mathbf{k}} e^{i\mathbf{kr}} \tag{1.10}$$

and inserting (1.10) into (1.8) one can see that in (1.10) the summation by momentum in the finite volume should not include $\mathbf{k} = \mathbf{0}$ states. Below we indicate this rule by introducing prime sign in the momentum summation.

Now using (1.4) and (1.10) in (1.1) we present the Hamiltonian as the sum of five terms

$$\hat{H} = \sum_{n=0}^{4} \hat{H}_n, \tag{1.11}$$

labeled according to their order with respect to $\hat{a}_{\mathbf{k}}$ and $\hat{a}^{\dagger}_{\mathbf{k}}$. The zero-order term does not contain the field operators of uncondensed triplons

$$\langle \hat{H}_0 \rangle = \frac{U}{2}\rho_0^2 - \mu\rho_0. \tag{1.12}$$

The first order term is identically zero

$$\hat{H}_1 = 0, \tag{1.13}$$

due to the orthogonality condition (1.8). The second-order term is

$$\hat{H}_2 = {\sum_{\mathbf{k}}}' \left[(\varepsilon_k - \mu + 2U\rho_0)\, \hat{a}^{\dagger}_{\mathbf{k}}\hat{a}_{\mathbf{k}} + \frac{U\rho_0}{2}\left(\hat{a}_{\mathbf{k}}\hat{a}_{-\mathbf{k}} + \hat{a}^{\dagger}_{\mathbf{k}}\hat{a}^{\dagger}_{-\mathbf{k}} \right) \right]. \tag{1.14}$$

The third-order

$$\hat{H}_3 = U\sqrt{\rho_0} \sum_{\mathbf{k},\mathbf{p}} \left(\hat{a}^{\dagger}_{\mathbf{p}}\hat{a}_{\mathbf{p}-\mathbf{k}}\hat{a}_{\mathbf{k}} + \hat{a}^{\dagger}_{\mathbf{k}}\hat{a}^{\dagger}_{\mathbf{p}-\mathbf{k}}\hat{a}_{\mathbf{p}} \right) \tag{1.15}$$

as well as fourth-order

$$\hat{H}_4 = \frac{U}{2} {\sum_{\mathbf{k},\mathbf{p},\mathbf{q}}}' \hat{a}^{\dagger}_{\mathbf{k}}\hat{a}^{\dagger}_{\mathbf{p}}\hat{a}_{\mathbf{q}}\hat{a}_{\mathbf{k}+\mathbf{p}-\mathbf{q}} \tag{1.16}$$

terms are rather complicated and a diagonalization procedure is required. For this purpose in HFB approximation the following procedure is conventionally implemented [34]:

$$\begin{aligned} &\hat{a}^{\dagger}_{\mathbf{k}}\hat{a}_{\mathbf{p}}\hat{a}_{\mathbf{q}} \to 2\langle \hat{a}^{\dagger}_{\mathbf{k}}\hat{a}_{\mathbf{p}} \rangle \hat{a}_{\mathbf{q}} + \hat{a}^{\dagger}_{\mathbf{k}} \langle \hat{a}_{\mathbf{p}}\hat{a}_{\mathbf{p}} \rangle, \\ &\hat{a}^{\dagger}_{\mathbf{k}}\hat{a}^{\dagger}_{\mathbf{p}}\hat{a}_{\mathbf{q}}\hat{a}_{\mathbf{m}} \to 4\hat{a}^{\dagger}_{\mathbf{k}}\hat{a}_{\mathbf{m}} \langle \hat{a}^{\dagger}_{\mathbf{p}}\hat{a}_{\mathbf{q}} \rangle + \hat{a}_{\mathbf{q}}\hat{a}_{\mathbf{m}} \langle \hat{a}^{\dagger}_{\mathbf{k}}\hat{a}^{\dagger}_{\mathbf{p}} \rangle + \hat{a}^{\dagger}_{\mathbf{k}}\hat{a}^{\dagger}_{\mathbf{p}} \langle \hat{a}_{\mathbf{q}}\hat{a}_{\mathbf{m}} \rangle - 2\rho_1^2 - \sigma^2, \end{aligned} \tag{1.17}$$

where $\langle \hat{a}^{\dagger}_{\mathbf{k}}\hat{a}_{\mathbf{p}} \rangle = \delta_{\mathbf{k},\mathbf{p}} n_{\mathbf{k}}$, $\quad \langle \hat{a}_{\mathbf{k}}\hat{a}_{\mathbf{p}} \rangle = \delta_{\mathbf{k},-\mathbf{p}} \sigma_{\mathbf{k}}$ with $n_{\mathbf{k}}$ and $\sigma_{\mathbf{k}}$ being related to the normal (ρ_1) and anomalous (σ) densities as

$$\rho_1 = \sum_{\mathbf{k}} n_{\mathbf{k}}, \qquad \sigma = \sum_{\mathbf{k}} \sigma_{\mathbf{k}}. \tag{1.18}$$

Here we underline that the main difference between the HFP and HFB approximations concerns the anomalous density: neglecting σ as well as $\langle \hat{a}_{\mathbf{k}}\hat{a}_{\mathbf{p}} \rangle$ in (1.14)

and (1.17) one arrives at the HFP approximation, which can also be obtained in variational perturbation theory [35]. However, the normal, ρ_1, and anomalous averages, σ, are equally important and neither of them can be neglected in a theory self-consistent [36, 37]. Although ρ_1 and σ are functions of temperature and external magnetic field, we omit at explicit dependences in the formulas when it does not cause a confusion.

Taking into account that $E_3 = \langle \hat{H}_3 \rangle = 0$, the expectation value of the energy can be evaluated as $E(T \leq T_{\rm cr}) = E_0 + E_2$, where

$$E_0 = \frac{U\rho_0^2}{2} - \mu\rho_0 - \frac{U}{2}(2\rho_1^2 + \sigma^2), \tag{1.19}$$

and $E_2 = \langle \hat{H}_2^{'} \rangle$, with $\hat{H}_2^{'}$ being quadratic in $\hat{a}_{\mathbf{k}}, \hat{a}_{\mathbf{k}}^{\dagger}$:

$$\hat{H}_2^{'} = \sum_{\mathbf{k}} \left[\omega_k \hat{a}_{\mathbf{k}}^{\dagger} \hat{a}_{\mathbf{k}} + \frac{\Delta}{2} \left(\hat{a}_{\mathbf{k}} \hat{a}_{-\mathbf{k}} + \hat{a}_{\mathbf{k}}^{\dagger} \hat{a}_{-\mathbf{k}}^{\dagger} \right) \right]. \tag{1.20}$$

In the last Equation we have

$$\omega_k = \varepsilon_k - \mu_{\rm eff}, \quad \mu_{\rm eff} = \mu - 2U\rho, \tag{1.21}$$

$$\Delta = U(\rho_0 + \sigma). \tag{1.22}$$

The next step in both approximations is the Bogoliubov transformation

$$\hat{a}_{\mathbf{k}} = u_{\mathbf{k}} \hat{b}_{\mathbf{k}} + v_{\mathbf{k}} \hat{b}_{-\mathbf{k}}^{\dagger}, \quad \hat{a}_{\mathbf{k}}^{\dagger} = u_{\mathbf{k}} \hat{b}_{\mathbf{k}}^{\dagger} + v_{\mathbf{k}} \hat{b}_{-\mathbf{k}} \tag{1.23}$$

to diagonalize $\hat{H}_2^{'}$. The operators $\hat{b}_{\mathbf{k}}$ and $\hat{b}_{\mathbf{k}}^{\dagger}$ can be interpreted as annihilation and creation operators of phonons with following properties:

$$[\hat{b}_{\mathbf{k}}, \hat{b}_{\mathbf{p}}^{\dagger}] = \delta_{\mathbf{k},\mathbf{p}}, \quad \langle \hat{b}_{\mathbf{k}}^{\dagger} \hat{b}_{-\mathbf{k}}^{\dagger} \rangle = \langle \hat{b}_{\mathbf{k}} b_{-\mathbf{k}} \rangle = 0, \tag{1.24}$$

$$\langle \hat{b}_{\mathbf{k}}^{\dagger} \hat{b}_{\mathbf{k}} \rangle = f_B(\mathcal{E}_k) = \frac{1}{e^{\beta \mathcal{E}_k} - 1}, \tag{1.25}$$

where $\beta \equiv 1/T$. To determine the BEC phonon dispersion $\mathcal{E}_k$ we insert (1.23) into (1.20) and require that the coefficient of the term $\hat{b}_{\mathbf{k}} b_{-\mathbf{k}} + b_{-\mathbf{k}}^{\dagger} \hat{b}_{\mathbf{k}}^{\dagger}$ vanishes, i.e:

$$\omega_k u_{\mathbf{k}} v_{\mathbf{k}} + \frac{\Delta}{2} \left(u_{\mathbf{k}}^2 + v_{\mathbf{k}}^2 \right) = 0. \tag{1.26}$$

Now using the condition $u_{\mathbf{k}}^2 - v_{\mathbf{k}}^2 = 1$ and presenting $u_{\mathbf{k}}, v_{\mathbf{k}}$ as

$$u_{\mathbf{k}}^2 = \frac{\omega_k + \mathcal{E}_k}{2\mathcal{E}_k}, \qquad v_{\mathbf{k}}^2 = \frac{\omega_k - \mathcal{E}_k}{2\mathcal{E}_k} \tag{1.27}$$

yields

$$\sqrt{\omega_k^2 - \mathcal{E}_k^2} = -\Delta \tag{1.28}$$

that is

$$\mathcal{E}_k = \sqrt{(\omega_k + \Delta)(\omega_k - \Delta)} \tag{1.29}$$

where ω_k and Δ are given in Eqs. (1.21) and (1.22).

Further requirement for $\mathcal{E}_k$ follows from the Hugenholtz-Pines theorem [38]: at small momentum k the spectrum should be gapless, and, therefore, the phonon dispersion is linear: $\mathcal{E}_k \sim ck + O(k^2)$, where c can be considered as the sound speed.[1] This linearity can be achieved by setting

$$\omega_k - \Delta = \varepsilon_k, \tag{1.30}$$

which together with Eq.(1.22) yields

$$\mu_{\text{eff}} = \mu - 2U\rho = -\Delta. \tag{1.31}$$

With this choice one obtains

$$\mathcal{E}_k = \sqrt{\varepsilon_k}\sqrt{\varepsilon_k + 2\Delta}, \tag{1.32}$$

with the sound speed

$$c = \sqrt{\frac{\Delta}{m}}, \tag{1.33}$$

i.e. $\Delta = mc^2$. Here m has the meaning of the triplon effective mass, characterizing the dispersion in the limit of small momenta $\varepsilon_k \approx k^2/2m$.

1.2.2 Condensed fraction and the condensate energy

Having fixed $u_{\mathbf{k}}$ and $v_{\mathbf{k}}$ one can find normal and anomalous densities as well as the energy by using equations (1.18)-(1.27). For example, inserting (1.23) into (1.18) results in

$$\sigma = \sum_{\mathbf{k}} \langle \hat{a}_{\mathbf{k}} \hat{a}_{-\mathbf{k}} \rangle = \sum_{\mathbf{k}} u_{\mathbf{k}} v_{\mathbf{k}} (1 + 2f_B(\mathcal{E}_k)) = -\Delta \sum_{\mathbf{k}} \frac{W_k}{\mathcal{E}_k}, \tag{1.34}$$

where we used the relation $u_{\mathbf{k}} v_{\mathbf{k}} = -\Delta/2\mathcal{E}_k$ and introduced notation $W_k = 1/2 + f_B(\mathcal{E}_k)$. Similarly one obtains:

$$\rho_1 = \sum_{\mathbf{k}} \langle \hat{a}^\dagger_{\mathbf{k}} \hat{a}_{\mathbf{k}} \rangle = \sum_{\mathbf{k}} \left(\frac{W_k \omega_k}{\mathcal{E}_k} - \frac{1}{2} \right), \tag{1.35}$$

$$E_2 = \langle \hat{H}_2' \rangle = \sum_{\mathbf{k}} \mathcal{E}_k f_B(\mathcal{E}_k) + \frac{1}{2} \sum_{\mathbf{k}} (\mathcal{E}_k - \omega_k), \tag{1.36}$$

with $\omega_k = \varepsilon_k + \Delta$.

[1] It can be shown that [36,39] Δ is related to the normal (Σ_{n}) and anomalous (Σ_{a}) self-energies as $\Sigma_{\text{n}} = \Delta + \mu$ and $\Sigma_{\text{a}} = \Delta$, respectively. The last two equations give $\Sigma_{\text{n}} - \Sigma_{\text{a}} = \mu$ which is again in agreement with Hugenholtz-Pines theorem [40, 41].

When the bare dispersion ε_k is isotropic, the momentum summation can be done with:

$$\sum_{\mathbf{k}} f\left(k^2\right) = \frac{4\pi}{(2\pi)^3} \int_0^\infty f\left(k^2\right) k^2 dk. \tag{1.37}$$

As a result, at $T = 0$ the quantities in Eqs.(1.34)-(1.36) can be represented as:

$$\rho_1(0) = \frac{1}{4\pi^2} \int_0^\infty k^2 dk \left(\frac{\varepsilon_k + \Delta}{\mathcal{E}_k} - 1 \right) \tag{1.38}$$

$$\sigma(0) = -\frac{\Delta}{4\pi^2} \int_0^\infty \frac{k^2 dk}{\mathcal{E}_k}, \tag{1.39}$$

$$E_2(0) = \frac{1}{4\pi^2} \left(\int_0^\infty \mathcal{E}_k k^2 dk - \int_0^\infty \left(\varepsilon_k + \Delta\right) k^2 dk \right), \tag{1.40}$$

The divergences in these integrals can be regularized by introducing a cutting parameter Λ ($\Lambda \to \infty$ at the end of the calculations) or equivalently by using the dimensional regularization scheme. Now, assuming for the moment that, for $T = 0$ case $\varepsilon_k = k^2/2m$ and using dimensional regularization one obtains:

$$\rho_1(0) = \frac{(\Delta m)^{3/2}}{3\pi^2}, \tag{1.41}$$

$$\sigma(0) = 3\rho_1(0), \tag{1.42}$$

$$E_2(0) = \frac{8(\Delta m)^{5/2}}{15 m \pi^2}. \tag{1.43}$$

Summarizing this subsection we rewrite the above formulas as:

$$\rho_1 = \frac{(\Delta m)^{3/2}}{3\pi^2} + \int \frac{d^3k}{(2\pi)^3} f_B(\mathcal{E}_k) \frac{\varepsilon_k + \Delta}{\mathcal{E}_k}, \tag{1.44}$$

$$\sigma = \frac{(\Delta m)^{3/2}}{\pi^2} - \Delta \int \frac{d^3k}{(2\pi)^3} f_B(\mathcal{E}_k) \frac{1}{\mathcal{E}_k}, \tag{1.45}$$

$$\begin{aligned} E &= \frac{8(\Delta m)^{5/2}}{15 m \pi^2} + \frac{U\rho_0^2}{2} - \mu\rho_0 - \frac{U}{2}\left(2\rho_1^2 + \sigma^2\right) \\ &+ \int \frac{d^3k}{(2\pi)^3} \mathcal{E}_k f_B\left(\mathcal{E}_k\right), \end{aligned} \tag{1.46}$$

where Bose distribution of phonons $f_B\left(\mathcal{E}_k\right)$ is defined in Eq.(1.25).

To perform the MFA calculations one starts by solving Eqs. (1.22) and (1.31) with ρ_1 and σ given by Eqs. (1.44) and (1.45). As outlined above, in contrast to the Bose-Einstein condensation of atomic gases, in the triplon problem the chemical potential μ is the input parameter, whereas the densities are the output ones. Bearing this in mind, we rewrite the main Eqs. (1.22) and (1.31) as

$$\Delta = \mu + 2U\left(\sigma - \rho_1\right), \tag{1.47}$$

$$\rho_0 = \Delta/U - \sigma. \tag{1.48}$$

The system of coupled equations, (1.44), (1.45) and (1.47), (1.48) has to be solved for given T and μ to evaluate the triplon density

$$\rho(T \leq T_{\rm cr}) = \rho_0 + \rho_1 = \frac{\Delta + \mu}{2U}, \tag{1.49}$$

which is proportional to the measured sample magnetization density M. Note that by formally setting $\sigma \equiv 0$ in all above formulas, one arrives at the HFP approximation and particularly

$$\Delta = \mu - 2U\rho_1, \qquad \rho_0 = \Delta/U. \tag{1.50}$$

1.2.3 Critical temperature and triplon density

Before discussing the normal $T > T_{\rm cr}$ phase we present the temperature of Bose-Einstein condensation transition. It is well-known that in the MFA the system of interacting Bose particles at $T \to T_{\rm cr}$ behaves similarly to an ideal gas. In fact, assuming $\rho_0(T \to T_{\rm cr}) = 0$, $\rho_1(T \to T_{\rm cr}) = \rho_{\rm cr}$, $\sigma(T \to T_{\rm cr}) = 0$, $\Delta(T \to T_{\rm cr}) = 0$, and $\mathcal{E}_k = \varepsilon_k$ one concludes from Eqs.(1.44),(1.47) that

$$\rho_{\rm cr} = \int \frac{d^3k}{(2\pi)^3} \frac{1}{\exp(\beta_{\rm cr}\varepsilon_k) - 1} = \frac{\mu}{2U}. \tag{1.51}$$

With given $\mu = \mu_B g H_{\rm ext} - \Delta_{\rm st}$ and coupling constant U, the critical temperature $T_{\rm cr} \equiv 1/\beta_{\rm cr}$ can be found as a solution of Eq. (1.51). Note that for the parabolic dispersion $\varepsilon_k = k^2/2m$, the integral (1.51) can be evaluated analytically giving following well known relation [42]:

$$T_{\rm cr}^{\rm [par]} = \frac{2\pi}{m} \left(\frac{\mu}{2\zeta(3/2)U} \right)^{2/3}, \tag{1.52}$$

where $\zeta(x)$ is the Riemann function.

As it has been underlined in section 1.1, the bare dispersion of magnons, ε_k, plays the crucial role in determining $T_{\rm cr}$. Figure 1.2 presents the transition temperature as a function of magnetic field $H_{\rm ext}$ and corresponding triplon density ρ, that is the sample magnetization, for parabolic $\varepsilon_k = k^2/2m$ and "relativistic"

$$\varepsilon_k = \sqrt{\Delta_{\rm st}^2 + J^2k^2/4} - \Delta_{\rm st} \tag{1.53}$$

bare dispersion, typical for a system with a gapped spectrum [25, 43]. Here the effective exchange parameter $J = 2\sqrt{\Delta_{\rm st}/m}$ is chosen to match the parabolic and the relativistic ε_k at small k. The dashed line obtained directly from Eq.(1.52) displays $T_{\rm cr} \sim \rho^{2/3}$ behavior. The solid one is a result of numerical solution of Eq.(1.51) with the dispersion in Eq.(1.53) and shows a crossover from $T_{\rm cr} \sim \rho^{2/3}$ at lower to $T_{\rm cr} \sim \rho^{0.5}$ at higher temperatures in agreement with the experimental data.[2] The decrease in $\Delta_{\rm st}$ enhances the role of relativistic features in the spectrum

[2] We mention that for linear dispersion $\varepsilon_k \sim k$, the exponent would be equal to 1/3, and, therefore, in the experimental regime, the triplon gas is between the "nonrelativistic" and strongly "relativistic" realizations.

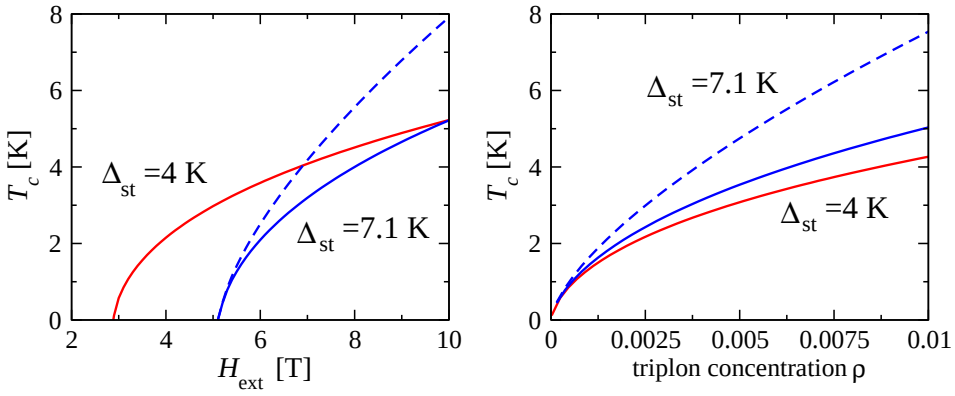

Figure 1.2: The critical temperature of Bose-Einstein condensation of triplons $T_{\rm cr}$ as a function of external field (left panel) and corresponding triplon density $\rho = \mu/2U$ (right panel) for two values of the singlet-triplet gap. To understand the role of the gap in the magnon spectrum, we present the results for $\Delta_{\rm st} = 4$ K, with the reduced exchange parameter yielding the same effective mass as for $\Delta_{\rm st} = 7.1$ K. The gap values are marked near the lines. The solid and dashed lines at $\Delta_{\rm st} = 7.1$ K are for the relativistic and parabolic dispersions.

and leads to a faster deviation from the $T_{\rm cr} \sim \rho^{2/3}$ behavior, as can be seen in Fig.1.2. Here and below we mainly use the set of input parameters as $m = 0.0204$ K^{-1}, $\Delta_{\rm st} = 7.1$ K, $U = 313$ K, and $g = 2.06$ [33] valid for the weakly anisotropic quantum antiferromagnet $TlCuCl_3$.

In the normal phase the symmetry in Eq.(1.3) is not broken and the Bogoliubov shift is not needed. Here the anomalous density vanishes, $\sigma(T > T_{\rm cr}) = 0$, and hence, both approximations, HFB and HFP coincide. As a result we obtain for the triplon density

$$\rho(T > T_{\rm cr}) = \int \frac{d^3k}{(2\pi)^3} \frac{1}{\exp(\beta\omega_k) - 1} \tag{1.54}$$

with $\omega_k = \varepsilon_k - \mu + 2U\rho \equiv \varepsilon_k - \mu_{\rm eff}$. Similarly, by setting $\Delta = \rho_0 = \sigma = 0$, $\rho_1 = \rho$, $\mathcal{E}_k = \omega_k$ in Eq.(1.46) one obtains following equation for the energy per unit cell

$$E(T > T_{\rm cr}) = -U\rho^2 + \int \frac{d^3k}{(2\pi)^3} \frac{\omega_k}{\exp(\beta\omega_k) - 1}. \tag{1.55}$$

The density of triplons as a function of temperature, evaluated in the HFP and HFB approximations is presented in Fig.1.3. It is seen that the former leads to a discontinuity in the magnetization near the critical temperature, while the latter gives a continuous behavior in accordance with the experimental data [33, 44, 45]. However, in the condensate phase, the triplon density is higher in the HFB than in the HFP approximation. Therefore, the validity of the description of

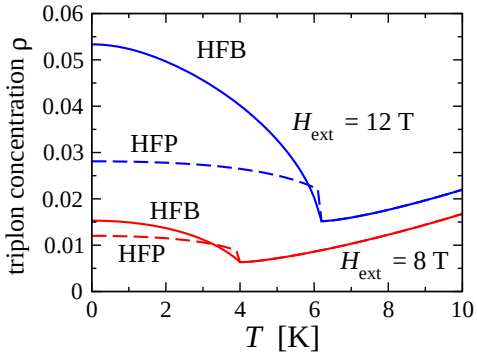

Figure 1.3: Comparison of the HFB (solid lines) and the HFP (dashed lines) results for the triplon density. The HFB approach shows a continuous behavior, which fully agrees with the experimental data [33, 44, 45] while the HFP approach leads to the discontinuity. The corresponding magnetic fields $H_{\rm ext}$ are marked near the plots.

the Bose-Einstein condensation in the HFP approximation can be checked in the magnetization measurement experiments.

1.3 Macroscopic properties: specific heat and magnetic susceptibility

1.3.1 General expressions with nonzero anomalous averages

Before discussing the susceptibility, we note that the macroscopic properties of the systems are related to their response to external fields. An example is given by the isothermal compressibility

$$\kappa_T = -\frac{1}{V}\left(\frac{\partial V}{\partial P}\right)_T = \frac{1}{\rho}\left(\frac{\partial \rho}{\partial P}\right)_T . \tag{1.56}$$

If $\kappa_T \to \infty$, the system becomes unstable [47,48] since an infinitesimal fluctuation of pressure P will lead to its collapse or explosion. The density of triplons is proportional to the magnetization M, while the $H_{\rm ext}$ simulates the pressure, and hence the relevant parameter, which determines the stability of the system with respect to the magnetic field, is the susceptibility

$$\chi(H_{\rm ext}, T) = \left(\frac{\partial M}{\partial H_{\rm ext}}\right)_T , \tag{1.57}$$

which can be expressed with the triplon density as:

$$\chi(H_{\rm ext}, T) = (g\mu_B)^2 \frac{\partial \rho}{\partial \mu}. \tag{1.58}$$

Triplon contribution to the constant volume specific heat C_v can be calculated by differentiation of the energy with respect to the temperature at given chemical potential, that is at given external field [46, 47]:

$$C_v(H_{\rm ext}, T) = \frac{\partial E}{\partial T}, \tag{1.59}$$

where the energies for condensate and normal states are given by Eqs. (1.46) and (1.55), respectively. We will omit $H_{\rm ext}$ from the arguments of $\chi(H_{\rm ext}, T)$ and $C_v(H_{\rm ext}, T)$ below.

We begin with the normal phase, where $\rho_0 = \sigma = \Delta = 0$. The derivative of the density with respect to the temperature can be evaluated here with Eq.(1.54) as

$$\frac{\partial \rho}{\partial T} = \frac{\beta S_1}{2S_2 - 1}. \tag{1.60}$$

Calculating the derivative of Eq.(1.55) with respect to T one obtains:

$$C_v(T > T_{\rm cr}) = -S_3 + 2US_1 \frac{\partial \rho}{\partial T}. \tag{1.61}$$

Here we introduced dimensionless quantities

$$S_1 = \sum_{\mathbf{k}} \omega_k f_B'(\omega_k), \quad S_2 = U \sum_{\mathbf{k}} f_B'(\omega_k), \quad S_3 = \beta \sum_{\mathbf{k}} \omega_k^2 f_B'(\omega_k), \tag{1.62}$$

and used the relation $\partial f_B(\omega)/\partial T = -\beta\omega f_B'(\omega)$, where

$$f_B'(\omega) = \frac{\partial f_B(\omega)}{\partial \omega} = -\beta \exp(\beta\omega) f_B^2(\omega)$$

and ω_k is given in Eq.(1.21).

Similarly, taking the derivative of the self-consistency Eq.(1.54), which we present here in the form:

$$\rho(\mu) = \sum_{\mathbf{k}} \frac{1}{\exp\left[\beta\left(\varepsilon_k - \mu + 2U\rho(\mu)\right)\right] - 1} \tag{1.63}$$

with respect to μ and solving the equation for $\partial\rho/\partial\mu$ one finds

$$\frac{\partial \rho}{\partial \mu} = \frac{S_2}{U}(2S_2 - 1).$$

As a result, we obtain with Eq.(1.58) the normal phase susceptibility:

$$\chi(T > T_{\rm cr}) = \frac{(g\mu_B)^2}{U} \frac{S_2}{2S_2 - 1}. \tag{1.64}$$

Now we proceed with the condensate phase, where the dependence of Δ and the corresponding normal and anomalous densities on temperature and magnetic field should be taken into account.

Here $C_v(T)$ is obtained by taking the derivative of $E\,(T < T_{\rm cr})$ given by Eq. (1.46). The latter can be rewritten as:

$$E\,(T < T_{\rm cr}) = E_2 - \frac{\mu^2}{2U} + U\left(\rho_1^2 - 2\rho_1\sigma\right), \tag{1.65}$$

where we used the relation $\rho_0 = \mu/U - 2\rho_1 + \sigma$ and present E_2 defined in Eq.(1.36) as:

$$E_2 = \frac{8m^{3/2}\Delta^{5/2}}{15\pi^2} + \sum_{\mathbf{k}} \mathcal{E}_k f_B\left(\mathcal{E}_k\right). \tag{1.66}$$

As a result:

$$C_v(T \le T_{\rm cr}) = \frac{\partial E_2}{\partial T} - 2U\rho_1\frac{\partial\sigma}{\partial T} - 2U\left(\rho - \frac{\mu}{U}\right)\frac{\partial\rho_1}{\partial T}. \tag{1.67}$$

We begin with calculation of $\partial\Delta/\partial T$, which is the key ingredient in the specific heat. It is obtained by differentiating both sides of the main equation (1.47) with respect to the temperature, and for known $\partial\Delta/\partial T$ the other two derivatives $\partial\rho_1/\partial T$ and $\partial\sigma/\partial T$ can be evaluated directly from Eqs.(1.44), (1.45). As a result one obtains the derivatives necessary to evaluate the specific heat:

$$\frac{\partial\Delta}{\partial T} = \frac{2U\beta}{1 - 2U\left(\dfrac{\sqrt{\Delta}m^{3/2}}{\pi^2} - \displaystyle\sum_{\mathbf{k}}\mathcal{F}\left(\mathcal{E}_k\right)\right)}\sum_{\mathbf{k}}\left(\varepsilon_k + 2\Delta\right)f_B'(\mathcal{E}_k), \tag{1.68}$$

$$\begin{aligned}\frac{\partial\rho_1}{\partial T} &= \frac{m\sqrt{\Delta m}}{2\pi^2}\frac{\partial\Delta}{\partial T}\\ &+ \sum_{\mathbf{k}}\left[\frac{\partial\Delta}{\partial T}\left(\frac{\varepsilon_k\Delta}{\mathcal{E}_k^2}\mathcal{F}\left(\mathcal{E}_k\right) + \frac{\varepsilon_k^2}{\mathcal{E}_k^2}f_B'\right) - \beta\left(\varepsilon_k + \Delta\right)f_B'(\mathcal{E}_k)\right],\end{aligned} \tag{1.69}$$

$$\begin{aligned}\frac{\partial\sigma}{\partial T} &= \frac{3m\sqrt{\Delta m}}{2\pi^2}\frac{\partial\Delta}{\partial T}\\ &- \sum_{\mathbf{k}}\left[\frac{\partial\Delta}{\partial T}\left(\frac{\varepsilon_k\Delta}{\mathcal{E}_k^2}\mathcal{F}\left(\mathcal{E}_k\right) + \frac{\varepsilon_k^2}{\mathcal{E}_k^3}f_B(\mathcal{E}_k)\right) - \beta\Delta f_B'(\mathcal{E}_k)\right],\end{aligned} \tag{1.70}$$

where we introduced notation for a frequently used expression:

$$\mathcal{F}\left(\mathcal{E}_k\right) \equiv \frac{f_B(\mathcal{E}_k)}{\mathcal{E}_k} + f_B'(\mathcal{E}_k). \tag{1.71}$$

The expression for

$$\frac{\partial E_2}{\partial T} = \frac{4\left(\Delta m\right)^{3/2}}{3\pi^2}\frac{\partial\Delta}{\partial T} + \sum_{\mathbf{k}}\left(\frac{\partial\Delta}{\partial T}\varepsilon_k\mathcal{F}\left(\mathcal{E}_k\right) - \beta\mathcal{E}_k^2 f_B'(\mathcal{E}_k)\right) \tag{1.72}$$

completes the set of derivatives necessary for evaluation of the specific heat.

The derivative $\partial\Delta/\partial\mu$ can be found by differentiating both sides of the main equation (1.47) with respect to μ. As a result,

$$\frac{\partial\Delta}{\partial\mu} = \frac{1}{1-2U\left(\dfrac{\sqrt{\Delta}m^{3/2}}{\pi^2} - \displaystyle\sum_{\mathbf{k}} \mathcal{F}\left(\mathcal{E}_k\right)\right)}. \tag{1.73}$$

As to $\partial\rho/\partial\mu$, needed for evaluation of the magnetic susceptibility in Eq.(1.58), it is obtained by differentiating the equation $\rho = (\Delta+\mu)/2U$, with respect to μ. This yields

$$\chi(T \le T_{\rm cr}) = \frac{(g\mu_B)^2}{2U}\left(\frac{\partial\Delta}{\partial\mu}+1\right). \tag{1.74}$$

Below we apply these equations to the cusps in the specific heat and susceptibility and to the qualitative effects such as the instability in strong magnetic fields. We will show that at a given temperature, there exists a critical field $H^{\rm cr}_{\rm ext}(T)$, such that when $H_{\rm ext}$ approaches $\geq H^{\rm cr}_{\rm ext}(T)$, the magnetic susceptibility, $\chi(H_{\rm ext},T)$ diverges.

1.3.2 Cusp in the specific heat and magnetic susceptibility near $T_{\rm cr}$

The cusp in the specific heat defined as

$$\Delta C_v = \lim_{T\to T_{\rm cr}-0} C_v(T) - \lim_{T\to T_{\rm cr}+0} C_v(T) \tag{1.75}$$

is an interesting quantity in physics of phase transitions. In accordance with the Ehrenfest classification, a phase transition with the discontinuity in C_v near the transition point, is the second order one. Particularly, it is well-known that [46,47] for the ideal gas ΔC_v near the transition into Bose-Einstein condensation is zero i.e. the specific heat is continuous. We shall illustrate this fact for completeness. The specific heat per particle of the ideal Bose gas is given by [46, 47]

$$C_v^{U=0}(T \le T_{\rm cr}) = \frac{15\zeta(5/2)}{4\zeta(3/2)}\left(\frac{T}{T_{\rm cr}}\right)^{3/2}, \tag{1.76}$$

$$C_v^{U=0}(T > T_{\rm cr}) = \frac{15g_{5/2}(z)}{4g_{3/2}(z)} - \frac{9g_{3/2}(z)}{4g_{1/2}(z)}, \tag{1.77}$$

where $g_p(z)$ is defined as:

$$g_p(z) = \frac{1}{\Gamma(p)}\int_0^\infty dx \frac{x^{p-1}}{z^{-1}e^x - 1}, \tag{1.78}$$

related to the Riemann function as $\zeta(p) = g_p(z=1)$. When $T \to T_{\rm cr}+0$, the fugacity $z = \exp(\beta\mu) < 1$ tends to unity, i. e. $\lim\limits_{T\to T_{\rm cr}+0} z = 1$ and the second term

in (1.77) vanishes, because of the divergence in $g_{1/2}$, i.e. $g_{1/2}(z) \sim (1-z)^{-1/2}$ in this range, while the first term exactly coincides with (1.76). As a result,

$$\Delta C_v^{U=0} = 0, \tag{1.79}$$

and hence the specific heat of the ideal gas is continuous although being plotted as a function of temperature $C_v^{U=0}(T)$ behaves similarly to the λ curve.

We proceed with calculation of ΔC_v for interacting gas. Bearing in mind that for $T > T_{\rm cr}$ HFB and HFP approximations coincide, from (1.61) we obtain

$$\lim_{T\to T_{\rm cr}+0} C_v(T) = -\beta_{\rm cr} \sum_{\mathbf{k}} \varepsilon_k^2 f_B'(\varepsilon_k). \tag{1.80}$$

For $T < T_{\rm cr}$, C_v is given by Eqs. (1.67)-(1.71). Assuming in the last equations $\mathcal{E}_k = \varepsilon_k$ and $\Delta = 0$, one finds

$$\lim_{T\to T_{\rm cr}-0} \frac{\partial \Delta}{\partial T} = \frac{2\beta_{\rm cr} U}{1 + 2U \sum\limits_{\mathbf{k}} \mathcal{F}(\varepsilon_k)} \sum_{\mathbf{k}} f_B'(\varepsilon_k)\varepsilon_k, \tag{1.81}$$

which is finite. Using (1.81) in (1.69)-(1.71) and setting in (1.67) $\rho = \mu/2U$, $\rho_0 = 0, \rho_1 = \rho, \sigma = 0$, one obtains for the maximum value of the specific heat $\max\{C_v^{\rm HFB}(T)\} \equiv \lim_{T\to T_{\rm cr}-0} C_v(T)$:

$$\lim_{T\to T_{\rm cr}-0} C_v(T) = \sum_{\mathbf{k}} (\mu + \varepsilon_k) \left(\mathcal{F}(\varepsilon_k) \frac{\partial \Delta}{\partial T} - \beta_{\rm cr}\varepsilon_k f_B'(\varepsilon_k) \right). \tag{1.82}$$

Subtracting (1.80) from (1.82) we finally obtain

$$\Delta C_v = \sum_{\mathbf{k}} \left(\mathcal{F}(\varepsilon_k)(\mu + \varepsilon_k) \frac{\partial \Delta}{\partial T} - \mu\beta_{\rm cr}\varepsilon_k f_B'(\varepsilon_k) \right), \tag{1.83}$$

where $\partial\Delta/\partial T$ is given by Eq. (1.81).

In a quite similar way one can calculate the cusp in the susceptibility:

$$\Delta\chi = \frac{(g\mu_B)^2}{2U} \frac{1}{1 + 2U \sum\limits_{\mathbf{k}} \mathcal{F}(\varepsilon_k)}. \tag{1.84}$$

1.3.3 Parabolic dispersion of triplons

For the parabolic dispersion $\varepsilon_k = k^2/2m$, calculations can be done analytically, as presented below. The specific heat is expressed as:

$$\max\{C_v(T)\} = -\beta_{\rm cr}R_1 - \mu\beta_{\rm cr}R_2 + \frac{\partial \Delta}{\partial T}(R_2 + \mu R_3 + R_5), \tag{1.85}$$

$$\lim_{T\to T_{\rm cr}+0} C_v(T) = -\beta_{\rm cr}R_1, \tag{1.86}$$

$$\Delta C_v = \max\{C_v(T)\} + \beta_{\rm cr}R_1 = \frac{\partial \Delta}{\partial T}(R_2 + \mu R_3 + R_5) - \mu\beta_{\rm cr}R_2. \tag{1.87}$$

The cusp can be obtained with form:

$$\Delta\chi = \frac{(g\mu_B)^2}{2U}\frac{\partial\Delta}{\partial\mu}. \tag{1.88}$$

The derivatives $\partial\Delta/\partial T$ and $\partial\Delta/\partial\mu$ can be simplified to:

$$\frac{\partial\Delta}{\partial T} = \frac{2\beta_{\rm cr}UR_2}{1+2UR_3}, \tag{1.89}$$

$$\frac{\partial\Delta}{\partial\mu} = \frac{1}{1+2UR_3}. \tag{1.90}$$

In these formulas we used following notations:

$$R_1 = -\beta_{\rm cr}\sum_{\mathbf{k}} f_B^2(\varepsilon_k)\varepsilon_k^2 e^{\beta_{\rm cr}\varepsilon_k} = -\frac{\zeta(5/2)\Gamma(7/2)}{\sqrt{2}\pi^2}T_{\rm cr}k_T^3, \tag{1.91}$$

$$R_2 = -\beta_{\rm cr}\sum_{\mathbf{k}} f_B^2(\varepsilon_k)\varepsilon_k e^{\beta_{\rm cr}\varepsilon_k} = -\frac{\zeta(3/2)\Gamma(5/2)}{\sqrt{2}\pi^2}k_T^3, \tag{1.92}$$

$$R_3 = \sum_{\mathbf{k}} (f_B'(\varepsilon_k) + f_B(\varepsilon_k)/\varepsilon_k) = -\frac{0.6471\sqrt{2}}{\pi^2}\frac{k_T^3}{T_{\rm cr}}, \tag{1.93}$$

$$R_4 = \sum_{\mathbf{k}} f_B(\varepsilon_k)\varepsilon_k = \frac{\zeta(5/2)\Gamma(5/2)}{\sqrt{2}\pi^2}T_{\rm cr}k_T^3, \tag{1.94}$$

$$R_5 = \sum_{\mathbf{k}} f_B(\varepsilon_k) = \frac{\zeta(3/2)\Gamma(3/2)}{\sqrt{2}\pi^2}k_T^3, \tag{1.95}$$

where we introduced $k_T \equiv \sqrt{mT_{\rm cr}}$ for the characteristic thermal wavevector of triplon at the transition temperature. Taking into account that R_5 is the triplon concentration, we find that Eq.(1.95) is equivalent to Eq.(1.52).

1.4 High-field instability

It is well-known that [48, 49] the dynamic stability of equilibrium system is determined by its excitation spectrum: When the latter becomes imaginary the time evolution of excitations changes qualitatively. In the condensate state the spectrum is given by $\mathcal{E}_k = \sqrt{\varepsilon_k}\sqrt{\varepsilon_k + 2\Delta}$ where Δ is the solution of nonlinear algebraic Eq.(1.47) which may be rewritten as follows

$$\Delta = \mu + \frac{4U(\Delta m)^{3/2}}{3\pi^2} - \frac{U}{\pi^2}\int_0^\infty \frac{\varepsilon_k + 2\Delta}{\mathcal{E}_k} f_B(\mathcal{E}_k)k^2 dk. \tag{1.96}$$

For some set of system parameters U, m and external fields $H_{\rm ext}$, Eq.(1.96) has no real solution and hence the spectrum, as well as the sound speed, become imaginary. Below we investigate the magnetic susceptibility near the instability point and show that it goes to infinity, as expected in these cases, providing the direct experimental test for the instability. This effect can be seen from the fact

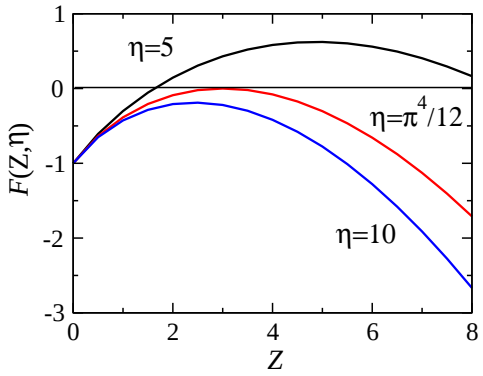

Figure 1.4: The LHS of Eq. (1.100) for different values of η. The real solutions of this equation correspond to the intersection of $F(Z,\eta)$ with the $Z=0$ axis.

that when $H_{\rm ext}=H_{\rm ext}^{\rm cr}$, i. e. $\mu=\mu_{\rm cr}$, the denominator of Eq. (1.73) becomes zero, and hence $\partial\Delta/\partial\mu$ diverges. For $\mu>\mu_{\rm cr}$ the main equation (1.96) has no positive solution and hence the sound speed $c=\sqrt{\Delta}/\sqrt{m}$ becomes complex. Below we illustrate this analytically for $T=0$.

For zero temperature the derivative $\partial\Delta/\partial\mu$ in Eq. (1.73) is written as

$$\frac{\partial\Delta}{\partial\mu}=\frac{1}{1-\dfrac{2U\sqrt{\Delta}m^{3/2}}{\pi^2}}, \tag{1.97}$$

where Δ is the solution to the following equation:

$$\Delta=\mu+\frac{4U(\Delta m)^{3/2}}{3\pi^2}. \tag{1.98}$$

Introducing dimensionless variables $\eta=\mu U^2m^3$ and $Z=\Delta/\mu$ one can rewrite the last two Equations as:

$$\frac{\partial\Delta}{\partial\mu}=\frac{1}{1-\dfrac{2\sqrt{\eta Z}}{\pi^2}}, \tag{1.99}$$

$$F(Z,\eta)\equiv Z-\frac{4Z^{3/2}\sqrt{\eta}}{3\pi^2}-1=0, \tag{1.100}$$

where η is an input parameter. In Figure 1.4 $F(Z,\eta)$ is plotted as a function of Z for various values of η. It is seen that for η larger than some critical $\eta_{\rm cr}$, the second term in (1.100) dominates, $F(Z,\eta)$ is always negative, and hence there is no real solutions. If the maximum value of $F(Z,\eta)$, $(\max\{F(Z,\eta)\})$, for a given η is negative the Eq. (1.100), has no real solution. Otherwise, when $\max\{F(Z,\eta)\}$ is positive, $F(Z,\eta)$ intersects the Z-axis and the equation has at least one positive

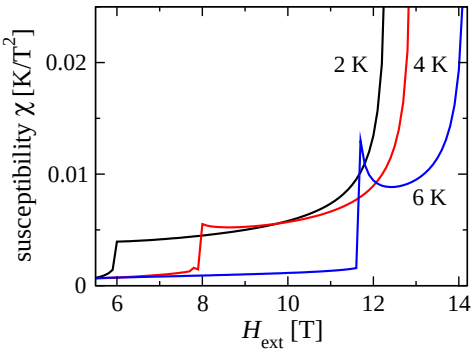

Figure 1.5: The magnetic susceptibility $\chi(T, H_{\rm ext})$ for the temperatures marked near the plots. When external magnetic field reaches the critical value $H_{\rm ext}^{\rm cr}$ the susceptibility diverges.

solution. Thus, the boundaries $\eta_{\rm cr}$ and $Z_{\rm cr}$ are defined by the coupled equations:

$$F(Z_{\rm cr}, \eta_{\rm cr}) = Z_{\rm cr} - \frac{4Z_{\rm cr}^{3/2}\sqrt{\eta_{\rm cr}}}{3\pi^2} - 1 = 0, \tag{1.101}$$

$$\left.\frac{\partial F}{\partial Z}\right|_{Z=Z_{\rm cr},\eta=\eta_{\rm cr}} = 1 - \frac{2\sqrt{Z_{\rm cr}\eta_{\rm cr}}}{\pi^2} = 0, \tag{1.102}$$

giving $\eta_{\rm cr} = \pi^4/12 = 8.1174$ and $Z_{\rm cr} = 3$. By comparing (1.102) and (1.99) one concludes that when η approaches $\eta_{\rm cr}$, $\partial\Delta/\partial\mu$ goes to infinity and so does the magnetic susceptibility given by Eq. (1.74), i.e. χ diverges. When η exceeds $\eta_{\rm cr}$, solutions of Eqs. (1.98), (1.100) acquire an imaginary part. Bearing in mind that $\eta = \mu m^3 U^2 = (\mu_B g H_{\rm ext} - \Delta_{\rm st}) m^3 U^2$, one concludes that at $T = 0$, if the $H_{\rm ext}$ is strong enough the speed of sound $c = \sqrt{\Delta/m} = \sqrt{\mu Z/m}$ becomes complex and the Bose condensed system of triplons displays dynamical instability. By expanding Eq. (1.100) in the vicinity of $Z = Z_{\rm cr}, \eta = \eta_{\rm cr}$, we obtain in this region for the real and imaginary parts of the speed of sound: ${\rm Re}(c) = \sqrt{3\mu_{\rm cr}/m}$ and ${\rm Im}(c)/{\rm Re}(c) = -2\sqrt{\mu - \mu_{\rm cr}} U m^{3/2}/\pi^2$, where $\mu_{\rm cr} \equiv \eta_{\rm cr}/(m^3 U^2)$.

Similarly it can be shown that for any given $T \leq T_{\rm cr}$ there is a maximal value of the external magnetic field $H_{\rm ext}^{\rm cr}$ such that the system posses dynamical instability at this point i.e. $\chi(H_{\rm ext}^{\rm cr}, T_{\rm cr}) \to \infty$ and simultaneously the sound speed acquires an imaginary part. This fact is illustrated in Figs.1.5 and 1.6. In Fig.1.5 the susceptibility $\chi(H_{\rm ext}, T)$ is plotted as a function of $H_{\rm ext}$. In Fig.1.6 the solution of the main equation, more precisely, the components of the sound speed c are plotted as a function of $H_{\rm ext}$ for several temperatures. It is clearly seen that for a given temperature the $\chi(H_{\rm ext}, T)$ diverges and the sound speed becomes complex at the same $H_{\rm ext}$.

Note that in the HFP approximation Eq.(1.100) being written as

$$F_{\rm HFP}(Z, \eta) = Z + \frac{2Z^{3/2}\sqrt{\eta}}{3\pi^2} - 1 = 0 \tag{1.103}$$

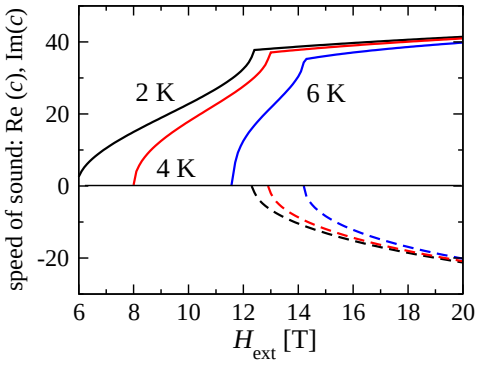

Figure 1.6: The components of the sound speed c for different temperatures, real for $H_{\rm ext} < H_{\rm ext}^{\rm cr}$, and complex out of this range. Real parts Re(c) (solid lines) are positive and Im(c) (dashed lines) are negative. Near the threshold Im(c) demonstrates to the mean-field square root behavior as discussed below Eq.(1.102).

has a positive solution for any positive η. Thus this approximation precludes the appearance of the instability.

The experiment-related results from the observed instability are presented in Fig.1.5 and Fig.1.6. Figure 1.5 shows the divergence in the susceptibility. Figure 1.6 shows how the imaginary part in the velocity appears and the real part of the velocity changes if the field becomes stronger than the threshold value. This is a qualitative effect, which should demonstrate itself in the experiment. Here an important comment on the values of the fields where the singular behavior of Δ can be observed is in order. A comparison of the calculations presented in Fig.1.3, experimental results [33, 44, 45], and theory taking into account the exact spectrum of triplons [30], shows that our model spectrum leads to an overestimate of the tiplon concentration by about a factor of 1.5. Therefore, it underestimates the threshold field, leading to the result that fields of the order of 20 T will be necessary [50] to put the condensate in the unstable part of the phase diagram.

We mention two characteristic features of the instability considered in this section. First, it is not a hydrodynamical instability arising in the inhomogeneous flow of the Bose-Einstein condensate [51–54]. Second, it is not directly related to the interaction between sound-like excitations [55] since we are still in the mean field approximation, and the Hamiltonian we consider does not contain higher-order products of the phonon operators. Nevertheless, both these effects can be studied taking into account the anomalous averages in the theory.

Summarizing this section we conclude that there are two characteristic values of $H_{\rm ext}$. First, when the triplons form the Bose-Einstein condensation, $H_{\rm ext}^{\rm BEC}$ and second, $H_{\rm ext}^{\rm cr} > H_{\rm ext}^{\rm BEC}$, when the Bose-Einstein condensation displays dynamical instability. The phase diagrams for different repulsion parameters U for relativistic triplon dispersion are shown in Fig. 1.7. The localization of the stable Bose-Einstein condensation phases on the $(T, H_{\rm ext})$ plane depends on the model parameters $(m, U, \Delta_{\rm st})$. One can conclude that increasing of U decreases $H_{\rm ext}^{\rm BEC}$

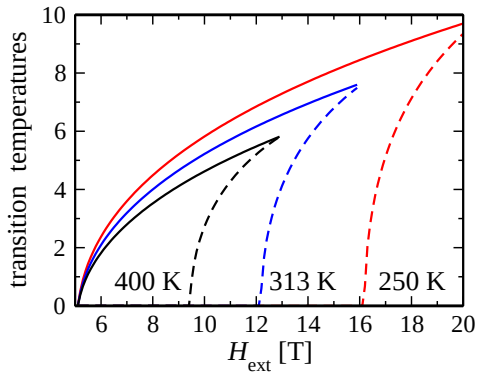

Figure 1.7: The instability borders (dashed lines) as well as the condensate formation borders (solid lines) for different U. With the increase in U the area corresponding to the stable condensate decreases.

and makes the Bose-Einstein condensation less stable, as expected from the fact that the instability is caused by the magnon-magnon repulsion.

Chapter 2

The effects of disorder in dimerized quantum magnets

In this Chapter we study the effects of disorder on Bose-Einstein condensates of triplon quasiparticles in doped dimerized quantum magnets. The condensation occurs in a strong enough magnetic field, where the concentration of bosons in the random potential is sufficient to form the condensate. The effect of doping is partly modeled by a δ - correlated distribution of impurities, which (i) leads to renormalization of the system parameters and (ii) produces disorder in the system with renormalized parameters. This approach can explain qualitatively the available magnetization data on the $Tl_{1-x}K_xCuCl_3$ compound taken as an example. In addition to the magnetization, we found that the speed of the Bogoliubov mode has a maximum as a function of disorder parameter x. No evidence of the pure Bose glass phase has been found in the BEC regime.

2.1 Introduction

The effects of disorder on the properties of Bose-Einstein condensates present interesting problems for theoretical and experimental physics [62–68]. Disorder is important in various systems of real particles such as superfluid ^{4}He, cold atoms in optical lattices, and quasiparticles such as polaritons [69] and excitons [70]. These systems are well-suited for experimental studies, however the theory of disordered ensembles of interacting bosons is complex and there are essentially no exact solutions even in one dimension [71]. To approach this problem, Yukalov and Graham (YG) developed a self-consisted stochastic mean field approximation (MFA) [72,73] for Bose systems with arbitrarily strong interparticle repulsion and arbitrary strength of disorder potential. It was shown that, in general, the Bose system consists of following coexisting components: the condensate fraction, ρ_0, the normal fraction ρ_N, the glassy fraction ρ_G, and, in addition, can be characterized by the superfluid density ρ_s. In the limit of asymptotically weak interactions and disorder the known results, obtained in pioneering work by Huang and Meng [74] (HM) are reproduced by the YG theory. An interesting question here concerns the problem about the existence of a pure Bose glass (BG) phase, i.e. the phase where the condensate fraction is nonzero, while the superfluid fraction is not yet present. Note that Ref. [68] introduced an alternative definition of the gapless BG phase, having localized short-lived excitations and vanishing superfluid density with a continuous transition to the normal phase at finite temperature. Even without disorder, the condensate is depleted by particle-particle interactions and temperature. The inclusion of random fields depletes the condensate further and, possibly, creates the glassy fraction.

In the magnets, the effect of disorder, which can be produced by admixing of other chemical elements, can be sufficiently strong to be seen in the physical properties such as the temperature-dependent magnetization. So far the most investigated compound showing BEC of triplons is $TlCuCl_3$. To study the effect of disorder, solid solutions of quantum antiferromagnets $TlCuCl_3$ and $KCuCl_3$, i.e. $Tl_{1-x}K_xCuCl_3$ have been experimentally investigated [75–77] at low temperatures. The zero-field ground states of $TlCuCl_3$ and $KCuCl_3$ are spin singlets with excitation gaps $\Delta_{\rm st} = 7.1$ K and $\Delta_{\rm st} = 31.2$ K, respectively and the magnetic excitations are spin triplets. In the solid solution $Tl_{1-x}K_xCuCl_3$ the induced magnetization M exhibits a cusplike minimum at a critical temperature $T_{\rm cr}(H_{\rm ext})$ for fixed magnetic field $H_{\rm ext} \geq H_{\rm ext}^{\rm cr}$ similarly to the parent compound corresponding to the triplon BEC [27, 33, 44, 45].

For a theoretical description it is natural to assume that for a weak doping $x \ll 1$ in the $Tl_{1-x}K_xCuCl_3$ system a small admixture of potassium forms a disorder potential. Consequently, recently developed theories of "dirty bosons" [62, 63, 72–74] can be applied to study the BEC of triplons in $Tl_{1-x}K_xCuCl_3$. Here the following natural questions arise. For example, what is the correspondence between admixing parameter x and the properties of the disorder potential? And what are the experimental consequences of the disorder? Yamada *et al.* [76] analyzed the electron spin resonance in $Tl_{1-x}K_xCuCl_3$ and concluded that there is a Bose glass - BEC transition near a critical magnetic field. Although this interpretation might

need a further analysis (see discussion in Refs. [78,79]) it is interesting to study the influence of the possible glassy phase, or more exactly, of the glassy fraction ρ_G on the magnetization. Note that even the existence of a pure Bose glass phase still is a matter of debate even in theoretical approaches. For example, it may be predicted by the approach used by Huang and Meng [74] if one extends their formulas from weak disorder to a strong one. On the other hand, no pure Bose glass was found in Monte - Carlo simulations [80] for atomic gases, although predicted for triplons at $T = 0$ in Ref. [81].

Here we develop a theory of the disorder effects on the BEC of triplons taking $Tl_{1-x}K_xCuCl_3$ as a prototype for studies of specific properties.

2.2 Yukalov-Graham approximation for disordered triplons

In the following we reformulate the Yukalov-Graham approximation for the triplon system with an arbitrary disorder. The Hamiltonian (cf. Eq. (1.1)) operator of triplons with repulsive interaction and implemented disorder potential $\mathcal{V}(\mathbf{r})$ is given by:

$$\hat{H} = \int d^3r \left[\hat{\psi}^\dagger(\mathbf{r}) \left(\hat{K} - \mu + \mathcal{V}(\mathbf{r}) \right) \hat{\psi}(\mathbf{r}) + \frac{U}{2} \left(\hat{\psi}^\dagger(\mathbf{r}) \hat{\psi}(\mathbf{r}) \right)^2 \right]. \qquad (2.1)$$

We adopt the units $k_B \equiv 1$, $\hbar \equiv 1$, and $V \equiv 1$ for the unit cell volume if not stated otherwise.

To describe Bose condensed system where the global gauge symmetry is broken, one employs the Bogoliubov shift (1.4) as in Chapter 1. In this Chapter we assume that the bare spectrum remains coherent in the presence of disorder and consider it as a simple isotropic one: $\varepsilon_{\mathbf{k}} = k^2/2m$, where m is the triplon effective mass. The YG approximation is formulated in representative ensemble formalism, which includes two Lagrange multipliers, μ_0 and μ_1, defined as:

$$N_0 \equiv -\frac{\partial \Omega}{\partial \mu_0}, \quad N_1 \equiv -\frac{\partial \Omega}{\partial \mu_1}, \qquad (2.2)$$

where Ω is the grand thermodynamic potential. It was shown that disorder would not change the explicit expressions for chemical potentials, obtained earlier [29] in Hartree-Fock-Bogoliubov (HFB) approximation without disorder,

$$\mu_0 = U(\rho + \rho_1 + \sigma), \quad \mu_1 = U(\rho + \rho_1 - \sigma), \qquad (2.3)$$

where $\sigma = \dfrac{1}{V} \displaystyle\int_V d^3r \langle \delta\hat{\psi}(\mathbf{r}) \delta\hat{\psi}(\mathbf{r}) \rangle$ is the anomalous density. The total chemical potential μ, related to the total number of particles as $N = -\partial\Omega/\partial\mu$, is determined by

$$\mu\rho = \mu_1\rho_1 + \mu_0\rho_0. \qquad (2.4)$$

Clearly, when the gauge symmetry is not broken, i.e. $\rho_0 = 0$, $\sigma = 0$, $\rho_1 = \rho$, both μ_0 and μ_1 coincide giving $\mu = \mu_1 = 2U\rho$.

As we said in Chapter 1, the magnetization is proportional to the triplon density, that is

$$M = g\mu_B \rho \tag{2.5}$$

with ρ is defined in (2.4) as

$$\rho = \frac{1}{\mu}\left(\mu_1\rho_1 + \mu_0\rho_0\right), \tag{2.6}$$

where μ_0 and μ_1 are given in (2.3) and the densities ρ_0, ρ_1 must be calculated self consistently.

It is well known [82] that the disorder field leads to formation of a glassy fraction with the density ρ_G. In this approximation each of ρ_1 and σ are presented as

$$\rho_1 = \rho_N + \rho_G; \quad \sigma = \sigma_N + \rho_G, \tag{2.7}$$

where ρ_N and σ_N are the normal and anomalous densities without disorder. In the YG method, based on HFB approximation, the following explicit relations can be obtained as (1.44) and (1.45):

$$\rho_N = \frac{(\Delta m)^{3/2}}{3\pi^2} + \int \frac{d^3k}{(2\pi)^3} f_B(\mathcal{E}_k)\frac{\varepsilon_k + \Delta}{\mathcal{E}_k}, \tag{2.8}$$

$$\sigma_N = \frac{(\Delta m)^{3/2}}{\pi^2} - \Delta \int \frac{d^3k}{(2\pi)^3} f_B(\mathcal{E}_k)\frac{1}{\mathcal{E}_k}, \tag{2.9}$$

with the Bose distribution of Bogoliubov excitations $f_B(\mathcal{E}_k) = 1/(e^{\mathcal{E}_k/T} - 1)$ having the dispersion $\mathcal{E}_k = \sqrt{\varepsilon_k}\sqrt{\varepsilon_k + 2\Delta}$ and the speed of the Bogoliubov mode is $c = \sqrt{\Delta/m}$ as defined in Eqs. (1.32) and (1.33) correspondingly.

The self energy Δ is determined formally by the same Equation as in the case when the disorder is neglected,

$$\Delta = U(\rho_0 + \sigma) = U(\rho - \rho_N + \sigma_N). \tag{2.10}$$

The contribution from the disorder potential is hidden in the density of the glassy fraction

$$\rho_G = \frac{1}{V}\int_V d^3r \langle\langle \delta\hat{\psi}(\mathbf{r})\delta\hat{\psi}(\mathbf{r})\rangle\rangle \tag{2.11}$$

where the double brackets mean the ensemble average. In general, the calculation of ρ_G is rather complicated, however, for the δ - correlated disorder i.e. for the white noise (we assume $\langle\mathcal{V}(\mathbf{r})\rangle = 0$),

$$\langle\langle \mathcal{V}(\mathbf{r})\mathcal{V}(\mathbf{r}')\rangle\rangle = R\delta(\mathbf{r} - \mathbf{r}'), \tag{2.12}$$

equation (2.11) is simplified as [72, 73]

$$\rho_G = \frac{R_0(\rho - \rho_N)}{R_0 + 7(1 - R_0)^{3/7}}. \tag{2.13}$$

The density of condensed fraction can be found by inserting (2.7) and (2.13) into the normalization condition $\rho = \rho_0 + \rho_1$. The result is

$$\rho_0 = \frac{7(1-R_0)^{3/7}(\rho - \rho_N)}{R_0 + 7(1-R_0)^{3/7}}. \tag{2.14}$$

In Eqs. (2.13) and (2.14) we introduced the dimensionless parameter R_0 as

$$R_0 \equiv \frac{7Rm^2}{4\pi\sqrt{m\Delta}}. \tag{2.15}$$

One can see from Eqs. (2.13) and (2.14) that the glassy fraction is proportional to the condensed one,

$$\rho_G = \frac{R_0}{7(1-R_0)^{3/7}}\rho_0. \tag{2.16}$$

The system of Eqs. (2.3), (2.4), (2.8)-(2.12) are the basic of YG approximation.

An interesting quantity, crucial for determining the Bose glass phase, is the superfluid density, ρ_s. In general it is defined as a partial density appearing as a response to a velocity

$$\rho_s = \frac{1}{3mV}\lim_{\mathbf{v}\to 0}\frac{\partial}{\partial \mathbf{v}}\langle \hat{\mathbf{P}}_{\mathbf{v}}\rangle \tag{2.17}$$

where $\hat{\mathbf{P}}_{\mathbf{v}}$ is the total momentum of the system, dependent on the macroscopic velocity $\mathbf{v}$. Following papers [72–74], we bring below analytical expression obtained there for ρ_s in the case of white noise random potential

$$\rho_s = \rho - \frac{4\rho_G}{3} - \frac{2Q_N}{3T}, \tag{2.18}$$

$$Q_N = \frac{1}{8m}\int \frac{k^2 d^3k}{(2\pi)^3 \sinh^2(\mathcal{E}_k/2T)}. \tag{2.19}$$

Note that YG approach is valid for arbitrary strength of the interaction potential U, and for arbitrary strong disorder. For the weak interactions it leads to Huang-Meng approach [74], which will be extended to the "dirty triplons" in the next section.

2.3 Huang-Meng approximation

For completeness, we present here the results for the Huang-Meng approach, based on the HFP approximation which has been widely applied in the literature to describe the BEC of triplons [33, 44, 45]. The basic equations of this approach can be obtained by neglecting the anomalous density σ, which leads naturally to the single chemical potential $\mu = \mu_0 = \mu_1$. Namely, one finds from (2.3), (2.4) and (2.10)

$$\Delta = U\rho_0, \qquad \mu = U(\rho + \rho_1). \tag{2.20}$$

From these equations and (2.7) one obtains following main equations for the self energy Δ:

$$\Delta = \mu - 2U(\rho_N + \rho_G), \tag{2.21}$$

where ρ_N is formally given in (2.8), and ρ_0 is determined by the first equation in (2.20). The glassy fraction can be obtained from (2.13) in the linear approximation by R assuming weakness of interparticle interaction [72–74]

$$\rho_G = \frac{m^2 R}{8\pi^{3/2}} \left(\frac{\rho_0}{a_s}\right)^{1/2}, \tag{2.22}$$

where $a_s = Um/4\pi$ is the s - wave scattering length. Inserting (2.22) into (2.21) we can rewrite the former as

$$\Delta = \mu - 2U\rho_N - \frac{m^2 R\sqrt{\Delta}}{2\pi\sqrt{m}}. \tag{2.23}$$

To evaluate the densities one has to solve nonlinear algebraic equation (2.23), where ρ_N is given formally by (2.8), with respect to Δ. Next, by inserting the result into (2.20) and (2.22) one obtains the density of condensed triplons ρ_0 and the glassy fraction ρ_G, respectively. The total density can be evaluated then by the normalization condition $\rho = \rho_0 + \rho_N + \rho_G$. Equations (2.18), (2.19) for the superfluid density are formally the same in both approximations.

2.4 The shift of $T_{\rm cr}$ and $T > T_{\rm cr}$ regime

As we consider in the section 1.2.3 the total density near the critical temperature (1.52) is defined by:

$$\rho_{\rm cr} = \mu/2U, \tag{2.24}$$

which is directly follows, from Eqs. (2.3), (2.4) or (2.21) by setting $\rho_N = \rho$ and $\rho_0 = \rho_G = 0$.

Clearly, any type of interaction is expected to modify $T_{\rm cr}$. In general, these modifications are related to the interparticle interactions as well as to the disorder potential. Both approaches, considered here give a zero shift due to the boson-boson repulsion. However the shift due to the $\delta-$correlated disorder (2.12), $\Delta T_{\rm cr} = T_{\rm cr} - T^0_{\rm cr}$ is given as [72, 73, 83]

$$\frac{\Delta T_{\rm cr}}{T^0_{\rm cr}} = -\frac{2\nu}{9\pi}, \tag{2.25}$$

where the dimensionless disorder parameter ν

$$\nu \equiv \frac{1}{\rho_{\rm cr}^{1/3} L_{\rm loc}}, \tag{2.26}$$

is introduced with the localization length

$$L_{\rm loc} = \frac{4\pi}{7m^2 R}. \tag{2.27}$$

For practical calculations we rewrite $T_{\rm cr}$ in Eq. (2.25), which is in a good agreement with perturbative estimates [63] as well as with Monte Carlo simulations [84],

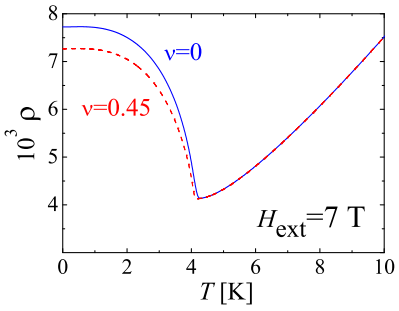

Figure 2.1: The total triplon density as a function of temperature in the YG approximation for two values of ν. Here the following set of parameters $H_{\rm ext} = 7$ T, m=0.0204 K^{-1}, $\Delta_{\rm st} = 7.3$ K, $U = 313$ K, and $g = 2.06$ [33] valid for $TlCuCl_3$ is used.

as an explicit function of effective mass m, the interaction strength U, critical magnetic field $H_{\rm ext}^{\rm cr}$, disorder parameter ν, and external field $H_{\rm ext}$ as follows:

$$T_{\rm cr} = \frac{9\pi - 2\nu}{9m}\left(\frac{\sqrt{2}g\mu_B(H_{\rm ext} - H_{\rm ext}^{\rm cr})}{U\zeta(3/2)}\right)^{2/3}. \tag{2.28}$$

Now we proceed to consider the triplon density in the normal state in the $T - T_{\rm cr} \gg \Delta T_{\rm cr}$ temperature range. The dirty bosons in the normal phase where the gauge symmetry is not broken, are yet poorly understood. For $R = 0$ with $\rho_0 = \rho_G = \sigma = 0$ the triplon gas behaves like an "ideal gas" with an effective chemical potential $\mu_{\rm eff}$, and the density [11] is defined by Eq. (1.54). Although $\mu_{\rm eff}$ is not accurately known it depends in general, on ρ, as well as on R. For the pure case MFA [11] gives $\mu_{\rm eff}(R = 0) = \mu - 2U\rho$. The contribution from the disorder potential has been studied neither in YG nor in HM approaches. Therefore, to make the calculations self consistently, we have to use

$$\rho(T > T_{\rm cr}) = \int \frac{d^3k}{(2\pi)^3}\frac{1}{\exp\left((\varepsilon_k - \mu - 2U\rho)/T\right) - 1}, \tag{2.29}$$

which yields the density ρ as a solution of the nonlinear equation (2.29).

2.5 Results and discussion

In the calculations below, the strength of disorder potential R, has units K^{-2} while the disorder parameter ν, defined in Eq. (2.26) is supposed to be less than one, $\nu < 1$.

To perform numerical calculations in the YG approximation, assuming that μ, U, m, and R are given parameters, we use following approach. (i) By inserting

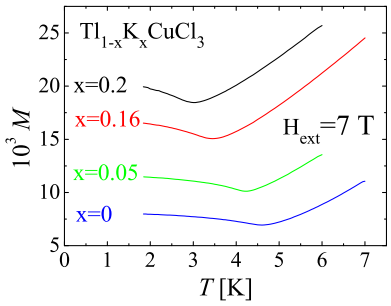

Figure 2.2: The experimental low temperature magnetization in units of Bohr magneton per Cu ion of $Tl_{1-x}K_xCuCl_3$ for various x in $H_{\rm ext} = 7$ T magnetic field obtained in Ref. [75].

(2.3), (2.7), (2.13) and (2.14) into (2.6) we obtain quadratic algebraic equation with respect to ρ and solve it analytically. (ii) By using this $\rho(\mu, R, \Delta)$ and (2.8), (2.9) in (2.10) we solve the latter numerically with respect to Δ, and (iii) by inserting this Δ back into $\rho(\mu, R, \Delta)$ we find the magnetization from (2.5) and evaluate other densities like ρ_0 and ρ_G from (2.13) and (2.14).

In Figure 2.1 we present as an example the total triplon density $\rho(T)$ for a clean and strongly disordered ($\nu = 0.45$, see Eq.(2.26)) $TlCuCl_3$, obtained in the YG approximation assuming that the total effect of the doping leads only to the randomness in the triplon subsystem.

The calculation of other quantities using the same assumptions shows that the disorder leads to a decrease in the condensed and superfluid fractions, thereby increasing the glassy one. This tendency is quite natural, since the localization effects prevent particles from going into BEC. However, the increase in ρ_G is so weak that along with ρ_0 the total number of triplons ρ is also decreased with increasing the strength of disorder potential R. Bearing in mind that M is proportional to the magnetization ρ, and ν is assumed to be approximately proportional to x, and comparing Fig.2.1 with the experimental data illustrated in Fig.2.2 one may conclude that the agreement between the theory and the experiment is unsatisfactory since the main features of the experimental results are not reproduced there. As it is seen in Fig.2.2, the disorder leads to an increase in the magnetization and, hence, in the total triplon density. This is accompanied by the decrease in the transition temperature. We therefore conclude that while the triplon gas can be considered similarly to atomic gases for which the considered mean-field approximations were developed, some further additional specific material - related properties of the dirty boson problem in quantum magnets must be taken into account.

First we note that the singlet - triplet excitation gap $\Delta_{\rm st}$, proportional to the critical field, $H_{\rm ext}^{\rm cr}$, decreases under high pressure. This was experimentally observed in Ref. [85–87] for the pure spin system $TlCuCl_3$. On the other hand it

Table 2.1: Optimized values of the input parameters of the model: the critical field, $H_{\rm ext}^{\rm cr}$ (taken from Ref. [75]), the disorder parameter ν, and the effective mass m for various doping x. The critical density, $\rho_{\rm cr}$, the healing length, $\lambda = 1/\sqrt{2m\mu}$, the interparticle distance, $d = 1/\rho_{\rm cr}^{1/3}$ and the localization length, $L_{\rm loc} = d/\nu$ are estimated at $H_{\rm ext} = 7$ T. It is assumed that the doping does not modify the Landé factor g and U. In the table λ, d and $L_{\rm loc}$ are measured in nanometers (nm).

x	ν	$H_{\rm ext}^{\rm cr}$ [T]	m [K^{-1}]	$\Delta_{\rm st}$ [K]	$\rho_{\rm cr}$	λ	d	$L_{\rm loc}$
0	0	5.3	0.020	7.3	0.0038	2.55	5.08	∞
0.05	0.16	4.8	0.024	6.6	0.0049	2.04	4.64	28.4
0.08	0.25	4.4	0.029	6.1	0.0059	1.71	4.38	17.7
0.16	0.48	4.1	0.039	5.6	0.0065	1.40	4.23	8.86
0.20	0.59	3.9	0.044	5.4	0.0068	1.28	4.16	7.09

can be argued that the doping acts as a chemical pressure, which decreases $H_{\rm ext}^{\rm cr}$. In fact, since the ionic radius of K^+ is smaller than that of Tl^+, a partial substitution of Tl^+ ions with K^+ ions produces not only the exchange randomness, but also a compression of the crystal lattice. Thus the increase in the doping parameter x leads to decrease in $H_{\rm ext}^{\rm cr}$ which has indeed been observed experimentally [75, 88–90]. Second, as it was shown long ago for helium in porous media [91] the disorder may increase the effective mass and decreases the critical temperature, $T_{\rm cr}$. Below we call this direct modification of internal parameters of the model as a direct doping effect (DDE). Note that this effect manifests itself in different ways. For example, for the mixed compound IPACu$(Cl_xBr_{1-x})_3$ the critical field, $H_{\rm ext}^{\rm cr}$ remains almost unchanged with varying x and then, abruptly becomes zero near the Cl-rich phase [92]. In another triplon-BEC compound, Ni$(Cl_{1-x}Br_x)_2$-4SC$(NH_2)_2$, it decreases by a factor of two when x changes from zero to 0.08 [89,90] although the physics of this decrease can be different from that in $Tl_{1-x}K_xCuCl_3$ due to the fact that Br atomic radius is larger than the atomic radius of Cl. These effects of renormalization of the triplon spectrum by disorder can be considered similarly to the virtual crystal approximation in the simulations of disorder in solids, where the disorder is assumed to lead to a uniform change in the system parameters. The effects of disorder such as the appearance of the glassy phase with the density ρ_G and related phenomena manifest themselves in addition to these uniform changes.

The phase diagram of $Tl_{1-x}K_xCuCl_3$ in the $(H_{\rm ext}, T)$ plane was experimentally determined in Refs. [75, 88] for various x, and the critical field $H_{\rm ext}^{\rm cr}$ was also estimated by extrapolation to zero temperature. In the present work the $T_{\rm cr}(H_{\rm ext})$ dependence is given by Eq. (2.28). We perform a least - square fit parameters m and ν by using Eq. (2.28) to describe the experimental phase diagram. For simplicity we assume that interparticle interaction is not changed by doping, i.e. $U = U(R = 0) = 313$ K. The parameters obtained by this optimization are presented in Table 2.1.

Having fixed the input parameters for certain values of x, we are now at the

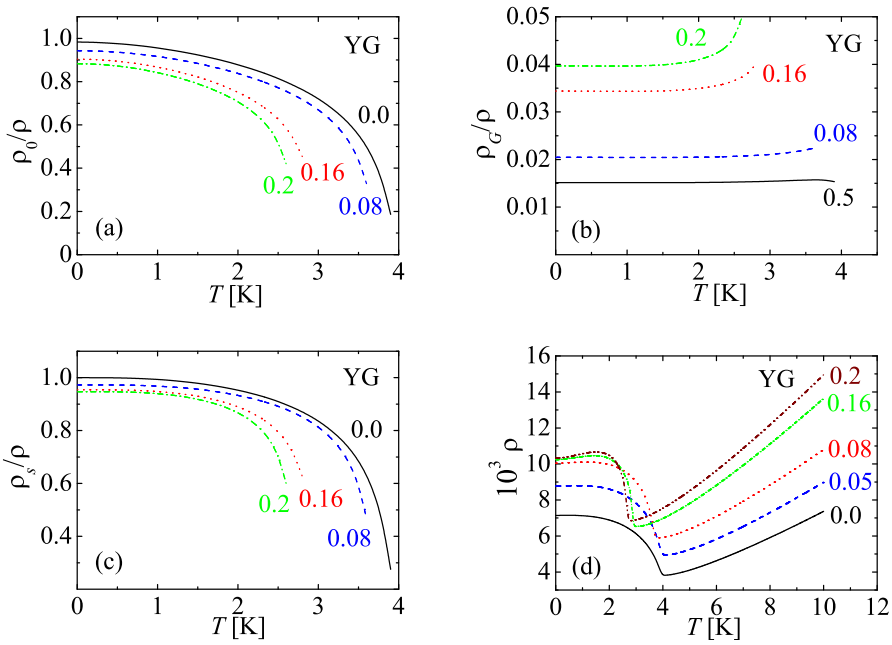

Figure 2.3: The condensed (a), glassy (b), superfluid fractions (c), and total density of triplons (d) as functions of temperature in the YG approximation for $H_{\rm ext} = 7$ T and various x marked near the plots with the input parameters from Table 2.1.

position of recalculating the densities as well the magnetization to compare them with the experiment. Figure 2.3 shows that the doping decreases ρ_0 and ρ_s, and increases ρ_G as it is expected due to the introduced disorder. Due to change of $H_{\rm ext}^{\rm cr}$ with x, the total density of triplons and hence the magnetization, now increases with increasing x in accordance with the experiment. One may conclude that the YG approach may well describe the effect of disorder to the magnetization, with the additional assumption of an x dependence of the effective mass and the critical field.

One of the main characteristics of Bose condensed systems is the speed of the Bogoliubov mode c, which characterizes the propagation of collective excitations in the condensate. It is interesting to mention that the magnitude of c is large, being only an order of magnitude less than the speed of sound in the crystal. This is due to very small triplon effective mass in $TlCuCl_3$. Clearly, disorder modifies the small-momentum excitation spectrum of the BEC. Estimates of such modification, $\Delta c = c - c_0$, where c_0 is the speed of the Bogoliubov mode for the pristine system, that exist in the literature are controversial. For example, perturbative [62] and hydrodynamic [64] approaches give $\Delta c > 0$, while $\Delta c < 0$ was predicted in Refs. [65–67]. In Fig. 2.4 we present the corresponding speed for various doping parameters. It can be seen from comparison of Fig.2.4(a) and

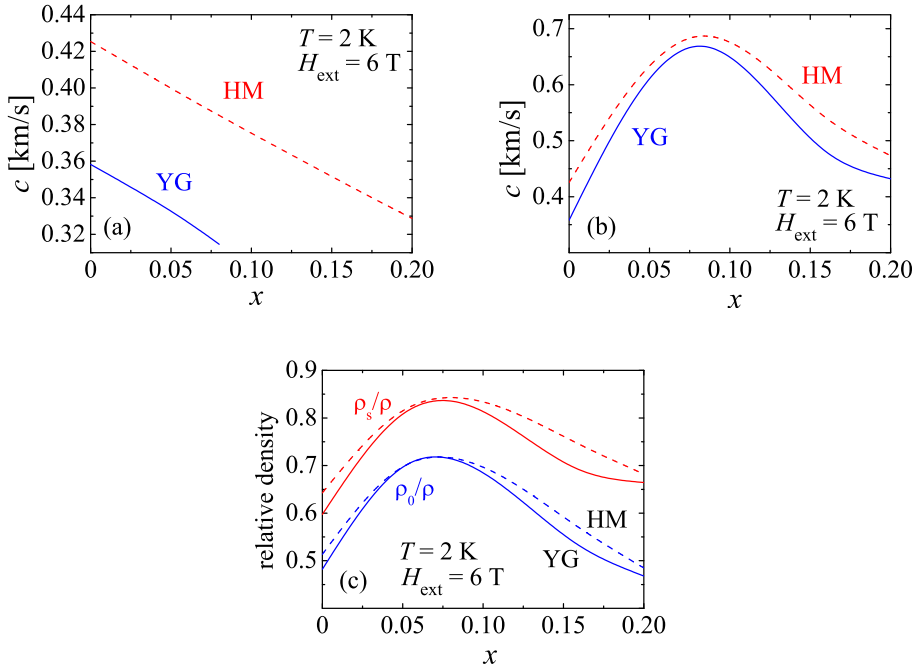

Figure 2.4: (a) The speed of sound-like condensate mode at $T = 2$ K and $H_{\rm ext} = 6$ T as a function of doping parameter x, without taking into account renormalization of the system parameters in the YG (solid line) and the HM (dashed line) approaches. (b) The same as in Fig. 2.4(a), now with effects of disorder taken into account. (c) The superfluid and condensed fractions (as marked near the plots) in the YG (solid lines) and the HM (dashed lines) approximations with the renormalized bare spectrum parameters.

Fig.2.4(b) that both MFA approximations considered here show the decrease in c with increasing the disorder strength due to the localization effects. However, the effect of disorder is small leading to a less than 10 percent decrease in the speed of the Bogoliubov mode.

However, when the spectrum modification by disorder is also taken into account by a renormalization of the triplon mass and the gap, as close to the real situation, the dispersion of the sound-like mode in fixed magnetic field slightly increases with increasing disorder, reaches a maximum and then starts to decrease, see Fig.2.4(b). This behavior is caused by interplay between renormalization of the system parameters and localization effects. The former tends to increase c, e.g. by increasing μ, and therefore increasing the density, while the latter tends to decrease c, e.g. by decreasing the condensed fraction. Note that an increase in c with increasing the density was experimentally observed by Andrews *et al.* [93] for the BEC of sodium atoms. This interplay is illustrated in Fig.2.4(c) for ρ_0 and ρ_s. It can be seen that uniform spectrum renormalization first leads to an

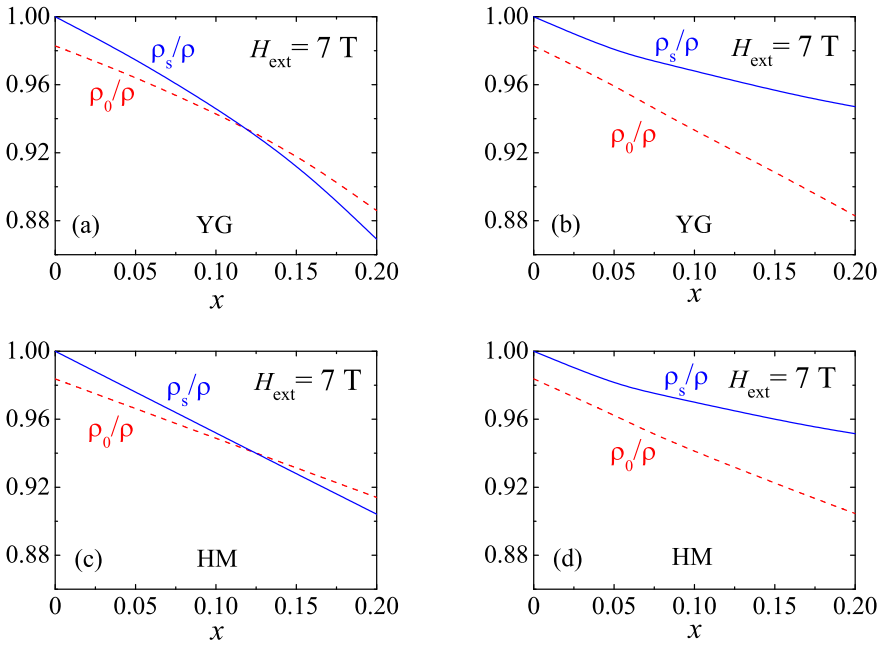

Figure 2.5: The superfluid, ρ_s/ρ (solid lines) and condensed, ρ_0/ρ (dashed lines), fractions as a function of the doping parameter x at $T = 0$, $H_{\rm ext} = 7$ T. Upper panel corresponds to the YG approximation and lower panel corresponds to the HM approximation presented here for comparison. Graphs in plots (a), (c) were calculated without bare spectrum renormalization, while graphs in plots (b), (d) take into account spectrum renormalization presented in Table 2.1.

"antidepletion" effect, increasing these quantities, while the localization effects impair the condensation and superfluidity.

We now consider the question about the existence of a pure Bose glass phase at $T = 0$, which, strictly speaking, should fulfill the following criteria [72, 73, 82, 94]: (i) gapless in the excitation spectrum, (ii) insulating behavior, i.e. the superfluid fraction, $\rho_s = 0$, (iii) finite compressibility, and (iv) finite density of states.

In 1970, Tachiki and Yamada [3] have shown that the Heisenberg-like Hamiltonian of $s = 1/2$ dimers can be rewritten as an effective bosonic Hamiltonian. Recently, Roscilde and Haas [95] generalized this bosonization procedure taking into account disorder and derived a Bose - Hubbard like Hamiltonian usually applied to study "dirty bosons" in optical lattices. Applying Fishers ideas [82] we may expect the formation of a pure Bose glass phase for doped magnets such as $Tl_{1-x}K_xCuCl_3$. Although Monte Carlo calculations [81,95] confirmed its existence the experimental confirmation is still a matter of debate [78, 79, 96]. We underline here that these Bose glass phases are localized out of the BEC phase, i.e. for $H_{\rm ext} < H_{\rm ext}^{\rm cr}$. However, in the present work we have been mainly concentrating on the region with $H_{\rm ext} \geq H_{\rm ext}^{\rm cr}$ where the gapless phase can be realized only within

the BEC phase. For this case the definition of BG phase may be simplified as a phase with $\rho_0 \neq 0$ and $\rho_s = 0$ since the spectrum of the BEC is gapless by itself. In searching for such a phase we studied ρ_s and ρ_0 at $T = 0$ for various $H_{\rm ext} \geq H_{\rm ext}^{\rm cr}$ and x and found no pure BG phase with $\rho_s = 0$ as illustrated in Fig. 2.5.

Note also that, as it is seen from Table 2.1, for moderate values of x considered here, the localization length, i.e the mean free path [97] is larger than interparticle distance, $L_{\rm loc} > d$. The physics of the possible BG phase for $H_{\rm ext} < H_{\rm ext}^{\rm cr}$ fields under this condition remains to be investigated.

Part II

BOSE ATOMS IN OPTICAL LATTICES

Chapter 3

Quasiequilibrium itinerant and localized bosons

In this Chapter we study a quasiequilibrium mixture of itinerant and localized bosonic atoms in an optical lattice at zero temperature and at integer filling factor, when such a coexistence is impossible at the equilibrium. The analysis is based on a model equivalent to a two-band, or two-component, boson Hubbard Hamiltonian. The minimal value for the ratio of on-site repulsion to tunneling parameter, necessary for the occurrence of such a mixture, is found.

3.1 Introduction

Here we consider the case of atoms inside an optical lattice, that is a system with an artificial periodic structure, usually, of mesoscopic or nanoscopic size [113]. Optical lattices provide exceptional opportunity for producing various states of periodic matter [94, 98–101]. Here we consider N bosonic atoms in a lattice of N_L sites, with the filling factor $\nu \equiv N/N_L$. The system is characterized by a boson Hubbard Hamiltonian with on-site repulsion U, tunneling parameter J, and the number of nearest neighbors z_0. At zero temperature and an integer filling factor Bose atoms, form either Mott insulating state or superfluid state, depending on the ratio $u \equiv U/z_0J$ of the on-site repulsion U to the product of the tunneling parameter J and the nearest-neighbor number z_0. For a cubic lattice, with $z_0 = 6$ and the unity filling factor ($\nu = 1$), the second-order phase transition between superfluid and insulating states occurs at $u_c = 4.9$, as follows from strong-coupling perturbation theory [102,103] and Monte Carlo simulations [104–106]. At finite temperature and/or noninteger filling factor, localized and delocalized atoms coexist [107–110].

Here we analyze a possible quasiequilibrium coexistence of delocalized (wandering) and localized atoms in a lattice with an integer filling factor at zero temperature. Let us assume that a nonequilibrium state, where a portion of atoms is localized and another portion is not localized has been prepared. This could be achieved in the process of loading atoms into the lattice. A nonequilibrium loading into a double-well optical lattice has been studied in Refs. [111,112]. Suppose that the process of such a nonequilibrium loading lasts the time $t_{\rm non}$ that is longer than the local-equilibrium time $t_{\rm loc}$, but shorter than the relaxation time $t_{\rm rel}$ that is necessary for the system for passing to the total equilibrium, that is

$$t_{\rm loc} \ll t_{\rm non} \ll t_{\rm rel}. \tag{3.1}$$

In this case, in the interval of time $t_{\rm non} \ll t \ll t_{\rm rel}$, the system can be treated as quasiequilibrium, so that the components of the itinerant and localized atoms are in equilibrium with each other, while the system as a whole has not yet been equilibrated, but is changing slowly. To create the quasiequilibrium it is possible to invoke external temporal modulation of the system parameters. Different variants of such a modulation of the parameters of trapped atoms are now discussed in the literature [114–119]. Fortunately, optical lattices are highly controllable objects, whose parameters can be varied in a wide range [94, 98–101]. Since the quasiequilibrium has been assumed, this imposes restrictions on the system parameters at which possible coexistence of itinerant and localized atoms could be realized. Our aim is to find out what are these restrictions and, in particular, the range of the interaction parameter $u = U/Jz_0$, where the coexistence would be admissible.

3.2 Two-band model

To describe the desired coexistence of states, we employ two-component Hubbard Hamiltonian [94], in which one band corresponds to delocalized atoms, while the other band corresponds to localized (bound) atoms. The system, as a whole,

contains $N_0 + N_1$ delocalized atoms, where N_0 is the number of condensed atoms and N_1, the number of uncondensed atoms. The number of localized atoms is N_2. So that the total number of atoms is

$$N = N_0 + N_1 + N_2. \tag{3.2}$$

The corresponding atomic fractions

$$n_0 \equiv \frac{N_0}{N}, \qquad n_1 \equiv \frac{N_1}{N}, \qquad n_2 \equiv \frac{N_2}{N}, \tag{3.3}$$

satisfy the normalization condition $n_0 + n_1 + n_2 = 1$ following from Eq. (3.2).

The field operator of itinerant atoms for the Bose-condensed system in a lattice has the form [121]

$$\hat{\psi}_j = \psi_0 + \delta\hat{\psi}_j. \tag{3.4}$$

with the index $j = 1, 2, \ldots, N_L$ enumerating lattice sites. Here, ψ_0 is the condensate order parameter, defining the density $|\psi_0|^2$, and $\delta\hat{\psi}_j$ is an operator of uncondensed atoms (similar to Eq. (1.3) in Chapter 1). Statistical averages for the operators of uncondensed atoms, $\delta\hat{\psi}_j$, and for those of localized atoms, $\hat{\phi}_j$, are such that

$$\langle\delta\hat{\psi}_j\rangle = \langle\hat{\phi}_j\rangle = 0. \tag{3.5}$$

Thus, the number of itinerant condensed atoms is

$$N_0 = \sum_j |\psi_0|^2 = \nu n_0 N_L, \tag{3.6}$$

the number of itinerant uncondensed atoms is

$$N_1 = \langle\hat{N}_1\rangle = \nu n_1 N_L, \qquad \hat{N}_1 = \sum_j \delta\hat{\psi}_j^\dagger \delta\hat{\psi}_j, \tag{3.7}$$

and the number of localized atoms is

$$N_2 = \langle\hat{N}_2\rangle = \nu n_2 N_L, \qquad \hat{N}_2 = \sum_j \hat{\phi}_j^\dagger \hat{\phi}_j. \tag{3.8}$$

The Hamiltonian has the form of a two-band Hubbard model

$$\hat{H}_{2b} = -J \sum_{\langle ij\rangle} \hat{\psi}_i^\dagger \hat{\psi}_j + \frac{U}{2} \sum_j \left(\hat{\psi}_j^\dagger \hat{\psi}_j^\dagger \hat{\psi}_j \hat{\psi}_j + 2\hat{\psi}_j^\dagger \hat{\psi}_j \hat{\phi}_j^\dagger \hat{\phi}_j + \hat{\phi}_j^\dagger \hat{\phi}_j^\dagger \hat{\phi}_j \hat{\phi}_j \right), \tag{3.9}$$

where in the first term the summation runs over the nearest neighbors. Constructing the grand Hamiltonian, we have to take into account the given normalization conditions, uniquely defining a representative ensemble for the system with broken gauge symmetry [48]. Then the grand Hamiltonian reads as

$$\hat{H} = \hat{H}_{2b} - \mu_0 N_0 - \mu_1 \hat{N}_1 - \mu_2 \hat{N}_2, \tag{3.10}$$

in which the Lagrange multipliers μ_0, μ_1, and μ_2, play the role of partial chemical potentials guaranteeing the normalizations (3.6), (3.7), and (3.8). The system chemical potential is

$$\mu = \mu_0 n_0 + \mu_1 n_1 + \mu_2 n_2. \tag{3.11}$$

However, in the considered case, not all these multipliers are independent. The restriction comes from the assumption that the system is in quasiequilibrium, such that the variation of a thermodynamic potential should be zero. From this condition, we have [94] the relation

$$\mu_2(n_0 + n_1) = \mu_0 n_0 + \mu_1 n_1, \tag{3.12}$$

which yields the chemical potential

$$\mu = \frac{\mu_0 n_0 + \mu_1 n_1}{n_0 + n_1} = \mu_2. \tag{3.13}$$

Atoms from different bands are assumed to be weakly correlated, such that we can use approximation

$$\delta\hat{\psi}_j^\dagger \delta\hat{\psi}_j \hat{\phi}_j^\dagger \hat{\phi}_j = \delta\hat{\psi}_j^\dagger \delta\hat{\psi}_j \langle \hat{\phi}_j^\dagger \hat{\phi}_j \rangle + \langle \delta\hat{\psi}_j^\dagger \delta\hat{\psi}_j \rangle \hat{\phi}_j^\dagger \hat{\phi}_j - \langle \delta\hat{\psi}_j^\dagger \delta\hat{\psi}_j \rangle \langle \hat{\phi}_j^\dagger \hat{\phi}_j \rangle. \tag{3.14}$$

Then the grand Hamiltonian (3.10) takes the form

$$\hat{H} = \hat{H}_{\rm del} + \hat{H}_{\rm loc} - \nu n_1 n_2 NU, \tag{3.15}$$

where the first term describes delocalized itinerant atoms, the second term describes localized atoms, and the third term is responsible for the interaction of atoms from different bands.

By substituting there the Bogoliubov shift (3.4), we obtain the Hamiltonian of delocalized atoms

$$\hat{H}_{\rm del} = \sum_{n=0}^{4} \hat{H}^{(n)}, \tag{3.16}$$

with the zero-order term

$$\hat{H}^{(0)} = \left(-z_0 J + \frac{U}{2} \nu n_0 - \mu_0 \right) n_0 N, \tag{3.17}$$

first-order term

$$\hat{H}^{(1)} = 0, \tag{3.18}$$

second-order term

$$\hat{H}^{(2)} = -J \sum_{\langle ij \rangle} \delta\hat{\psi}_j^\dagger \delta\hat{\psi}_j + (2\nu n_0 U + \nu n_2 U - \mu_1) \sum_j \delta\hat{\psi}_j^\dagger \delta\hat{\psi}_j +$$
$$\nu n_0 \frac{U}{2} \sum_j \left(\delta\hat{\psi}_j^\dagger \delta\hat{\psi}_j^\dagger + \delta\hat{\psi}_j \delta\hat{\psi}_j \right). \tag{3.19}$$

third-order term

$$\hat{H}^{(3)} = \sqrt{\nu n_0} U \sum_j \left(\delta\hat{\psi}_j^\dagger \delta\hat{\psi}_j^\dagger \delta\hat{\psi}_j + \delta\hat{\psi}_j^\dagger \delta\hat{\psi}_j \delta\hat{\psi}_j \right). \tag{3.20}$$

and the fourth-order term

$$\hat{H}^{(4)} = \frac{U}{2} \sum_j \delta\hat{\psi}_j^\dagger \delta\hat{\psi}_j^\dagger \delta\hat{\psi}_j \delta\hat{\psi}_j . \tag{3.21}$$

The Hamiltonian of localized atoms is

$$\hat{H}_{loc} = \sum_j \hat{H}_j . \tag{3.22}$$

where

$$\hat{H}_j = \frac{U}{2} \hat{\phi}_j^\dagger \hat{\phi}_j \left(\hat{\phi}_j^\dagger \hat{\phi}_j - 1 \right) + [\nu(n_0 + n_1)U - \mu] \hat{\phi}_j^\dagger \hat{\phi}_j . \tag{3.23}$$

3.3 Itinerant atoms

For the operators of delocalized atoms, we invoke the Fourier transformation

$$\delta\hat{\psi}_j = \frac{1}{\sqrt{N_L}} \sum_{\mathbf{k}} \hat{a}_{\mathbf{k}} e^{i\mathbf{k}\cdot\mathbf{r}_j} , \tag{3.24}$$

in which the summation is performed over the Brillouin zone and $\mathbf{r}_j$ is a lattice vector. For definiteness, we consider in what follows a cubic lattice with the lattice constant r, where

$$r^D = \frac{V}{N_L} = \frac{\nu}{\rho} \qquad \left(\rho \equiv \frac{N}{V} \right) . \tag{3.25}$$

with D being the spatial dimensionality.

For this choice the second-order term (3.19) transforms to

$$\hat{H}^{(2)} = \sum_{\mathbf{k}} \left[-2J \sum_\alpha \cos(k_\alpha r) + 2\nu n_0 U + \nu n_2 U - \mu_1 \right] \hat{a}_{\mathbf{k}}^\dagger \hat{a}_{\mathbf{k}} . \tag{3.26}$$

The third-order term (3.20) becomes

$$\hat{H}^{(3)} = \frac{U}{N_L} \sqrt{N_0} \sum_{\mathbf{k},\mathbf{p}} \left(\hat{a}_{\mathbf{k}}^\dagger \hat{a}_{\mathbf{p}} \hat{a}_{\mathbf{k}+\mathbf{p}} + \hat{a}_{\mathbf{k}+\mathbf{p}}^\dagger \hat{a}_{\mathbf{p}} \hat{a}_{\mathbf{k}} \right) . \tag{3.27}$$

And the fourth-order term (3.21) is

$$\hat{H}^{(4)} = \frac{U}{2N_L} \sum_{\mathbf{k},\mathbf{p},\mathbf{q}} \hat{a}_{\mathbf{k}}^\dagger \hat{a}_{\mathbf{p}}^\dagger \hat{a}_{\mathbf{k}+\mathbf{q}} \hat{a}_{\mathbf{p}-\mathbf{q}} . \tag{3.28}$$

The following consideration is in line with the general self-consistent approach to Bose systems with broken gauge symmetry, advanced in Refs. [29, 48], and employed in Refs. [27, 39, 122]. We use the definition (as in Chapter (1))

$$\omega_k \equiv -2J \sum_\alpha \cos(k_\alpha r) + \nu(1 + n_0 + n_1)U - \mu_1 \tag{3.29}$$

and

$$\Delta \equiv \nu(n_0 + \sigma)U, \tag{3.30}$$

where normal and anomalous averages are (as in Chapter 1)

$$\begin{aligned} n_1 &= \frac{1}{N}\sum_{\mathbf{k}} n_{\mathbf{k}} \qquad (n_{\mathbf{k}} \equiv \langle \hat{a}^\dagger_{\mathbf{k}} \hat{a}_{\mathbf{k}} \rangle), \\ \sigma &= \frac{1}{N}\sum_{\mathbf{k}} \sigma_{\mathbf{k}} \qquad (\sigma_{\mathbf{k}} \equiv \langle \hat{a}_{-\mathbf{k}} \hat{a}_{\mathbf{k}} \rangle). \end{aligned} \tag{3.31}$$

Employing the Hartree-Fock-Bogoliubov approximation yields

$$\hat{H}_{\rm del} = \hat{E}_{\rm HFB} + \sum_{\mathbf{k}} \omega_k \hat{a}^\dagger_{\mathbf{k}} \hat{a}_{\mathbf{k}} + \frac{1}{2}\sum_{\mathbf{k}} \left(\Delta \hat{a}^\dagger_{\mathbf{k}} \hat{a}^\dagger_{-\mathbf{k}} + \Delta^* \hat{a}_{-\mathbf{k}} \hat{a}_{\mathbf{k}} \right). \tag{3.32}$$

where the nonoperator term is

$$\hat{E}_{\rm HFB} \equiv \hat{H}^{(0)} - N\nu \left(2n_1^2 + \sigma^2 \right) \frac{U}{2}. \tag{3.33}$$

Diagonalizing this Hamiltonian with the help of the Bogoliubov transformation (1.23) yields the Hamiltonian

$$\hat{H}_{\rm del} = \hat{E}_{\rm B} + \sum_{\mathbf{k}} \mathcal{E}_k \hat{b}^\dagger_{\mathbf{k}} \hat{b}_{\mathbf{k}}, \tag{3.34}$$

with the nonoperator term

$$\hat{E}_{\rm B} = \hat{E}_{\rm HFB} + \frac{1}{2}\sum_{\mathbf{k}} (\mathcal{E}_k - \omega_k), \tag{3.35}$$

and the excitation spectrum is $\mathcal{E}_k = \sqrt{\omega_k^2 - \Delta^2}$.

In equilibrium, the equation of motion for condensate atoms [94] reduces to

$$\left\langle \frac{\partial \hat{H}}{\partial N_0} \right\rangle = 0. \tag{3.36}$$

which gives the condensate chemical potential

$$\mu_0 = -z_0 J + \nu U(n_0 + 2n_1 + \sigma). \tag{3.37}$$

The condition of condensate existence [94] requires gapless spectrum such that

$$\lim_{k \to 0} \mathcal{E}_k = 0 \qquad (\mathcal{E}_k \geq 0), \tag{3.38}$$

which is equivalent to the Hugenholtz-Pines relation [123] and yields

$$\mu_1 = -z_0 J + \nu U(1 + n_1 - \sigma). \tag{3.39}$$

Next, we introduce notation

$$\varepsilon_k \equiv 2J \sum_\alpha [1 - \cos(k_\alpha r)] = 4J \sum_\alpha \sin^2 \left(\frac{k_\alpha r}{2} \right). \tag{3.40}$$

The normal and anomalous averages (3.31) are given by the integrals

$$n_1 = \frac{1}{\rho} \int_{\mathcal{B}} n_k \frac{d^3k}{(2\pi)^3}, \qquad \sigma = \frac{1}{\rho} \int_{\mathcal{B}} \sigma_k \frac{d^3k}{(2\pi)^3}, \tag{3.41}$$

in which the integration is over the Brillouin zone and

$$n_k = \frac{\omega_k}{2\mathcal{E}_k} \coth \left(\frac{\mathcal{E}_k}{2T} \right) - \frac{1}{2}, \qquad \sigma_k = -\frac{\Delta}{2\mathcal{E}_k} \coth \left(\frac{\mathcal{E}_k}{2T} \right). \tag{3.42}$$

Equation (1.32) in the Chapter 1 yields the excitation spectrum $\mathcal{E}_k$ in the form

$$\mathcal{E}_k = \sqrt{\varepsilon_k (\varepsilon_k + 2\Delta)}. \tag{3.43}$$

3.4 Localized atoms

In the Hamiltonian of localized atoms (3.22), the site terms (3.23) can be represented as

$$\hat{H}_j = \frac{U}{2} \hat{N}_j^2 + \left[U \left(\nu n_0 + \nu n_1 - \frac{1}{2} \right) - \mu \right] \hat{N}_j, \tag{3.44}$$

with the density operator

$$\hat{N}_j \equiv \hat{\phi}_j^\dagger \hat{\phi}_j. \tag{3.45}$$

The average number of localized atoms per site is

$$\langle \hat{N}_j \rangle = \frac{\mathrm{Tr} \hat{N}_j e^{-\beta \hat{H}_j}}{\mathrm{Tr} e^{-\beta \hat{H}_j}}. \tag{3.46}$$

Since the eigenvalues of Hamiltonian (3.44) are

$$E_n = \frac{U}{2} n^2 + \left[U \left(\nu n_0 + \nu n_1 - \frac{1}{2} \right) - \mu \right] n, \tag{3.47}$$

where $n = 1, 2, \ldots$, the average number of localized atoms (3.46) is

$$\nu n_2 = \frac{\sum_{n=0}^{\infty} n e^{-\beta E_n}}{\sum_{n=0}^{\infty} e^{-\beta E_n}}. \tag{3.48}$$

At low temperature, such that $T \ll U$, the maximal contribution into the sums over n is given by the term with $n = n_{\mathrm{eff}}$, for which E_n is minimal, that is, when

$$\frac{\partial E_n}{\partial n} = 0, \qquad \frac{\partial^2 E_n}{\partial n^2} > 0. \tag{3.49}$$

The latter gives

$$n_{\rm eff} = \frac{1}{2} - \nu(n_0 + n_1) + \frac{\mu}{U}, \tag{3.50}$$

under condition $U > 0$. Thus, we obtain at $T \ll U$

$$\nu n_2 \simeq n_{\rm eff}. \tag{3.51}$$

Combining Eqs. (3.50) and (3.51) results at $T \ll U$ in:

$$\mu = \left(\nu - \frac{1}{2} \right) U. \tag{3.52}$$

According to Eq. (3.30), we have

$$\sigma + n_0 = \frac{\Delta}{\nu U}. \tag{3.53}$$

Using this in the chemical potentials (3.37) and (3.39) results in

$$\begin{aligned} \mu_0 &= -z_0 J + \Delta + 2\nu n_1 U, \\ \mu_1 &= -z_0 J - \Delta + \nu(1 + n_0 + n_1) U. \end{aligned} \tag{3.54}$$

Equating expressions (3.13) and (3.52) gives

$$\left(\nu - \frac{1}{2} \right) U = \frac{\mu_0 n_0 + \mu_1 n_1}{n_0 + n_1}. \tag{3.55}$$

From Eqs. (3.54) and (3.55), we find

$$\frac{n_0}{n_1} = \frac{(1 + 2\nu n_1)U - 2\Delta - 2z_0 J}{(2\nu - 6\nu n_1 - 1)U - 2\Delta + 2z_0 J}. \tag{3.56}$$

The latter, employing the relation

$$n_2 = 1 - n_0 - n_1. \tag{3.57}$$

results in the equation

$$n_2 = \frac{U - 2z_0 J + 2\nu U(4n_1 - 2n_1^2 - 1) + 2\Delta(1 - 2n_1)}{U - 2z_0 J + 2\nu U(3n_1 - 1) + 2\Delta}, \tag{3.58}$$

defining the fraction of localized atoms n_2.

3.5 Dimensionless equations

For numerical calculations, it is convenient to introduce the dimensionless interaction parameter

$$u \equiv \frac{U}{z_0 J} \tag{3.59}$$

and the dimensionless sound velocity is

$$c \equiv \sqrt{\frac{\Delta}{z_0 J}}. \tag{3.60}$$

Also, considering a cubic lattice, we use the dimensionless wave vector with the components

$$q_\alpha \equiv \frac{r}{\pi} k_\alpha \qquad (\alpha = 1, 2, \ldots, D). \tag{3.61}$$

Measuring all energy quantities in units of $z_0 J$, we have, instead of Eq. (3.29),

$$\omega_k = \varepsilon_k + c^2, \tag{3.62}$$

where

$$\varepsilon_k = \frac{4}{z_0} \sum_\alpha \sin^2 \left(\frac{\pi}{2} q_\alpha \right). \tag{3.63}$$

and the Bogoliubov spectrum (3.43) becomes

$$\mathcal{E}_k = \sqrt{\varepsilon_k (\varepsilon_k + 2c^2)}. \tag{3.64}$$

With the relation $\rho r^D = \nu$, Eqs. (3.41) are reduced to

$$\begin{aligned} n_1 &= \frac{1}{\nu} \int_0^1 \ldots \int_0^1 n_k dq_1 \ldots dq_D. \\ \sigma &= \frac{1}{\nu} \int_0^1 \ldots \int_0^1 \sigma_k dq_1 \ldots dq_D. \end{aligned} \tag{3.65}$$

where n_k and σ_k are given by Eq. (3.42). In particular, at zero temperature, we have

$$n_k = \frac{1}{2} \left(\frac{\omega_k}{\mathcal{E}_k} - 1 \right) \qquad \sigma_k = -\frac{c^2}{2\mathcal{E}_k}. \tag{3.66}$$

Equation (3.30) for the sound velocity becomes

$$c^2 = (n_0 + \sigma) \nu u. \tag{3.67}$$

And for Eq. (3.58), we find

$$n_2 = \frac{2 + (2\nu - 1)u - 4\nu n_1 (2 - n_1) u + 2c^2 (2n_1 - 1)}{2 + (2\nu - 1)u - 6\nu n_1 u - 2c^2}. \tag{3.68}$$

3.6 Numerical results and discussion

We accomplish numerical calculations for a three-dimensional cubic lattice ($D = 3$, $z_0 = 6$), with unity filing factor ($\nu = 1$), at zero temperature ($T = 0$). Explicitly, we solve numerically the system of equations

$$n_1 = \frac{1}{2} \int_0^1 \left(\frac{\omega_k}{\mathcal{E}_k} - 1 \right) dq_1 dq_2 dq_3. \tag{3.69}$$

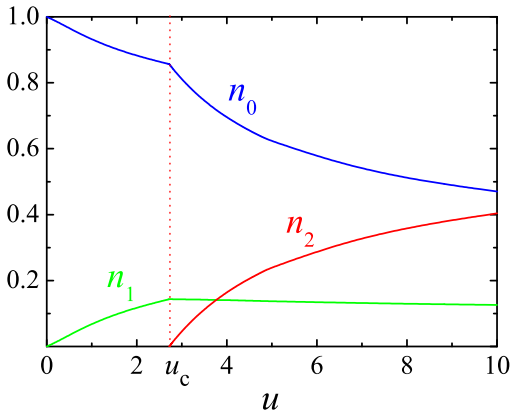

Figure 3.1: Atomic fractions, as functions of the dimensionless interaction parameter u, for the condensed atoms (blue line), uncondensed atoms (green line), localized atoms (red line), and $u_c = 2.75$.

$$\sigma = -\frac{c^2}{2}\int_0^1 \frac{1}{\mathcal{E}_k} dq_1 dq_2 dq_3 . \tag{3.70}$$

$$\omega_k = \varepsilon_k + c^2 . \qquad \mathcal{E}_k = \sqrt{\varepsilon_k(\varepsilon_k + 2c^2)} . \tag{3.71}$$

$$\varepsilon_k = \frac{2}{3}\sum_{\alpha=1}^{3} \sin^2\left(\frac{\pi}{2} q_\alpha\right) . \qquad k_\alpha \equiv \frac{\pi}{r} q_\alpha . \tag{3.72}$$

$$c^2 = (n_0 + \sigma)u . \qquad n_0 = 1 - n_1 - n_2 . \tag{3.73}$$

$$n_2 = \frac{2 + u - 4un_1(2 - n_1) + 2c^2(2n_1 - 1)}{2 + u - 6un_1 - 2c^2} . \tag{3.74}$$

The results for the fractions of condensed atoms, n_0, uncondensed atoms, n_1, and localized atoms, n_2, are shown in Fig. 3.1.

When the interaction parameter (3.59) is smaller than $u_c = 2.75$, there are no positive solutions for n_2, so that the sole possibility is $n_2 = 0$, which corresponds to the single-band Hubbard model. The mixture can exist only for $u > 2.75$ as marked in Fig. 3.1. This gives the lower boundary for the possible quasiequilibrium coexistence of itinerant Bose-condensed and localized atoms.

To conclude the Chapter: we analyzed conditions, under which a quasiequilibrium system of coexisting itinerant and localized Bose atoms could be created. The consideration is based on an effective two-band, or two-component, boson Hubbard model [94]. One component corresponds to itinerant atoms and is described by the self-consistent Hartree-Fock-Bogoliubov approximation [29, 48]. This approximation is known [29] to be well suited for superfluids. However, since it explicitly takes into account the global gauge symmetry breaking, it is not suitable for the Mott insulating state, where the gauge symmetry is not broken [124]. Therefore,

the localized atoms in the insulating state are characterized in our model as bound atoms without tunneling between the lattice sites. We find that the mixture of itinerant and localized atoms can be formed only when the on-site repulsion is sufficiently strong, such that $u > 2.75$.

It is interesting to mention that in the presented model the itinerant and localized atoms are not spatially separated. This distinguishes our case from that studied in Ref. [125], where superfluid droplets were spatially separated, being surrounded by normal, nonsuperfluid, phase.

Part III

COLLAPSE OF TWO-DIMENSIONAL SPIN-ORBIT COUPLED BOSE-EINSTEIN CONDENSATES

Chapter 4

Collapse of spin-orbit coupled Bose-Einstein condensates

A finite-size quasi two-dimensional Bose-Einstein condensate collapses if the attraction between atoms is sufficiently strong. Here we present a theory of collapse for condensates with the interatomic attraction and spin-orbit coupling. We consider two realizations of spin-orbit coupling: the axial Rashba coupling and balanced, effectively one-dimensional, Rashba-Dresselhaus one. In both cases spin-dependent "anomalous" velocity, proportional to the spin-orbit coupling strength, plays a crucial role. For the Rashba coupling, this velocity forms a centrifugal component in the density flux opposite to that arising due to the attraction between particles and prevents the collapse at a sufficiently strong coupling. For the balanced Rashba-Dresselhaus coupling, the spin-dependent velocity can spatially split the initial state in one dimension and form spin-projected wavepackets, reducing the total condensate density. Depending on the spin-orbit coupling strength, interatomic attraction, and the initial state, this splitting either prevents the collapse or modifies the collapse process. These results show that the collapse can be controlled by a spin-orbit coupling, thus, extending the domain of existence of condensates of attracting atoms.

4.1 Introduction

Understanding Bose-Einstein condensates of interacting atoms is one of the most interesting problems in condensed matter physics [126]. For uniform three dimensional systems repulsion between the bosons depletes the condensate, while attraction leads to the condensate instability seen as the appearance of Bogoliubov modes with imaginary frequencies. For the finite-size condensates this instability can be seen in their collapse [127–131]. The collapse, where the size of the state goes to zero after a finite time, strongly depends on the spatial dimension D and is possible only in the $D = 2$ and $D = 3$ condensates. The physics of the collapse is related to the fundamental problems of nonlinear optics and quantum mechanics [132], plasma instability [133], and polaron formation [134].

The main features of the collapse of a free, not restricted by an external potential, condensate, are determined by the interplay of its positive quantum kinetic and negative attraction energies dependent on the characteristic size of the condensate a. The kinetic energy is proportional to a^{-2} while the attraction contribution behaves as $-a^{-D}$. For $D = 3$ the dependence of the total energy on a is non monotonic and the collapse with $a \to 0$ occurs at any interaction strength since at small a the attraction dominates [135]. For $D = 2$ the interaction and kinetic energies scale as a^{-2} and the collapse occurs only at a strong enough attraction.

The BEC physics becomes much richer with synthetic gauge fields [136] and synthetic spin-orbit coupling (SOC) [137, 138]. For the latter, optically produced atomic pseudospin 1/2 is coupled to atomic momentum and to a synthetic magnetic field. The SOC can be produced in various forms, simulating the Rashba and the Dresselhaus symmetries [139, 140] known in solid state physics. This coupling opens a venue to the appearance of new phases in a variety of ultracold bosonic [21, 141–150] and fermionic [151–154] ensembles. The SOC plays crucial role in BEC physics in uniform three-dimensional gases with interparticle repulsion and makes condensation possible only at zero temperature [155], while at a finite temperature the thermal depletion of the condensate diverges [156]. For $D = 2$ the phases of the BEC of repelling bosons trapped in a harmonic potential were found in Ref. [157].

One of the advantages of cold atomic gases is the fact that due to a very large particle wavelength compared with the atomic radius, the interatomic interaction can be accurately described by a single parameter, the scattering length a_s, where positive (negative) a_s corresponds to repulsion (attraction) between the atoms. The attraction can be achieved by means of the Feshbach resonance [158] in a certain range of the system parameters. Here we study joint effect of the interatomic attraction and spin-orbit coupling on the spread and collapse of a quasi two-dimensional spin-orbit coupled BEC.

4.2 General formulation: Hamiltonian and the collapse process

We consider a pancake-shaped condensate of pseudospin 1/2 particles described by a two-component wave function $\Psi = \left[\psi^{\uparrow}(\mathbf{r}, t), \psi^{\downarrow}(\mathbf{r}, t)\right]^T$, where $\mathbf{r} \equiv (x, y)$, nor-

malized to the total number of particles $N \gg 1$. In the presence of the spin-orbit coupling, the evolution of the wavefunction is described by a system of coupled nonlinear partial differential equations in the Gross-Pitaevskii-Schrödinger form

$$i\hbar\frac{\partial\Psi}{\partial t} = \left[-\frac{\hbar^2}{2M}\Delta + \widehat{H}_{\rm so} + \frac{1}{2}\left(\mathbf{B}\cdot\widehat{\boldsymbol{\sigma}}\right) - g_2\left|\Psi\right|^2\right]\Psi. \tag{4.1}$$

Here M is the particle mass, $\widehat{H}_{\rm so}$ is the SOC Hamiltonian, $\mathbf{B}$ is the effective synthetic magnetic field, and $\widehat{\boldsymbol{\sigma}} = (\widehat{\sigma}_x, \widehat{\sigma}_y, \widehat{\sigma}_z)$ is the spin operator. The coupling constant in Eq. (4.1) is given by $g_2 = -4\pi\hbar^2 a_s/Ma_z$, which we assume for simplicity to be spin-independent, where a_z is the condensate extension along the z-axis, and a_s is negative [127, 129, 130]. Below we consider two strongly different forms of $\widehat{H}_{\rm so}$: the Rashba coupling with the spectrum axially symmetric in the momentum space and the balanced, essentially, one-dimensional Rashba-Dresselhaus coupling.

Without loss of generality, we consider an initial state prepared in a parabolic potential at zero temperature as:

$$\Psi(\mathbf{r}, t=0) \equiv A(0)\exp\left[-\frac{r^2}{2a^2(0)}\right]\boldsymbol{\psi}(0), \tag{4.2}$$

where $\boldsymbol{\psi}(0)$ is the initial spinor, $A(0) = \sqrt{N/\pi}/a(0)$, and $a(0)$ is the initial width. At $t = 0$, the confining potential is switched off [126] and the spin-orbit coupling and the attraction between the atoms are switched on. The subsequent dynamics is, thus, a response of the system to the instantaneous change in the potential, interaction, and spin-orbit coupling.

In what follows we use the units $\hbar \equiv M \equiv 1$ and the dimensionless interaction $\widetilde{g}_2 \equiv -4\pi a_s/a_z$. The unit of length ℓ can be chosen arbitrarily, and the corresponding unit of time is ℓ^2.

We address first the collapse without spin-dependent effects. Here the energy of the system is

$$E = -\frac{1}{2}\int\left[\Psi^\dagger\Delta\Psi + \widetilde{g}_2\left|\Psi\right|^4\right]dxdy, \tag{4.3}$$

and the evolution can be described by a variational approach based on Gaussian ansatz [129]

$$\Psi(\mathbf{r}, t) = A(t)\exp\left[-\frac{r^2}{2a_{\rm v}^2(t)}\left(1 + ib_{\rm v}(t)\right)\right]\boldsymbol{\psi}(0), \tag{4.4}$$

where the variational parameters $b_{\rm v}(t)$ and $a_{\rm v}(t)$ are the chirp and the packet width, respectively. The equation of motion for $a_{\rm v}$ becomes $\ddot{a}_{\rm v} = -\Lambda/a_{\rm v}^3$, where $\Lambda = \left(\widetilde{g}_2 N - \lambda_{\rm v}\right)/2$. The collapse occurs if $\widetilde{g}_2 N$ exceeds the variational threshold value [1] $\lambda_{\rm v} = 2\pi$. The solution of this equation is

$$a_{\rm v}(t) = a(0)\sqrt{1 - \frac{\Lambda t^2}{a^4(0)}}. \tag{4.5}$$

[1] More precisely, the critical interatomic attraction is slightly smaller [133], that is $\lambda_{\rm ex} = 1.862\pi$. We will return to this difference between the exact and variational ($\lambda_{\rm v}$) threshold values when considering near-the-threshold collapse.

The timescale of the evolution is the collapse time $T_c \equiv a^2(0)/\sqrt{\Lambda}$, and the characteristic collapse velocity is $v_c \equiv a(0)/T_c = \sqrt{\Lambda}/a(0)$.

The key point in the understanding of the role of the spin-orbit coupling in the collapse process is the modified velocity

$$\mathbf{v} = \mathbf{k} + \boldsymbol{\nabla}_{\mathbf{k}} \widehat{H}_{\rm so}, \tag{4.6}$$

with $\mathbf{k} = -i\partial/\partial\mathbf{r}$, including the anomalous velocity [159] term $\boldsymbol{\nabla}_{\mathbf{k}}\widehat{H}_{\rm so}$ (here $\boldsymbol{\nabla}_{\mathbf{k}} \equiv \partial/\partial\mathbf{k}$) directly related to the particle spin. The evolution of the probability density $\rho = \Psi^\dagger\Psi$ is given by the continuity equation

$$\frac{\partial\rho}{\partial t} + \boldsymbol{\nabla}\cdot\mathbf{J}(\mathbf{r},t) = 0, \tag{4.7}$$

with the components of the flux density

$$\mathbf{J}(\mathbf{r},t) = \frac{i}{2}\left[\Psi\boldsymbol{\nabla}\Psi^\dagger - \Psi^\dagger\boldsymbol{\nabla}\Psi\right] + \Psi^\dagger\left[\boldsymbol{\nabla}_{\mathbf{k}}\widehat{H}_{\rm so}\right]\Psi. \tag{4.8}$$

The spin components of the condensate are given by quantum mechanical expectation values

$$\langle\widehat{\sigma}_i(t)\rangle = \frac{1}{N}\int \Psi^\dagger\widehat{\sigma}_i\Psi dxdy. \tag{4.9}$$

4.3 Rashba spin-orbit coupling

4.3.1 Strong interaction collapse

As the first form of spin-orbit interaction we consider the Rashba coupling

$$\widehat{H}_{\rm so} \equiv \widehat{H}_R = \alpha\left(k_x\widehat{\sigma}_y - k_y\widehat{\sigma}_x\right), \tag{4.10}$$

with the coupling constant α and $\mathbf{k} \equiv (k_x, k_y)$. The corresponding spin-dependent terms in the velocity operators in Eq. (4.6) become

$$\frac{\partial\widehat{H}_R}{\partial k_x} = \alpha\widehat{\sigma}_y, \quad \frac{\partial\widehat{H}_R}{\partial k_y} = -\alpha\widehat{\sigma}_x. \tag{4.11}$$

The spatial scale of the SOC effects is described by the characteristic distance the particle has to move to flip the spin, $L_{\rm so} = 1/\alpha$. The corresponding spin rotation angle at the particle displacement L is of the order of $L/L_{\rm so}$. At the initial stage of the BEC evolution $t \ll T_c$ we obtain from Eq. (4.1) for $\Psi(\mathbf{r}, t=0)$ in Eq. (4.2) with $\boldsymbol{\psi}(0) = [1,0]^T$,

$$\frac{\partial}{\partial t}\psi^\downarrow(\mathbf{r}, t\to 0) = i\frac{\sqrt{N}}{\sqrt{\pi}a^3(0)}\frac{x+iy}{L_{\rm so}}\exp\left[-\frac{r^2}{2a^2(0)}\right]. \tag{4.12}$$

As a result, the $\psi^\downarrow(\mathbf{r},t)$ component begins to grow at distances $r \sim a(0)$ with a rate proportional to α at the funnel form as presented in Fig. 4.1. At a sufficiently large α this growth can eventually lead to the collapse prevention.

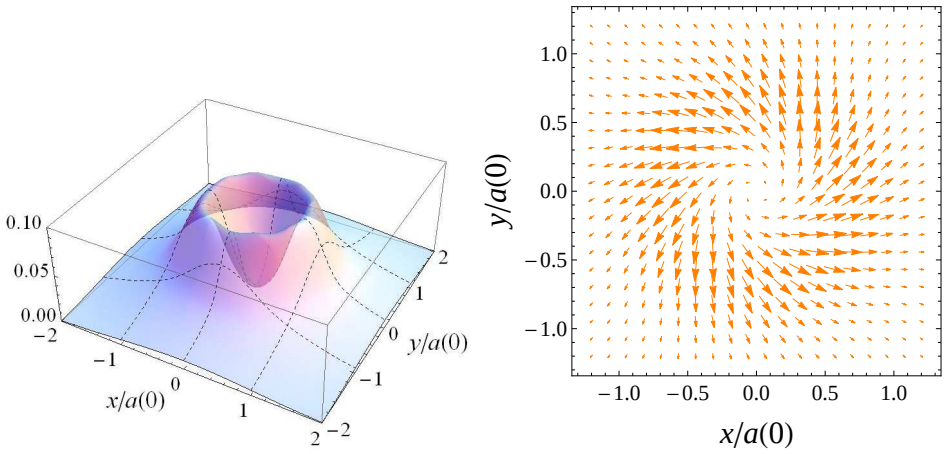

Figure 4.1: (left) Spinor component density $|\psi^{\downarrow}(x,y,t)|^2 a^2(0)$ and (right) flux of the condensate for parameters $\widetilde{g}_2 N = 16\pi$ and $\alpha = 0.84 v_c$ at the time $t = 0.2a^2(0)$. Since here $\alpha > \alpha_{\rm cr} = 0.7 v_c$ this is the no-collapse regime.

At $t > 0$, a spatially nonuniform spin evolution begins. Since the spin precession angle at the displacement of $a(0)$ is of the order of $a(0)/L_{\rm so}$, starting from the fully polarized $\boldsymbol{\psi}(0) = [1,0]^T$ state, the atoms acquire the anomalous velocity of the order of $a(0)/L_{\rm so} \times \alpha \sim \alpha^2 a(0)$ for the weak SOC $a(0) \ll L_{\rm so}$, or of the order of α otherwise. The criterion of a large spin rotation in the collapse is $a(0) > L_{\rm so}$, that is $\alpha > 1/a(0)$, while the condition of a sufficiently large developed anomalous velocity is $\alpha > v_c$, that is

$$\alpha > \frac{\sqrt{\Lambda}}{a(0)}. \tag{4.13}$$

If the latter inequality is satisfied, the centrifugal component in the flow caused by the SOC, [2] which is demonstrated in Fig. 4.1, can prevent the collapse, as we explain in detail below. The condition of a weak effect of magnetic field on the collapse can be formulated as smallness of spin precession angle due to the Zeeman splitting compared to the precession angle due to the spin-orbit coupling, that is $T_c B \ll \min\{a(0)/L_{\rm so}, 1\}$. We will assume this condition and neglect the effects of the Zeeman splitting.

We begin the analysis of the joint effect of the SOC and the interatomic attraction with numerical results obtained by direct integration of Eq.(4.1) for a strong interaction, $\widetilde{g}_2 N \gg 1$, where the effect is clearly seen, taking the initial spin state $\boldsymbol{\psi}(0) = [1,0]^T$. Figure 4.2 shows the time-dependent width of the packet defined

[2] This effect, being an intrinsic property of the spin-orbit coupled BEC, is qualitatively different from the centrifugal flux formed by the angular momentum of a rotating condensate. See [160] for a review on the latter systems.

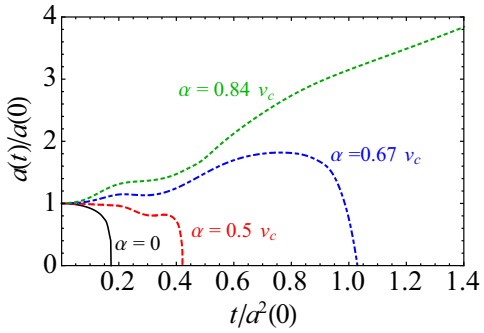

Figure 4.2: Time dependence of the condensate width for $\widetilde{g}_2 N = 16\pi$ and the values of α marked near the lines. The green short-dashed line corresponds to the absence of collapse.

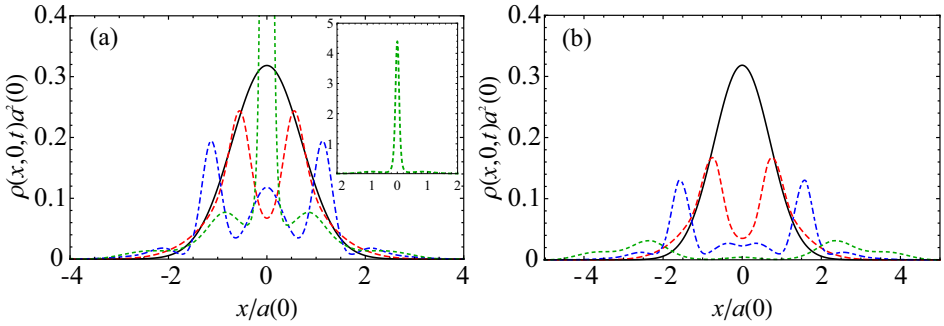

Figure 4.3: Density profile $\rho(x, y, t)$ for $\widetilde{g}_2 N = 16\pi$. Black solid line is for $t = 0$, red dashed line is for $t = 0.2a^2(0)$, blue dot-dashed line is for $t = 0.4a^2(0)$, and green dotted line is for $t = a^2(0)$. (a) $\alpha = 0.67 v_c$, and the dotted green line shown in detail in the inset, clearly demonstrates the collapse. (b) $\alpha = 0.84 v_c$, the condensate is robust against attraction and can spread without collapsing.

as

$$a(t) \equiv \frac{N}{\sqrt{2\pi}} \left[\int |\Psi|^4 \, dxdy \right]^{-1/2}, \tag{4.14}$$

where Ψ is obtained by a direct solution of Eq. (4.1) representative values of α. The solid line in Fig. 4.2 corresponds to the collapse at $\alpha = 0$ where in the vicinity of T_c, the numerically calculated using Eqs. (4.1) and (4.14), width $a(t)$ is accurately described by variational Eq. (4.5) with $a(t) \sim (T_c - t)^{1/2}$.

When spin-orbit coupling is included, the following features may be seen.

(i) At short time $t \ll T_c$, the attraction-induced velocity develops linearly with t, while the anomalous velocity increases as t^2. As a result, the $a(t)$-dependences for all values of α are the same at small t.

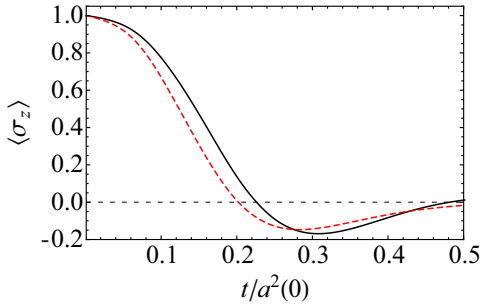

Figure 4.4: Time dependence of the total condensate spin component. Here $\widetilde{g}_2 N = 16\pi$, black solid line is for $\alpha = 0.67 v_c < \alpha_{\rm cr}$ (collapse regime), and red dashed line is for $\alpha = 0.84 v_c$ (no-collapse regime).

(ii) The packet width $a(t)$ increases with time, reaches a plateau, and then decreases to zero. Thus, with the increase in α, the collapse still can occur, albeit taking a longer actual time $t_c > T_c$.

(iii) Increasing further, α reaches a critical value $\alpha_{\rm cr} \approx 0.7 v_c$ such that at $\alpha > \alpha_{\rm cr}$ the anomalous velocity is large enough to prevent the collapse. The dependence of t_c on the SOC strength can be described as $t_c \sim (\alpha_{\rm cr} - \alpha)^{-1}$.

To get an insight of the effects of SOC on the collapse, we depict the density profiles in Fig. 4.3. At a large α the density forms a double peak with the maxima positions separating with time as a result of the centrifugal component in the flux. The resulting two-dimensional density distribution is given by a ring of radius $R(t)$ and width $w(t)$ with $a(t) \sim \sqrt{R(t)w(t)}$, responsible for the broad plateaus in $a(t)/a(0)$ seen in Fig. 4.2 at subcritical spin-orbit coupling. At $R(t) \gg a(t)$ the interatomic interaction energy tends to zero as $-1/R(t)w(t)$, and the conserved total energy becomes the sum of the kinetic and SOC terms. At $\alpha < \alpha_{\rm cr}$, (see Fig. 4.3(a)) the attraction is still strong enough to reverse the splitting and to restore the collapse. At $\alpha > \alpha_{\rm cr}$, (see Fig. 4.3(b)) the anomalous velocity takes over, the splitting continues, and the collapse does not occur [3]. This process is naturally accompanied by evolution of the condensate flux and spin presented in the Fig. 4.4.

4.3.2 Near-the-threshold collapse

Now we address a near-the-threshold collapse, which takes a long time, and where the difference between the variational $\widetilde{g}_2 N = 2\pi$ and the exact $\widetilde{g}_2 N = 1.862\pi$

[3]The density can decrease to zero with infinite $R(t \to \infty)$ only in the absence of a strong confinement. If the confinement potential $\omega_0^2 \left(x^2 + y^2\right)/2$, where ω_0 is the corresponding frequency, is taken into account, the energy conservation limits the value of $R(t)$ and naturally increases the critical value of SOC. However, as our simulations show, in the case of a strong spin-orbit coupling, even if the density returns to the vicinity of the origin, where the confinement potential is weak, the centrifugal flux takes over and the condensate begins to spread again rather than to collapse.

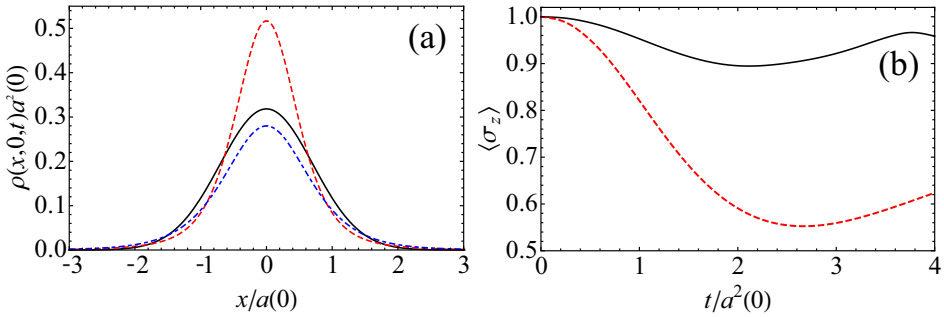

Figure 4.5: (left) Density profile of the condensate for $\alpha = 0.39(2\pi - \lambda_{\rm ex})^{1/4}$ (no-collapse regime) and different times: black solid line is for $t = 0$, red dashed line is for $t = a^2(0)$, and blue dot-dashed line is for $t = 4.4a^2(0)$. (right) Time dependence of the total condensate spin component, black solid line is for $\alpha = 0.19(2\pi - \lambda_{\rm ex})^{1/4}$ (collapse regime) and red dashed line is for $\alpha = 0.39(2\pi - \lambda_{\rm ex})^{1/4}$ (no-collapse regime). Here $\widetilde{g}_2 N = 2\pi$ is slightly above the critical value.

threshold couplings becomes important. We take $\widetilde{g}_2 N = 2\pi$, where in the absence of spin-related effects, the total energy in Eq. (4.3) of a Gaussian state is zero. In this case the critical spin-orbit coupling $\alpha_{\rm cr}$ sufficient to destroy the collapse by the anomalous velocity is determined by condition $\alpha_{\rm cr}^2 \sim v_c/a(0)$ and can be estimated as $(\widetilde{g}_2 N - \lambda_{\rm ex})^{1/4}$. The numerically obtained critical value is $\alpha_{\rm cr} \approx 0.38(2\pi - \lambda_{\rm ex})^{1/4}$. Figure 4.5(a) shows that for α slightly larger than the critical value, the condensate first narrows and then broadens. The peak structure of Fig. 4.3 is not formed here, and the collapse disappears due to the broadening rather than due to the splitting. Although the change in the spin component shown in Fig. 4.5(b) is moderate compared to that presented in Fig. 4.4, as expected for relatively small values of α, the collapse does not occur here.

4.4 Balanced Rashba and Dresselhaus couplings

In this subsection we consider a one-dimensional coupling

$$\widehat{H}_{\rm so} \equiv \widehat{H}_{RD} = \alpha k_x \widehat{\sigma}_z, \tag{4.15}$$

which is equivalent to the balanced Rashba and Dresselhaus contributions and can be gauged out by an x-dependent spin rotation [161]

$$\mathbf{U}(x) = \exp\left[i\widehat{\sigma}_z x/L_{\rm so}\right]. \tag{4.16}$$

For simplicity we consider the initial state corresponding to the spin oriented along the x-axis with $\boldsymbol{\psi}(0) = [1,1]^T/\sqrt{2}$. Due to the anomalous velocity $\partial\widehat{H}_{RD}/\partial k_x = \alpha\widehat{\sigma}_z$ (cf. Eq. (4.11)), the initial state splits into two spin-polarized wavepackets moving in the absence of interactions with velocities $\pm\alpha$. In the presence of

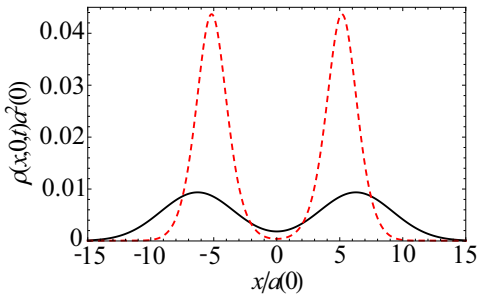

Figure 4.6: Density of the condensate and its profile for balanced Rashba-Dresselhaus coupling, $\alpha = 1.25v_c$ and $t = 4a^2(0)$ in the no-collapse regime. Lines correspond to $g = 0$ (solid line) and $\widetilde{g}_{2D}N = 3\pi$ (dashed line).

interaction for initial time the separation of the condensate should overcome the attraction between atoms, while the condensate completely separates in two parts, and each part expands slower in the no-collapse regime. These effects can be seen in Fig. 4.6. As a result, the effective interaction decreases, and the collapse can be prohibited by this decrease. This happens, however, only at certain conditions, which we establish here. For qualitative variational analysis we use the ansatz

$$\psi^{\uparrow,\downarrow}(\mathbf{r}_{\mp},t) = \widetilde{A}(t)\exp\left[-\frac{r_{\mp}^2}{2\widetilde{a}_{\rm v}^2(t)}\left(1+i\widetilde{b}_{\rm v}(t)\right) \mp i\widetilde{c}_{\rm v}(t)x\right], \tag{4.17}$$

where the upper (lower) sign corresponds to spin up (down) and position $\mathbf{r}_{\mp} \equiv (x \mp \widetilde{d}_{\rm v}(t), y)$, and in addition to the variational chirp $\widetilde{b}_{\rm v}(t)$ and width $\widetilde{a}_{\rm v}(t)$, we introduced the variational momentum $\widetilde{c}_{\rm v}(t)$. From this ansatz we obtain, using an approach similar to that of Ref. [129], equations of motion for $\widetilde{d}_{\rm v}$ and $\widetilde{a}_{\rm v}$:

$$\begin{aligned}
\ddot{\widetilde{d}}_{\rm v} &= -\frac{\widetilde{g}_2 N}{\pi}\frac{\widetilde{d}_{\rm v}}{\widetilde{a}_{\rm v}^4}\exp\left(-\frac{2\widetilde{d}_{\rm v}^2}{\widetilde{a}_{\rm v}^2}\right), \\
\ddot{\widetilde{a}}_{\rm v} &= \frac{1}{\widetilde{a}_{\rm v}^3}\left[\pi - \frac{\widetilde{g}_2 N}{4}\left[1+\left(1-\frac{2\widetilde{d}_{\rm v}^2}{\widetilde{a}_{\rm v}^2}\right)\exp\left(-\frac{2\widetilde{d}_{\rm v}^2}{\widetilde{a}_{\rm v}^2}\right)\right]\right],
\end{aligned} \tag{4.18}$$

for given $\widetilde{a}_v(0) = a(0)$ and other initial conditions

$$\widetilde{d}_{\rm v}(0) = 0, \quad \dot{\widetilde{d}}_{\rm v}(0) = \alpha, \quad \dot{\widetilde{a}}_{\rm v}(0) = 0, \tag{4.19}$$

where $\dot{\widetilde{d}}_{\rm v}(0)$ is due to the anomalous velocity term leading to the spin-dependent splitting. These equations show that the collapse disappears if the coupling is strong enough to sufficiently separate the spin components, that is at a certain time $\ddot{\widetilde{a}}_{\rm v}$ changes sign from negative to positive.

Qualitative conditions of the collapse in the presence of spin-orbit coupling in Eq. (4.15), which can be found from Eq. (4.18), are as follows. If $\widetilde{g}_2 N > 4\pi$, the

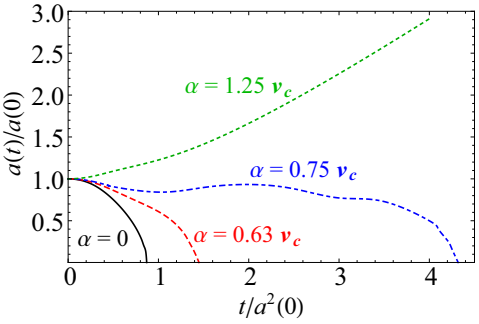

Figure 4.7: Time dependence of the condensate width for $\widetilde{g}_2 N = 3\pi$ in the presence of balanced Rashba-Dresselhaus SOC and different values of α as marked near the lines.

collapse always occurs since even if the spin states are well-separated, each of them still has the sufficient for collapse number of atoms. Depending on the interatomic interaction and SOC, one can either obtain the collapse at the origin, producing a spin non-polarized condensate, or two spatially symmetric ones producing z-axis polarized condensates. If $\widetilde{g}_2 N < 4\pi$, the collapse occurrence depends on the SOC strength.

At a sufficiently strong SOC, the spin splitting of the initial state and possible collapse happen on different time scales. The splitting occurs fast, on the timescale of $a(0)/\alpha$, and the interatomic attraction starts to play a role after the splitting. The condition of time scale separation, which allows one to treat the splitting and the collapse independently, is formulated as $a(0) < T_c\alpha$ or, in other words, as $\alpha > \sqrt{\Lambda}/a(0)$. This looks similar to the above condition (4.13) for the critical Rashba coupling. However, these conditions are qualitatively different. For the Rashba coupling, the density decreases to zero and the collapse disappears completely at any SOC stronger than the critical one. For the balanced Rashba-Dresselhaus coupling the maximum density decreases at most by a factor of two, and, therefore, the collapse can occur even at a very strong SOC, when spin-up and spin-down states are already well-separated in space.

Figure 4.7 shows the time dependence of the packet width in Eq. (4.14) obtained by solution of Eq. (4.1) with spin-orbit coupling Hamiltonian (4.15) for $\widetilde{g}_2 N = 3\pi$. The behavior at small $t \ll T_c$ here depends on α since the peaks in the spin-projected densities split by $2\alpha t$ due to the anomalous velocity. The numerically obtained critical value of α here is approximately $0.83 v_c$ and $a(t) \sim (t_c - t)$ shows a linear rather than a square-root behavior near the collapse time.

4.5 Relation to experiment and discussion

To make connections to possible BEC experiments, we return to the physical units and estimate the constant $\widetilde{g}_2$ as 0.05 for $-a_s \sim 100 a_B \sim 5 \times 10^{-3}$ μm and $a_z \sim 1$

μm. The condition $\widetilde{g}_2 N > 2\pi$ can be satisfied already for ensembles with $N \sim 100$ particles. The velocity of the collapse is $v_c \sim \hbar\sqrt{\widetilde{g}_2 N}/Ma(0)$. At $a(0) \sim 10$ μm and $N \sim 10^3$ this estimate yields $v_c \sim 0.03$ cm/s and the corresponding time scale $T_c = a(0)/v_c \sim 0.3$ s. Such a small value of v_c demonstrates that even a relatively weak experimentally achievable coupling [162] can prevent the BEC from collapsing. At these conditions, the characteristic distance between the particles $\left(a^2(0)a_z/N\right)^{1/3} \sim 0.5$ μm is much larger than $-4\pi a_s \leq 0.1$ μm, still preventing a strong depletion of the condensate.

To conclude this Chapter: we have demonstrated that the anomalous spin-dependent velocity determined by the spin-orbit coupling strength can prevent collapse of a nonuniform quasi two-dimensional BEC. For the Rashba coupling with the spectrum axially symmetric in the momentum space, this velocity leads to a centrifugal component in the two-dimensional density flux. As a result, spin-orbit coupling can prevent collapse of the two-dimensional BEC if this flux is sufficiently strong to overcome the effect of interatomic attraction. In this case, the attraction between the bosons cannot squeeze the initial wavepacket and force it to collapse. In the case of effectively one-dimensional balanced Rashba-Dresselhaus couplings, the anomalous velocity splits the initial state into spin-polarized wave packets, decreases the condensate density and, thus, can prevent the collapse. These results show that one can gain a control over the BEC collapse process by using the experimentally available synthetic spin-orbit coupling fields and, thus, extend the experimental abilities to study various nontrivial dynamical regimes in Bose-Einstein condensates of attracting particles.

Part IV

ONE-DIMENSIONAL SPIN-ORBIT COUPLED BOSE-EINSTEIN CONDENSATES

Chapter 5

Interference of spin-orbit coupled Bose-Einstein condensates

Interference of atomic Bose-Einstein condensates, observed in free expansion experiments, is a basic characteristic of their quantum nature. In this Chapter we theoretically describe interference of two noninteracting spin-orbit coupled Bose-Einstein condensates moving with different velocities in an external synthetic magnetic field. We demonstrate that the spin-orbit coupling and the magnetic field strongly influence the interference pattern determined by the angle between the spins of the condensates, as can be seen in time-of-flight experiments. In addition, we show that a quantum backflow, being a subtle feature of the interference, is, nevertheless, robust against the spin-orbit coupling and applied synthetic magnetic field.

5.1 Introduction

Interference of matter waves is one of the most interesting effects in quantum physics. The interference of two freely expanding Bose-Einstein condensates is a clear manifestation of quantumness in macroscopic systems [163–165]. It can be observed by preparing two condensates in spatially separated harmonic traps, that are released afterwards. Then, the condensates can expand freely and eventually overlap, producing an interference pattern.

In this Chapter we consider the time-of-flight control of interference of two one-dimensional condensates producing their entangled state, which might be required for quantum information purposes, by balanced Rashba-Dresselhaus spin-orbit coupling and synthetic magnetic field, as shown in Fig.5.1. The condensates, that move freely in a one-dimensional waveguide realized by means of tight confinement in the transverse directions, give rise to an interference pattern that strongly depends on the relative orientation of their pseudospins. We will study the role of the synthetic magnetic field on the interference and show that it can be fully controlled by changing the synthetic Zeeman coupling. In addition, we will show that the quantum backflow [166–173], being a subtle effect of the interference, is rather robust against the effects of mutual spin orientation.

5.2 Interference of two condensates with spin-orbit coupling

We begin with reminding a well-known picture of the motion of a free one-dimensional wavepacket in the presence of a balanced Rashba-Dresselhaus spin-orbit coupling with the Hamiltonian

$$\widehat{H} = \frac{\widehat{p}^2}{2M} + \frac{\alpha}{\hbar}\widehat{p}\widehat{\sigma}_z, \tag{5.1}$$

where $\widehat{\sigma}_z$ is the corresponding Pauli matrix, $\widehat{p}$ is the momentum operator, M is the particle mass, and α is the spin-orbit coupling constant. The solution of the Schrödinger equation

$$i\hbar\frac{\partial\Psi}{\partial t} = \widehat{H}\Psi, \qquad \Psi \equiv \Psi(x,t) \equiv \begin{bmatrix} \psi^{\uparrow}(x,t) \\ \psi^{\downarrow}(x,t) \end{bmatrix} \tag{5.2}$$

can be presented as

$$\Psi(x,t) = \int \exp\left(-\frac{i}{\hbar}\widehat{H}t + \frac{i}{\hbar}px\right)\mathbf{G}(p)\frac{dp}{2\pi\hbar}, \tag{5.3}$$

where $\mathbf{G}(p) = g(p)\boldsymbol{S}(0)$, $g\,(p)$ is wave function in the momentum space, and $\boldsymbol{S}(0) = (\beta_1(0),\ \beta_2(0))^T$ is the initial spinor normalized with $\beta_1^2(0)+\beta_2^2(0) = 1$. We assume without loss of generality that $\beta_1(0)$ and $\beta_2(0)$ are real. The spinor components

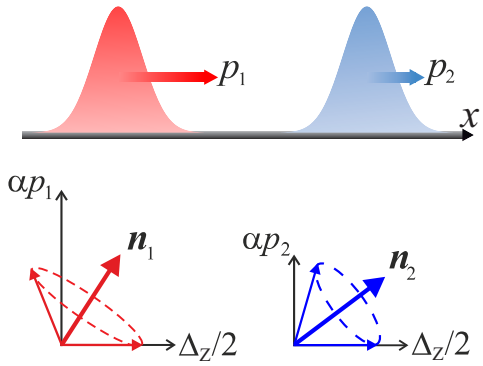

Figure 5.1: Two condensates with mean momenta per particle p_1, p_2 and spin-orbit coupling constant α and spins precessing in a synthetic magnetic field characterized by Zeeman splitting Δ_Z. Dashed ellipses show the time-dependent spins of condensates, and vectors $\mathbf{n}_1$ and $\mathbf{n}_2$ mark corresponding precession axes.

in (5.3) are:

$$\begin{aligned}\psi^{\uparrow}(x,t) &= \int \beta_1(0)g(p)\exp\left[-\frac{i}{\hbar}\frac{p^2t}{2M}+\frac{ipx_-}{\hbar}\right]\frac{dp}{2\pi\hbar},\\ \psi^{\downarrow}(x,t) &= \int \beta_2(0)g(p)\exp\left[-\frac{i}{\hbar}\frac{p^2t}{2M}+\frac{ipx_+}{\hbar}\right]\frac{dp}{2\pi\hbar},\end{aligned} \tag{5.4}$$

where $x_\pm \equiv x \pm \alpha t/\hbar$. Below, for definiteness, we assume Gaussian $g(p)$, produced by an initial state in a harmonic trap, as described in Ref. [173]. This function can be obtained as:

$$\begin{aligned}g\left(p\right) &= \int \psi(x,0)\exp(-ipx/\hbar)dx,\\ \psi(x,0) &= \frac{1}{(\pi w^2(0))^{1/4}}\exp\left[-\frac{(x-x_{\text{in}})^2}{2w^2(0)}+i\frac{x\langle p\rangle}{\hbar}\right],\end{aligned} \tag{5.5}$$

where $\langle p\rangle$ is the mean momentum, $w(0)$ is the initial width, and x_{in} is the initial position. As a result, (5.5) becomes

$$g(p) = (4\pi w^2(0))^{1/4}\exp\left[-\frac{w^2(0)(p-\langle p\rangle)^2}{2\hbar^2}-\frac{ipx_{\text{in}}}{\hbar}\right]. \tag{5.6}$$

The expectation values of the packet width and velocity at time t obtained by Eq. (5.4) are

$$\langle w(t)\rangle = \left[w^2(0)\left(1+\frac{\hbar^2t^2}{w^4(0)M^2}\right)+8\frac{\alpha^2t^2}{\hbar^2}\left(\beta_1(0)\beta_2(0)\right)^2\right]^{1/2}, \tag{5.7}$$

$$\langle v\rangle \equiv \frac{i}{\hbar}\langle[\widehat{H},\widehat{x}]\rangle = \frac{\langle p\rangle}{M} + \frac{\alpha}{\hbar}\langle\widehat{\sigma}_z(0)\rangle\,. \tag{5.8}$$

Here $\langle\widehat{\sigma}_z(0)\rangle = \boldsymbol{S}^\dagger(0)\widehat{\sigma}_z\boldsymbol{S}(0) = \beta_1^2(0) - \beta_2^2(0)$. It follows from (5.7) and (5.8) that the spin-orbit coupling modifies the width of the packet and velocity.

From Eq. (5.8) follows that, the current density $J(x,t)$ is given by (as in Eq. (4.8)):

$$J(x,t) = \frac{i\hbar}{2M}\left[\frac{\partial\Psi^\dagger}{\partial x}\Psi - \Psi^\dagger\frac{\partial\Psi}{\partial x}\right] + \frac{\alpha}{\hbar}\Psi^\dagger\widehat{\sigma}_z\Psi, \tag{5.9}$$

The experimentally measured density $\rho(x,t) = \Psi^\dagger(x,t)\Psi(x,t)$ is related to $J(x,t)$ by the continuity equation (4.7). For the weak coupling considered below we neglected the α - related terms in Eqs.(5.7)-(5.9).

For a packet narrow in the momentum space with $\langle p\rangle w(0) \gg \hbar$, one can neglect momentum distribution and present the wavefunction (5.3) as a product $\Psi(x,t) = \psi(x,t)\boldsymbol{S}(t)$, where $\psi(x,t)$ is the time and coordinate dependence in the absence of spin-orbit coupling. The spin state of a packet is given by:

$$\boldsymbol{S}(t) = \exp\left(-i\widehat{H}_{\rm so}t/\hbar\right)\boldsymbol{S}(0), \tag{5.10}$$

where $\widehat{H}_{\rm so} = \alpha\langle p\rangle\widehat{\sigma}_z/\hbar$ is the mean value of spin contribution to the Hamiltonian (5.1), and $\Omega = 2\alpha\langle p\rangle/\hbar^2$ is the mean spin precession rate. We apply Eq.(5.10) below for a qualitative analysis of the interference.

A comment on the applied approach is in order here. Instead of using direct calculation in Eqs. (5.2)-(5.4) and (5.10), One can produce coordinate-dependent spin rotation $\exp[ix\widehat{\sigma}_z/L_{\rm so}]$ as in Eq. (4.16), and then make the inverse transformation to obtain the physical result [161,174–176], same as in the above approach. However, in the presence of a Zeeman field, which is our interest, gauging out the spin-orbit coupling leads to a coordinate-dependent effective magnetic field, difficult to treat beyond the perturbation theory [174]. For this reasons we use the direct calculation rather than the spin rotation approach.

To see the effect of the spin-orbit coupling on interference of condensates, we take the initial wave function in the form where the coherence can be achieved, e.g. by technique proposed in [163]:

$$\mathbf{G}(p) = A_1 g_1(p)\boldsymbol{S}_1(0) + A_2 g_2(p)\boldsymbol{S}_2(0). \tag{5.11}$$

Here $\boldsymbol{S}_j(0) = (\beta_{j1}(0), \beta_{j2}(0))^T$ is the corresponding spinor, the amplitudes A_1 and A_2 are normalized as $A_1^2 + A_2^2 = 1$, and the Gaussian $g_j(p)$ is defined by (5.6), where $j = 1, 2$ labels the condensate. The average velocities of the packets v_j are determined by (5.8) for the corresponding momentum p_j and spin state, and from now on we omit $\langle\ldots\rangle$ in the notation of averages. Using (5.3) and (5.11) we obtain the exact evolution of two initial wave packets with spin-orbit coupling.

For a qualitative understanding we use a model of two independent condensates moving with different momenta. Take first as an illustration a system with wave function $\Psi(x,t)$ presented as a sum of two terms:

$$\Psi(x,t) = \Psi_1(x,t) + \Psi_2(x,t), \tag{5.12}$$

where

$$\Psi_j(x,t) = \psi_j(x,t)\boldsymbol{S}_j(t). \tag{5.13}$$

The current density (5.9) for the wave function (5.12) is defined by:

$$\begin{aligned} J(x,t) = \; & \frac{\hbar}{M}\mathrm{Im}\left[\psi_1^\dagger \frac{\partial\psi_1}{\partial x}|\boldsymbol{S}_1|^2 + \psi_1^\dagger \frac{\partial\psi_2}{\partial x}\boldsymbol{S}_1^\dagger \boldsymbol{S}_2\right] + \\ & \frac{\hbar}{M}\mathrm{Im}\left[\psi_2^\dagger \frac{\partial\psi_1}{\partial x}\boldsymbol{S}_2^\dagger \boldsymbol{S}_1 + \psi_2^\dagger \frac{\partial\psi_2}{\partial x}|\boldsymbol{S}_2|^2\right], \end{aligned} \tag{5.14}$$

where $\boldsymbol{S}_1 \equiv \boldsymbol{S}_1(t)$ and $\boldsymbol{S}_2 \equiv \boldsymbol{S}_2(t)$. As one can see in Eq.(5.14), the interference, seen in the case of wave packets as fast oscillations in the coordinate or time-dependence of the current, is controlled by the spin states with the product $\boldsymbol{S}_1^\dagger \boldsymbol{S}_2$. In this formula we neglected the last term of (5.9), assuming a weak spin-orbit coupling.

If these two packets moving with velocities v_1, v_2 meet after the time-of-flight t_0, at a position x_0, their initial positions were

$$x_j = x_0 - v_j t_0. \tag{5.15}$$

In the presence of spin-orbit coupling, the mutual orientation of the spins of the condensates, and, in turn, their interference, depends on the time of flight. In particular, if at $t = t_0$ the spins states are orthogonal, the interference disappears, showing that it can be controlled by manipulating the condensate spin.

Assuming that both packets are well-defined in the momentum space, we use (5.10) and find the product of two spin states

$$\boldsymbol{S}_1^\dagger(t)\boldsymbol{S}_2(t) = \boldsymbol{S}_1^\dagger(0) e^{i\widehat{H}_{\mathrm{so}1}t/\hbar} e^{-i\widehat{H}_{\mathrm{so}2}t/\hbar}\boldsymbol{S}_2(0) = \cos\theta(t), \tag{5.16}$$

where the angle between the condensates' spins at time t is

$$\theta(t) = \frac{\alpha}{\hbar^2}\,(p_1 - p_2)\,t. \tag{5.17}$$

Let us now consider a specific example. We use in numerical calculations the system of units with $\hbar \equiv 1$, mass $M \equiv 1$, unit of length 1μm and dimensionless parameters:

$$\begin{aligned} & p_1 = 8,\ p_2 = 2,\ A_1 = A_2 = 1/\sqrt{2}, \\ & \beta_{11}(0) = \beta_{12}(0) = \beta_{21}(0) = \beta_{22}(0) = 1/\sqrt{2}, \end{aligned} \tag{5.18}$$

corresponding to both condensates with the spin oriented along the x-axis. We take time-of-flight $t_0 = 20$ and the condensate "collision" the point $x_0 = 0$. To make connection with possible experimental observations, we take ^{87}Rb atom as an example. The resulting velocity unit $\hbar/(M_{\mathrm{Rb}} \times 10^{-4}\ \mathrm{cm})$ is 0.072 cm/s and, therefore, the unit of time is approximately 1.4×10^{-3} s. As a result, time scale of the problem $t_0 = 20$ corresponds to about 28 milliseconds and an initial distance between the packets (for $p_1 = 8$ and $p_2 = 2$) is 120 micron. Below we consider two realizations of the condensates, with equal and different widths.

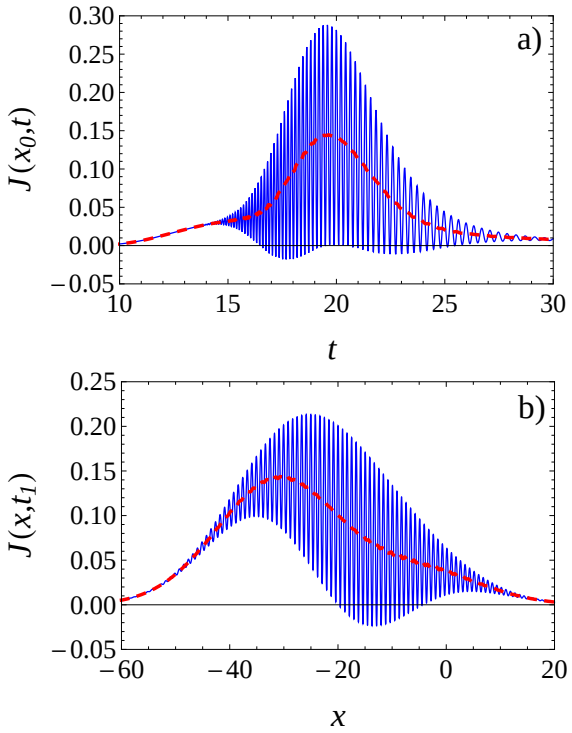

Figure 5.2: Plot of current (a) vs time at $x = x_0$ and (b) vs coordinate at $t = t_1$ ($t_1 = 16$), for the parameters in (5.18). Color lines correspond to values of spin-orbit coupling from (5.19) and (5.20), α_1 - red dashed line, α_2 - blue solid line.

1. First we take both initial widths equal, $w_1(0) = w_2(0) = 1$. At the meeting time t_0, if the spin states of the condensates are orthogonal, that is $\cos\theta(t_0) = 0$, the interference will be destroyed. For $\cos\theta(t_0) = \pm 1$, we obtain the constructive (destructive) interference with similar fringes, just shifted by a half of the period. Here the interference is maximal and, for $\cos\theta(t_0) = 1$, the same as in the absence of spin-related effects. We take spin-orbit coupling corresponding to the two realizations (see (5.17)):

$$\alpha_1 = \frac{\pi\hbar^2}{2(p_1 - p_2)t_0}, \qquad \theta(t_0) = \pi/2 \tag{5.19}$$

$$\alpha_2 = \frac{\pi\hbar^2}{(p_1 - p_2)t_0}, \qquad \theta(t_0) = \pi \tag{5.20}$$

respectively.

In Figure 5.2 one can see that, for $\alpha = \alpha_1$ there is no interference in the flux, while for $\alpha = \alpha_2$ the flux is characterized by a strong interference pattern and by the presence of backflow, namely a negative current density, $J(x_0, t) < 0$, see

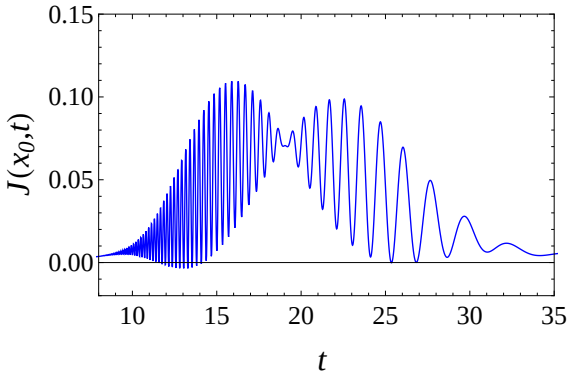

Figure 5.3: Plot of current density for $p_1 = 5$, $p_2 = 2.5$, $\alpha = 0.09$, $w_1(0) = 0.5$, $w_2(0) = 20$ and other parameters from (5.18). For these parameters the number of no-interference points in (5.25) is $N_{\cos\theta=0} \approx 1$.

Fig. 5.2 [166–173]. For other values of spin-orbit coupling the flux interference is between these two limits.

2. For different initial widths of the packets at the time-of-flight t_0 the widths of the packets can be, in general, different. The same holds for the travel time of the packets through the point x_0 defined as

$$T_j \approx 2\frac{w_j(t_0)}{v_j}, \tag{5.21}$$

where v_1 and v_2 are the velocities of the packets determined in (5.8), $w_1(t_0)$ and $w_2(t_0)$ are the widths of the packets at the meeting time t_0 determined in (5.7), and we have taken into account that the traveling time of wave function is the order of $2w_j(t)$.

In this case, the duration of the interference (interference time) is

$$T_{\rm int} \approx \min\{T_1,\ T_2\}. \tag{5.22}$$

From (5.17) we define one rotation period $T_{\rm rot}$ as

$$\theta(T_{\rm rot}) = 2\pi \tag{5.23}$$

and obtain

$$T_{\rm rot} = \frac{2\pi\hbar^2}{\alpha(p_1 - p_2)}. \tag{5.24}$$

If the coupling α is large, the spins of the packets rotate fast and during the time interval $T_{\rm int}$ the interference would be destroyed several times depending on the rotation rate. Then the number of points in time domain where the interference disappears can be estimated as:

$$N_{\cos\theta=0} \approx 2\frac{T_{\rm int}}{T_{\rm rot}}. \tag{5.25}$$

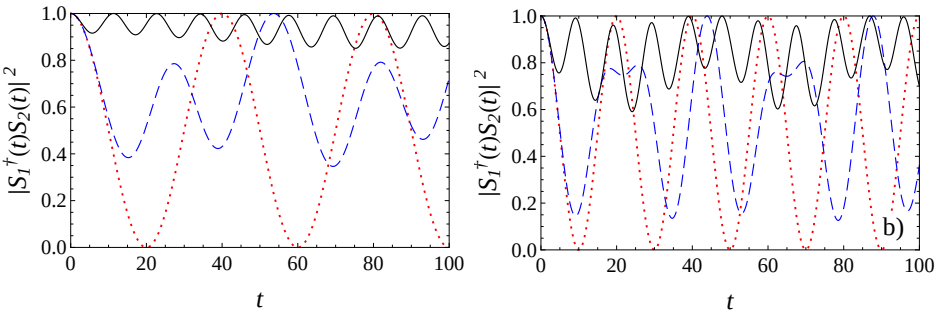

Figure 5.4: Products of spinors for values in (5.18) for the spin-orbit coupling from (5.19) and (5.20): (a) - α_1 and (b) - α_2. Lines correspond to: $\Delta_Z = 0$ - red dot line, $\Delta_Z = 0.1$ - blue dashed line, and $\Delta_Z = 0.5$ - black solid line.

In this formula the factor 2 means that, in one period of rotation of the angle between spins, the interference will be destroyed twice when spin states are orthogonal. In addition, if the packets are initially narrow, and, therefore, spread with a large rate of the order of $\hbar/Mw_j$, one can see the effect of multiple interferences better.

From Fig. 5.3 we can see that, during the interference time the spin states will be orthogonal once, and the interference will be destroyed at this instant.

5.3 Interference and quantum backflow in a Zeeman field

Here we consider the effect of Zeeman splitting in a synthetic magnetic field on the interference of condensates. We will limit ourselves to considering only equal initial widths of the packets with all other initial parameters unchanged. To see the spin precession clearly, we take for simplicity the field along the x- axis since the spin-orbit coupling is along the z- axis. Then the Hamiltonian becomes:

$$\widehat{H} = \frac{\widehat{p}^2}{2M} + \frac{\alpha}{\hbar}\widehat{p}\widehat{\sigma}_z + \frac{\Delta_Z}{2}\widehat{\sigma}_x, \tag{5.26}$$

where Δ_Z is the Zeeman splitting, and $\widehat{\sigma}_x$ is the corresponding Pauli matrix. In this system the spin rotates around the axis (cf. Fig.5.1):

$$\boldsymbol{n}_j = \frac{2}{\hbar\Omega_j}\left[\frac{\Delta_Z}{2},\ 0,\ \frac{\alpha p_j}{\hbar}\right], \tag{5.27}$$

with the rate

$$\Omega_j = \frac{2}{\hbar}\sqrt{\left(\frac{\alpha p_j}{\hbar}\right)^2 + \left(\frac{\Delta_Z}{2}\right)^2}. \tag{5.28}$$

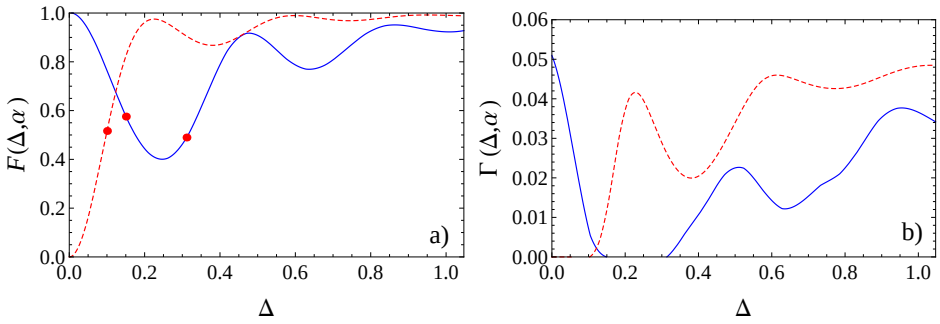

Figure 5.5: The evaluation of interferences (a) and backflow (b) for values from (5.18), $w_1(0) = w_2(0) = 1$ and spin-orbit coupling from (5.19) and (5.20) α_1-dashed red line, α_2-solid blue line. In (a) small circles mark appearance and disappearance of the backflow.

Figure 5.1 shows the time-dependent spins of two condensates in the presence of synthetic magnetic field and the directions of the vectors (5.27). If the condition $\Delta_Z \gg \alpha p_j/\hbar$ is satisfied, then the vectors (5.27) are very close to each other and to the x-axis, and the spins be always parallel to each other with a high accuracy.

From the spin-related contribution to Hamiltonian (5.26)

$$\widehat{H}_{soj} = \frac{\alpha}{\hbar} p_j \widehat{\sigma}_z + \frac{\Delta_Z}{2} \widehat{\sigma}_x, \tag{5.29}$$

and using Eq.(5.16) we find the product of spin states:

$$\begin{aligned} \boldsymbol{S}_1^\dagger(t)\boldsymbol{S}_2(t) &= \frac{\hbar^2\Delta_Z^2 + 4p_1p_2\alpha^2}{\hbar^4\Omega_1\Omega_2} \sin\frac{\Omega_2 t}{2}\sin\frac{\Omega_1 t}{2} + \cos\frac{\Omega_2 t}{2}\cos\frac{\Omega_1 t}{2} \\ &+ \frac{i}{\hbar}\left[\frac{\Delta_Z}{\Omega_2}\sin\frac{\Omega_2 t}{2}\cos\frac{\Omega_1 t}{2} - \frac{\Delta_Z}{\Omega_1}\cos\frac{\Omega_2 t}{2}\sin\frac{\Omega_1 t}{2}\right], \end{aligned} \tag{5.30}$$

where Ω_1 and Ω_2 are defined by (5.28). As a result, the interference can be controlled by spin-orbit coupling and Zeeman splitting. At $\Delta_Z = 0$ equations (5.30) and (5.16) coincide. Figure 5.4 demonstrates the spin states (5.30) and shows that the expression (5.30) is zero only when $\Delta_Z = 0$. As a result with synthetic magnetic field the interference cannot be completely destroyed by spin-orbit coupling.

Now we evaluate the effect of $\boldsymbol{S}_1^\dagger(t)\boldsymbol{S}_2(t)$ on the time-dependent flux as a function of the synthetic magnetic field. For this purpose we use the Fourier series in the time domain and define:

$$J(t) \equiv \sqrt{\frac{2}{T_2 - T_1}} \sum_{n=1}^{n_{\max}} J_n \sin\frac{\pi n(t - T_1)}{T_2 - T_1}, \tag{5.31}$$

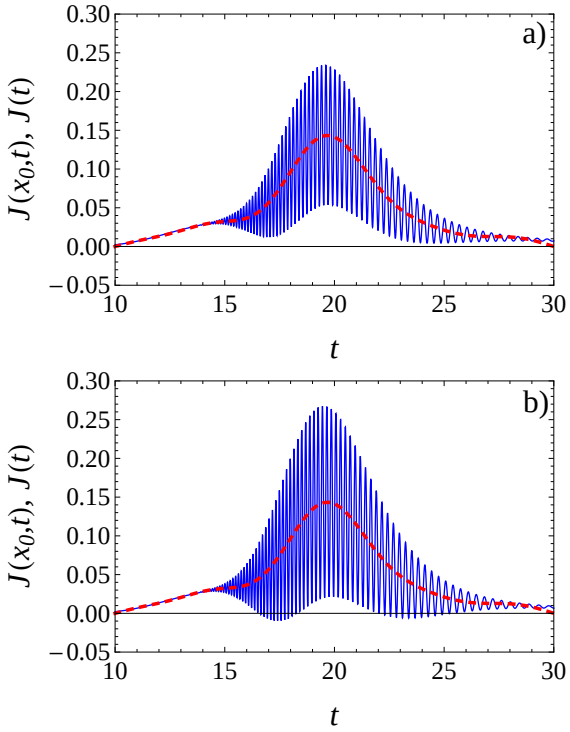

Figure 5.6: The fluxes for values from (5.18), spin-orbit coupling is α_2 from (5.20), and the plots correspond to the fields with $\Delta_Z = 0.26$ (a) and $\Delta_Z = 0.63$ (b). Lines correspond to functions (5.9) - blue solid line and (5.31) - with $n_{max} = 10$ red dashed line.

with the coefficients J_n

$$J_n = \sqrt{\frac{2}{T_2 - T_1}} \int_{T_1}^{T_2} J(x_0, t) \sin \frac{\pi n (t - T_1)}{T_2 - T_1} dt, \tag{5.32}$$

where $[T_1, T_2]$, $(T_1 = 0,\ T_2 = 30)$ is the full collision time interval. For summation limit $n_{\max} \to \infty$ the function (5.31) is $J(x_0, t)$ in (5.9). To quantitatively describe the interference, first we filter out high-frequency Fourier components from the time dependence by taking a smaller $n_{\max}$ (in our case $n_{\max} = 10$) limit in Eq.(5.31). Now, the high-frequency terms do not contribute, and in Fig. 5.6 we see that plot of the function (5.9) symmetrically oscillates around the plot of the filtered function (5.31). The maximal amplitude of oscillation is obtained for $\alpha = 0$ and $\Delta_Z = 0$. As a result, we can define the value corresponding to the strongest interference as:

$$F_{\max} = \int_{T_1}^{T_2} \left[J(x_0, t) - J(t) \right]^2 dt \qquad (\Delta_Z = 0, \alpha = 0) \tag{5.33}$$

having the value of ≈ 0.04 at given system parameters. The efficiency of the interference as a function of Δ_{Z} is characterized by:

$$F(\Delta_{\mathrm{Z}}, \alpha) = \frac{1}{F_{\max}} \int_{T_1}^{T_2} \left[J(x_0, t) - J(t)\right]^2 dt, \tag{5.34}$$

and the contribution of the backflow is evaluated as:

$$\Gamma(\Delta_{\mathrm{Z}}, \alpha) = \frac{2}{F_{\max}} \int_{T_1}^{T_2} J(t) \left[|J(x_0, t)| - J(x_0, t)\right] dt. \tag{5.35}$$

The evaluation of interference and backflow, (5.34) and (5.35) dependent on Δ_{Z} is plotted in Fig. 5.5 for given values of spin-orbit coupling (5.19) and (5.20). Figures 5.5 and 5.6 show that it is possible to control the interference of two condensates using the spin-orbit coupling and synthetic magnetic field. For strong Zeeman field spins of particles will be frozen in one direction and interference will be maximal. The zero value of the function $\Gamma(\Delta_{\mathrm{Z}}, \alpha)$ corresponds to the absence of the backflow, where the flux $J(x_0, t) > 0$ for any t. As we can see, the intervals of its zero values are relatively small, meaning that the backflow is robust against the spin-dependent interactions. Figure 5.5 shows that for the given system parameters the backflow disappears if the interference parameter $F(\Delta_{\mathrm{Z}}, \alpha)$ is less than 0.5.

A comment on the role of the interactions is in order. Since interactions do not influence the momentum of the packet, they do not change its mean spin precession rate, affecting the spinors only marginally. However they do influence the packet width and can prevent collision if they are strong enough. To avoid these effects in the regime $p_1 w_1(0) \gg \hbar$ and $p_2 w_2(0) \gg \hbar$ it is sufficient to satisfy the condition of small contribution of the interatomic repulsion into the packet width. Since in the absence of repulsion the packet spreads with the rate of the order of $\hbar/M w_j$, the interaction energy per atom should be less than $\hbar^2/M w_j^2$ to satisfy this condition. A good candidate for a very weakly interacting BEC is ^{7}Li ensemble, although, to the best of our knowledge, spin-orbit coupling effects have not been reported for this isotope.

As a conclusion of this Chapter, we have shown that two freely moving spin-orbit coupled condensates strongly depend on the total spin states, namely from the spin precession angles of the condensates. By using spin-orbit coupling and synthetic magnetic field, one can control the interference and quantum backflow effects of the condensates.

Chapter 6

Macroscopic spin qubit in spin-orbit coupled Bose-Einstein condensates

In this Chapter we consider a macroscopic spin qubit based on spin-orbit coupled Bose-Einstein condensates, where, in addition to the spin-orbit coupling, spin dynamics strongly depends on the interaction between particles. The evolution of the spin for freely expanding, trapped, and externally driven condensates is investigated. For condensates oscillating at the frequency corresponding to the Zeeman splitting in the synthetic magnetic field, the spin Rabi frequency does not depend on the interaction between the atoms since it produces only internal forces and does not change the total momentum. However, interactions and spin-orbit coupling bring the system into a mixed spin state, where the total spin is inside rather than on the Bloch sphere. This greatly extends the available spin space making it three-dimensional, but imposes limitations on the reliable spin manipulation of such a macroscopic qubit. The spin dynamics can be modified by introducing suitable spin-dependent initial phases, determined by the spin-orbit coupling, in the spinor wave function.

6.1 Introduction

One of the prospective applications of spin-orbit coupled Bose-Einstein condensates consists in the realization of macroscopic spin qubits [21]. A more detailed analysis of quantum computation based on a two-component BEC was proposed in [178]. The gates for performing these operations can be produced by means of the SOC and of an external synthetic magnetic field. Due to the SOC, a periodic mechanical motion of the condensate drives the spin dynamics and can cause spin-flip transitions at the Rabi frequency depending on the SOC strength. This technique, known in semiconductor physics as the electric dipole spin resonance, is well suitable for the manipulation of qubits based on the spin of a single electron [179–181]. For the macroscopic spin qubits based on Bose-Einstein condensate, the physics is different in at least two aspects. First, a relative effect of the SOC compared to the kinetic energy can be much stronger here than in semiconductors. Second, the interaction between the bosons can have a strong effect on the entire spin dynamics.

In this Chapter, we study how the spin evolution of a quasi one-dimensional Bose-Einstein condensate depends on the repulsive interaction between the particles and on the SOC strength. First, we find the ground state properties of a quasi-one dimensional condensate and consider simple spin-dipole oscillations. Second, we analyze, by means of the Gross-Pitaevskii approach, the dynamics of free, harmonically trapped, and mechanically driven macroscopic qubits based on such a condensate. We assume that the periodic mechanical driving resonates with the Zeeman transition in the synthetic magnetic field and find different regimes of the spin qubit operation in terms of the interaction between the atoms, and the driving. We show that some control of the spin qubit state can be achieved by introducing phase factors, dependent on the SOC, in the spinor wave function.

6.2 Ground state and spin-dipole oscillations

6.2.1 Ground state energy and wave function

Before analyzing the spin qubit dynamics, we obtain the ground state of an interacting BEC. In particular, we consider a harmonically trapped quasi one-dimensional condensate, tightly bounded in the transverse directions. The system can be described by the following effective Hamiltonian, where the interactions between the atoms are taken into account in the Gross-Pitaevskii form:

$$\widehat{H}_0 = \frac{\widehat{p}^2}{2M} + \frac{M\omega_0^2}{2}x^2 + g_1|\psi(x)|^2. \tag{6.1}$$

Here $\psi(x)$ is the condensate wave function, M is the particle mass, ω_0 is the frequency of the trap (with the corresponding oscillator length $a_{\rm ho} = \sqrt{\hbar/M\omega_0}$), and $g_1 = 2a_s\hbar\omega_\perp$ is the effective one-dimensional interaction constant, with a_s being the scattering length of interacting particles, and $\omega_\perp \gg \omega_0$ being the transverse confinement frequency. Below in calculations we put $\hbar \equiv M \equiv 1$, and measure energy in units of ω_0 and length in units of $a_{\rm ho}$, respectively. All the effects of the interaction are determined by the dimensionless parameter $\widetilde{g}_1 N$, where $\widetilde{g}_1 = 2\widetilde{a}_s\widetilde{\omega}_\perp$,

where $\widetilde{a}_s$ is the scattering length in the units of $a_{\rm ho}$, $\widetilde{\omega}_\perp$ is the transverse confinement frequency in the units of ω_0, and N is the number of particles. In physical units, for a condensate of ^{87}Rb and an axial trapping frequency $\omega_0 = 2\pi \times 10$ Hz, the unit of time corresponds to 0.016 s, the unit of length $a_{\rm ho}$ corresponds to 3.4 μm, and the unit of speed $a_{\rm ho}\omega_0$ becomes 0.021 cm/s, respectively. In addition, considering that $a_s = 100a_{\rm B}$, $a_{\rm B}$ being the Bohr radius, in the presence of a transverse confinement with frequency $\omega_\perp = 2\pi \times 100$ Hz the dimensionless coupling constant $\widetilde{g}_1$ turns out to be of the order of 10^{-3}.

In order to find the BEC ground state we minimize the total energy in a properly truncated harmonic oscillator basis. To design the wave function we take the real sum of even-order eigenfunctions

$$\psi_0(x) = N^{1/2} \sum_{n=0}^{n_{\rm max}} C_{2n}\varphi_{2n}(x). \tag{6.2}$$

Here

$$\varphi_{2n}(x) = \frac{1}{\sqrt{\pi^{1/2}(2n)!2^{2n}}} H_{2n}\left(x\right) \exp\left[-\frac{x^2}{2}\right], \tag{6.3}$$

where $H_{2n}\left(x\right)$ are the Hermite polynomials, and the normalization is fixed by requiring that

$$\sum_{n=0}^{n_{\rm max}} C_{2n}^2 = 1. \tag{6.4}$$

The coefficients C_{2n} are determined by minimizing the total energy $E_{\rm tot}$, such that

$$E_{\rm min} = \min_{C_{2n}} \left\{E_{\rm tot}\right\}, \tag{6.5}$$

where

$$E_{\rm tot} = \frac{1}{2}\int \left[\left(\psi'(x)\right)^2 + x^2\psi^2(x) + \widetilde{g}_1\psi^4(x)\right] dx, \tag{6.6}$$

and $|C_{2n_{\rm max}}| \ll 1$.

Formulas (6.5) and (6.6) yield the ground state energy, while the width of the condensate is defined as:

$$w_{\rm gs} = \left[\frac{2}{N}\int x^2|\psi_0(x)|^2 dx\right]^{1/2}. \tag{6.7}$$

In the non interacting limit, $\widetilde{g}_1 = 0$, $\psi_0(x)$ is the ground state of the harmonic oscillator ($n_{\rm max} = 0$), that is a Gaussian function with $w_{\rm gs} = 1$. In the opposite, strong coupling limit $\widetilde{g}_1 N \gg 1$, the exact wave function (6.2) is well reproduced (see Figure 6.1) by the Thomas-Fermi expression

$$\psi_{\rm TF}(x) = \frac{\sqrt{3}}{2}\frac{\sqrt{N}}{w_{\rm TF}^{3/2}}\left(w_{\rm TF}^2 - x^2\right)^{1/2}; \quad |x| \le w_{\rm TF}, \tag{6.8}$$

where $w_{\rm TF} = \left(3\widetilde{g}_1 N/2\right)^{1/3}$.

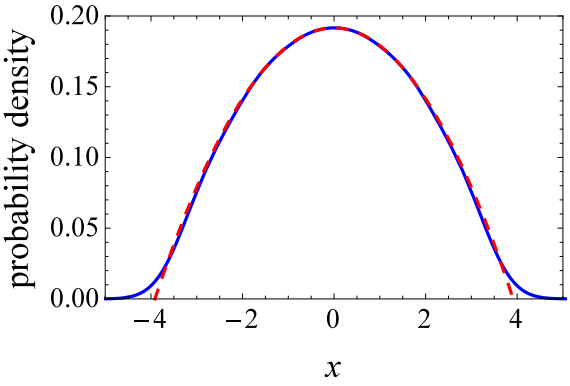

Figure 6.1: Ground-state probability density of the condensate obtained from (6.2)-(6.6) (blue solid line), compared with the Thomas-Fermi approximation in (6.8) (red dashed line) for $\widetilde{g}_1 N = 40$.

In general, for a qualitative description of the ground state one can use instead of the exact wave function (6.2), the Gaussian ansatz

$$\psi_{\rm G}(x) = \left(\frac{N}{\pi^{1/2} w}\right)^{1/2} \exp\left[-\frac{x^2}{2w^2}\right], \tag{6.9}$$

where the width w is single variational parameter for the energy minimization. Then the total energy (6.6) becomes:

$$E_{\rm tot} = N\left[\frac{1}{4}\left(w^2 + \frac{1}{w^2}\right) + \frac{\widetilde{g}_1 N}{2(2\pi)^{1/2} w}\right]. \tag{6.10}$$

The latter is minimized with respect to w by solving the equation

$$\frac{dE_{\rm tot}}{dw} = N\left[\frac{1}{2}\left(w - \frac{1}{w^3}\right) - \frac{\widetilde{g}_1 N}{2(2\pi)^{1/2} w^2}\right] = 0. \tag{6.11}$$

In the strong coupling regime, $\widetilde{g}_1 N \gg 1$, we have $w \gg 1$ so that - to a first approximation - the kinetic term $\propto 1/w^3$ in (6.11) can be neglected, yielding the following value for the width of the ground state:

$$\widetilde{w} = \left(\frac{\widetilde{g}_1 N}{\sqrt{2\pi}}\right)^{1/3}. \tag{6.12}$$

The first order correction can be obtained by writing $w = \widetilde{w} + \epsilon$ ($\epsilon \ll 1$), so that from (6.11) it follows:

$$w = \left(\frac{\widetilde{g}_1 N}{\sqrt{2\pi}}\right)^{1/3} + \frac{\sqrt{2\pi}}{3\widetilde{g}_1 N}. \tag{6.13}$$

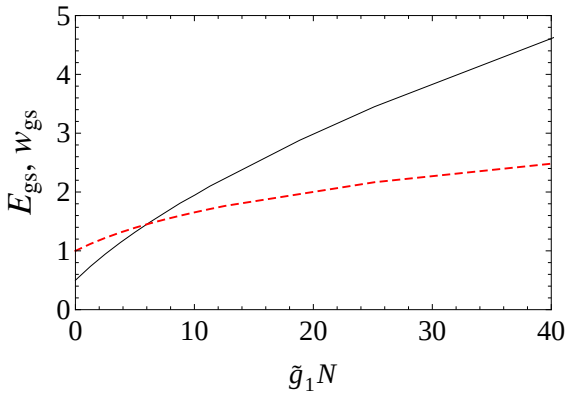

Figure 6.2: Ground state energy (black solid line) and condensate width (red dashed line) vs. the interaction parameter $\widetilde{g}_1 N$.

By substituting (6.13) in (6.10) we obtain that the leading term in the ground state energy for $\widetilde{g}_1 N \gg 1$ is:

$$E_{\min}^{[\mathrm{G}]} = \frac{3}{4} N \left(\frac{\widetilde{g}_1 N}{\sqrt{2\pi}} \right)^{2/3}. \tag{6.14}$$

In Figure 6.2 we plot the ground state energy and the condensate width as a function of the interaction, as obtained numerically from (6.5) and (6.7), respectively. As expected, in the strong coupling regime $\widetilde{g}_1 N \gg 1$ both quantities nicely follow the behavior (not shown in the Figure) predicted both by the Gaussian approximation and by the exact solution, namely $E_{\min} \propto (\widetilde{g}_1 N)^{2/3}$ and $w_{\mathrm{gs}} \propto (\widetilde{g}_1 N)^{1/3}$.

6.2.2 Simple spin-dipole oscillations

Let us now turn to the case of a condensate of pseudospin 1/2 atoms. Here the system is described by a two-component spinor wave function $\Psi = [\psi_\uparrow(x,t), \psi_\downarrow(x,t)]^T$, still normalized to the total number of particles N. The interaction energy (third term in the functional (6.6)) now acquires the form (see, e.g. [146])

$$E_{\mathrm{int}} = \frac{1}{2} \widetilde{g}_1 \int \left[|\psi_\uparrow(x,t)|^2 + |\psi_\downarrow(x,t)|^2 \right]^2 dx, \tag{6.15}$$

where, for simplicity and qualitative analysis, we neglect the dependence of interatomic interaction on the spin component $\uparrow$ or $\downarrow$ and characterize all interactions by a single constant $\widetilde{g}_1$.

Here we consider spin dipole oscillations, induced by a given small initial symmetric displacement of the two spin components $\pm\xi$. For a qualitative understanding, we assume a negligible spin-orbit coupling and a Gaussian form of the wave

function presented as

$$\Psi_{\mathrm{G}}(x) = \frac{1}{\sqrt{2}} \begin{bmatrix} \psi_{\mathrm{G}}(x-\xi) \\ \psi_{\mathrm{G}}(x+\xi) \end{bmatrix}, \tag{6.16}$$

where ψ_{G} is given by (6.9), and $\xi \ll w$. The corresponding energy is given by:

$$E = E_{\mathrm{min}}^{[\mathrm{G}]} + E_{\mathrm{sh}}, \tag{6.17}$$

where $E_{\mathrm{min}}^{[\mathrm{G}]}$ is defined by (6.14) and E_{sh} is the shift-dependent contribution:

$$E_{\mathrm{sh}} = \frac{N}{2}\xi^2 \left(1 - \frac{\widetilde{g}_1 N}{\sqrt{2\pi}w^3}\right). \tag{6.18}$$

Then, it follows that the corresponding oscillation frequency is

$$\omega_{\mathrm{sh}} = \sqrt{1 - \frac{\widetilde{g}_1 N}{\sqrt{2\pi}w^3}}. \tag{6.19}$$

For strong interaction ($\widetilde{g}_1 N \gg 1$) by substituting (6.13) in (6.19) we obtain:

$$\omega_{\mathrm{sh}} \approx \left(\frac{\sqrt{2\pi}}{\widetilde{g}_1 N}\right)^{2/3}. \tag{6.20}$$

Therefore, for strong interaction the frequency of the spin dipole oscillations falls as $(\widetilde{g}_1 N)^{-2/3}$, and this result is common for the Gaussian ansatz and for the exact solution; it will be useful in the following section.

6.3 Spin evolution and interaction effects

6.3.1 Hamiltonian and spin density matrix

To consider the evolution of the driven quasi one dimensional pseudospin-1/2 SOC condensate we begin with the effective Hamiltonian

$$\widehat{H} = \alpha\widehat{\sigma}_z\widehat{p} + \frac{\widehat{p}^2}{2} + \frac{\Delta}{2}\widehat{\sigma}_x + \frac{1}{2}(x - d(t))^2 + \widetilde{g}_1 |\Psi|^2. \tag{6.21}$$

Here α is the SOC constant (see [139] and [140] for comprehensive review on the SOC in cold atomic gases), $\widehat{\sigma}_x$ and $\widehat{\sigma}_z$ are the Pauli matrices, Δ is the synthetic Zeeman splitting, and $d(t)$ is the driven displacement of the harmonic trap center as can be obtained by a slow motion of the intersection region of laser beams trapping the condensate.

The two-component spinor wave function Ψ is obtained as a solution of the nonlinear Schrödinger equation

$$i\frac{\partial\Psi}{\partial t} = \widehat{H}\Psi. \tag{6.22}$$

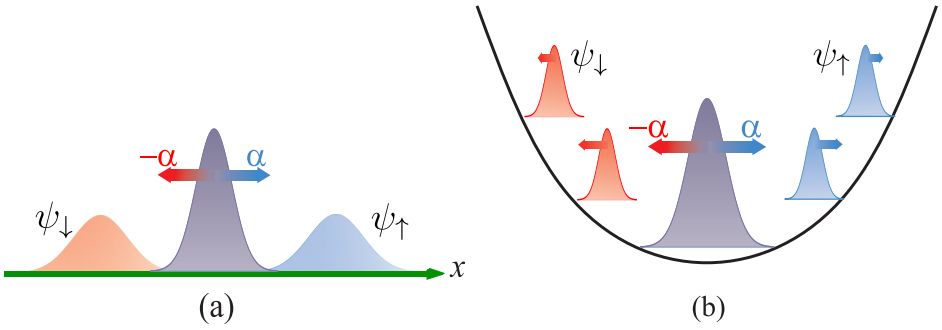

Figure 6.3: (Color online) (a) Separation of a freely expanding condensate in two spin-up and spin-down components with opposite anomalous velocities. (b) Oscillation of the spin-up and spin-down components in the harmonic trap.

To describe spin evolution we introduce the reduced density matrix

$$\rho(t) \equiv |\Psi\rangle\langle\Psi| = \begin{bmatrix} \rho_{11}(t) & \rho_{12}(t) \\ \rho_{21}(t) & \rho_{22}(t) \end{bmatrix}, \tag{6.23}$$

where we trace out the $x-$dependence by calculating integrals

$$\begin{aligned} \rho_{11}(t) &= \int |\psi_\uparrow(x,t)|^2 dx, \;\; \rho_{22}(t) = \int |\psi_\downarrow(x,t)|^2 dx, \\ \rho_{12}(t) &= \int \psi_\uparrow^*(x,t)\psi_\downarrow(x,t)dx, \quad \rho_{21}(t) = \rho_{12}^*(t), \end{aligned} \tag{6.24}$$

and, as a result,

$$\mathrm{tr}\left(\rho(t)\right) \equiv \rho_{11}(t) + \rho_{22}(t) = N. \tag{6.25}$$

Although the $|\Psi\rangle$ state is pure, integration in (6.24) produces $\rho(t)$ formally describing a mixed state in the spin subspace. One can characterize the resulting spin state purity by a parameter P defined as

$$P = \frac{2}{N^2}\left(\mathrm{tr}\left(\rho^2\right) - \frac{N^2}{2}\right), \tag{6.26}$$

where $0 \leq P \leq 1$,

$$\mathrm{tr}\left(\rho^2\right) = N^2 + 2(|\rho_{12}|^2 - \rho_{11}\rho_{22}), \tag{6.27}$$

and we omitted the explicit $t-$dependence for brevity. The system is in the pure state when $P = 1$, that is $\mathrm{tr}\left(\rho^2\right) = N^2$ with $\rho_{11}\rho_{22} = |\rho_{12}|^2$. In the fully mixed state, where $\mathrm{tr}\left(\rho^2\right) = N^2/2$, we have $P = 0$ with

$$\rho_{11} = \rho_{22} = \frac{N}{2}, \qquad \rho_{12} = 0. \tag{6.28}$$

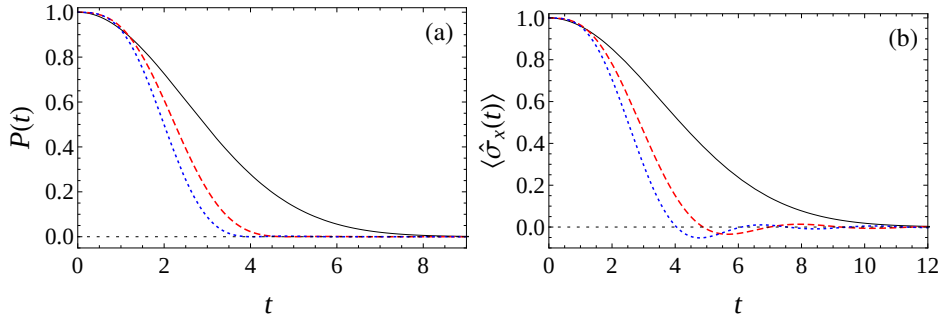

Figure 6.4: (Color online) (*a*) Purity and (*b*) spin component as a function of time for a condensate released from the trap, for $\alpha = 0.2$. The lines correspond to $\widetilde{g}_1 N = 0$ (black solid line; for the purity cf. (6.32)), $\widetilde{g}_1 N = 10$ (red dashed line), and $\widetilde{g}_1 N = 20$ (blue dot-dashed line).

The spin components defined by $\langle\widehat{\sigma}_i\rangle \equiv \mathrm{tr}\,(\widehat{\sigma}_i\rho)/N$ become

$$\langle\widehat{\sigma}_x\rangle = \frac{2}{N}\mathrm{Re}(\rho_{12}), \quad \langle\widehat{\sigma}_y\rangle = -\frac{2}{N}\mathrm{Im}(\rho_{12}),$$
$$\langle\widehat{\sigma}_z\rangle = \frac{2}{N}\rho_{11} - 1, \tag{6.29}$$

and the purity $P = \sum_{i=1}^{3}\langle\widehat{\sigma}_i\rangle^2$, which allows one to match the value of P and the length of the spin vector inside the Bloch sphere. For a pure state $\sum_{i=1}^{3}\langle\widehat{\sigma}_i\rangle^2 = 1$, and the total spin is on the Bloch sphere. Instead, for a fully mixed state $\sum_{i=1}^{3}\langle\widehat{\sigma}_i\rangle^2 = 0$, and the spin null.

6.3.2 A simple condensate motion

Let us suppose that a condensate of interacting spin-orbit coupled particles is located in a harmonic trap and characterized by an initial wave function

$$\Psi_0(x,0) = \frac{1}{\sqrt{2}}\psi_{\mathrm{in}}(x)\begin{bmatrix} 1 \\ 1 \end{bmatrix}, \tag{6.30}$$

with the spin parallel to the $x-$axis.

The spin-orbit coupling modifies the commutator corresponding to the velocity operator by introducing the spin-dependent contribution as:

$$\widehat{v} \equiv i\left[\frac{\widehat{p}^2}{2} + \alpha\widehat{\sigma}_z\widehat{p}, \widehat{x}\right] = \widehat{p} + \alpha\widehat{\sigma}_z. \tag{6.31}$$

The effect of the spin-dependent anomalous velocity term on the condensate motion was clearly observed experimentally in [149] as the spin-induced dipole oscillations and in [177] as the *Zitterbewegung*. Since the initial spin in (6.30) is parallel to the x-axis, the expectation value of the velocity vanishes, $\langle\widehat{v}\rangle = 0$.

Free and oscillating motion of the BEC is shown in Figure 6.3(a) and Figure 6.3(b), respectively. When one switches off the trap, the condensate is set free, and the two spin components start to move apart and the condensate splits up, see Figure 6.3(a). Each spin-projected component broadens due to the Heisenberg momentum-coordinate uncertainty and interaction. The former effect is characterized by a rate proportional to $1/w_{\rm gs}$. At large $\widetilde{g}_1 N$, the width $w_{\rm gs} \sim (\widetilde{g}_1 N)^{1/3}$, and, as a result, the quantum mechanical broadening rate decreases as $(\widetilde{g}_1 N)^{-1/3}$. At the same time, the repulsion between the spin-polarized components accelerates the peak separation [1] and leads to the asymptotic separation velocity $\sim (\widetilde{g}_1 N)^{1/2}$. This acceleration by repulsion leads to opposite time-dependent phase factors in $\psi_\uparrow(x,t)$ and $\psi_\downarrow(x,t)$ in (6.24) and, therefore, results in decreasing in $|\rho_{12}(t)|$ and in the purity. Thus, with the increase in the interaction, the purity and the $x-$ spin component asymptotically tend to zero faster, as demonstrated in Figure 6.4. For a noninteracting condensate with the initial Gaussian wave function $\psi_{\rm in} \sim \exp\left(-x^2/2w^2\right)$ the purity can be written analytically as

$$P_0(t) = \exp\left[-2\left(\frac{\alpha t}{w}\right)^2\right]. \tag{6.32}$$

In the presence of the trap (figure 6.3(b)), the anomalous velocity in (6.31) causes spin components (spin-dipole) oscillations with a characteristic frequency of the order of $\omega_{\rm sh}$ in (6.20). With the increase in the interatomic interaction, the frequency $\omega_{\rm sh}$ decreases and, therefore, the amplitude of the oscillations arising due to the anomalous velocity ($\sim \alpha/\omega_{\rm sh}$) increases. As a result, the acceleration and separation of the spin-projected components increase, the off-diagonal components of the density matrix in (6.24) became smaller, and the minimum in $P(t)$ rapidly decreases to $P(t) \ll 1$ as shown by the exact numerical results presented in Figures 6.5(a) and (b) [2]. In Figure 6.5(c) we show the corresponding evolution of spin density dipole moment

$$\langle x\widehat{\sigma}_z\rangle = \frac{1}{N}\int \Psi^\dagger x\widehat{\sigma}_z\Psi dx. \tag{6.33}$$

Here the oscillation frequency is a factor of two larger than that of the spin density oscillation.

6.3.3 Qubit dynamics

To manipulate the macroscopic spin qubit, the center of the trap is driven harmonically at the frequency corresponding to the Zeeman splitting Δ as

$$d(t) = d_0 \sin(\Delta t), \tag{6.34}$$

where d_0 is an arbitrary amplitude. For a noninteracting condensate and a very weak spin-orbit coupling, the spin component $\langle\widehat{\sigma}_x(t)\rangle$ is expected to oscillate roughly as

$$\langle\widehat{\sigma}_x(t)\rangle = \cos(\Omega_R t), \tag{6.35}$$

[1] This procedure models the von Neumann quantum spin measurement, see [182].

[2] An analysis of the spin-dipole oscillations based on the sum rules was presented in [146,147].

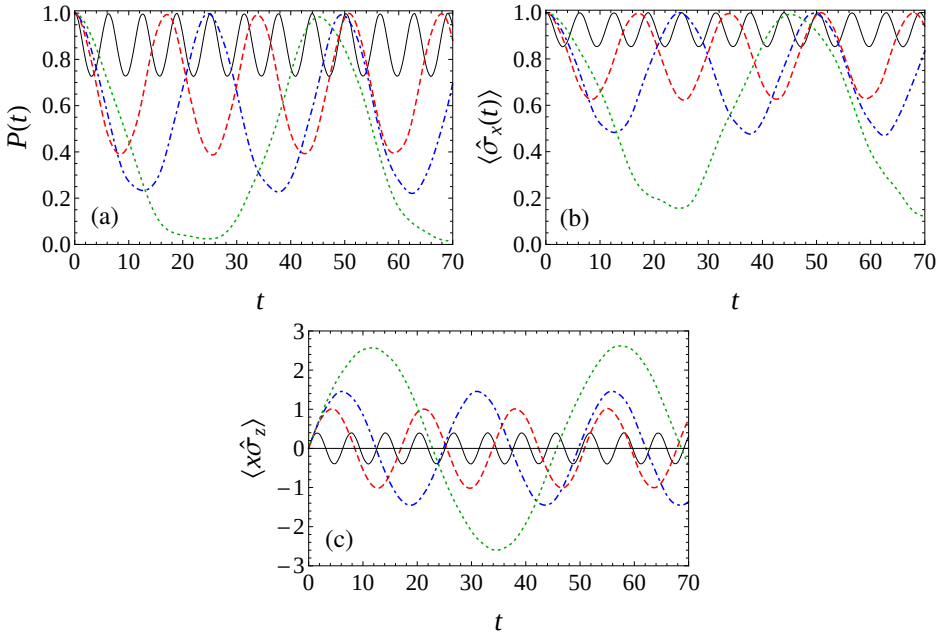

Figure 6.5: (Color online) (a) Purity, (b) spin component, and (c) spin dipole moment as a function of time for the system in the harmonic trap with $\alpha = 0.2$, $\Delta = 0$, $d_0 = 0$. The different lines correspond to $\widetilde{g}_1 N = 0$ (black solid line), $\widetilde{g}_1 N = 10$ (red dashed line), $\widetilde{g}_1 N = 20$ (blue dot-dashed line), and $\widetilde{g}_1 N = 60$ (green dotted line).

where $\Omega_R = \alpha d_0 \Delta$ is the Rabi frequency. The corresponding spin-flip time $T_{\rm sf}$ is

$$T_{\rm sf} = \frac{\pi}{\Omega_R}. \tag{6.36}$$

Figure 6.6 shows the time dependence of the purity and the spin of the condensate for given α, d_0, and Δ at different interatomic interactions. In Figure 6.6(a) one can see that the increase of $\widetilde{g}_1 N$ enhances the variation of the purity (cf. Fig 6.5(a)). This variation prevents a precise manipulation of the spin-qubit state in the condensate [3]. It follows from Figure 6.6(b) that although increasing the interaction strongly modifies the spin dynamics, it roughly conserves the spin-flip time $T_{\rm sf} = 50\pi$, see (6.36). To demonstrate the role of the SOC coupling strength α and interatomic interaction at nominally the same Rabi frequency Ω_R, we calculated the spin dynamics presented in Figure 6.7. By comparing Figures 6.6 and 6.7(a),(b) we conclude that the increase in the SOC, at the same Rabi frequency, causes an increase in the variation of the purity and of the spin component. These

[3] This low precision of the spin control can be seen as a general feature of the systems where external perturbation strongly drives the orbital motion. See, e.g. [183].

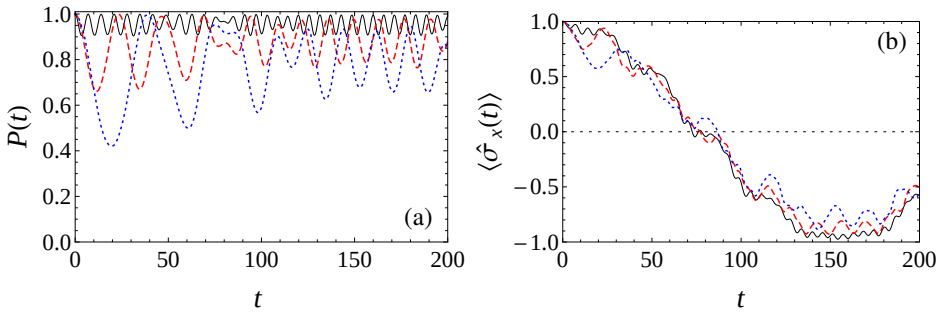

Figure 6.6: (*a*) Purity and (*b*) spin component as a function of time for a driven condensate with $\alpha = 0.1$, $\Delta = 0.1$, $d_0 = 2$. The lines correspond to $\widetilde{g}_1 N = 0$ (black solid line), $\widetilde{g}_1 N = 10$ (red dashed line), and $\widetilde{g}_1 N = 20$ (blue dot-dashed line).

results show that to achieve a required Rabi frequency and a reliable control of the spin, it is better to increase the driving amplitude d_0 rather than the spin-orbit coupling α. The increase in the SOC strength can result in losing the spin state purity and decreasing the spin length. Figure 6.7(c) shows the irregular spin evolution of the condensate inside the Bloch sphere. In Figure 6.7(a), for $\alpha = 0.2$ and $\widetilde{g}_1 N = 20$, the purity decreases almost to zero, placing the spin close to the center of the Bloch sphere, as can be seen in figure 6.7(c). It follows from Figures 6.6(b) and 6.7(b) that in order to protect pure macroscopic spin-qubit states, the Rabi frequency should be small. Then, taking into account that the displacement of the spin-projected wave packet is of the order of $\alpha\,(\widetilde{g}_1 N)^{2/3}$ and the packet width is of the order of $(\widetilde{g}_1 N)^{1/3}$, we conclude that for $\alpha \gtrsim (\widetilde{g}_1 N)^{-1/3}$, the purity of the driven state tends to zero. As a result, the Rabi frequency for the pure state evolution is strongly limited by the interaction between the particles and cannot greatly exceed $d_0 \Delta / (\widetilde{g}_1 N)^{1/3}$.

In addition, it is interesting to note that for $\widetilde{g}_1 N \gg 1$, where the spin dipole oscillates at the frequency of the order of $(\widetilde{g}_1 N)^{-2/3}$ (as given by (6.20)), the perturbation due to the trap motion is in the high-frequency limit already at $\Delta \geq (\widetilde{g}_1 N)^{-2/3}$, having a qualitative influence on the spin dynamics [184–186].

6.3.4 Phase factors due to spin-orbit coupling

The above results show that the spin-dependent velocity in (6.31), along with the interatomic repulsion, results in decreasing the spin state purity and produces irregular spin motion inside the Bloch sphere. To reduce the effect of these anomalous velocities and to prevent the resulting fast separation (with the relative velocity of 2α) of the spin components, we compensate them by introducing coordinate-dependent phases (similar to the Bragg factors) in the wave function [187, 188]. To demonstrate the effect of these phase factors, we construct the initial spinor

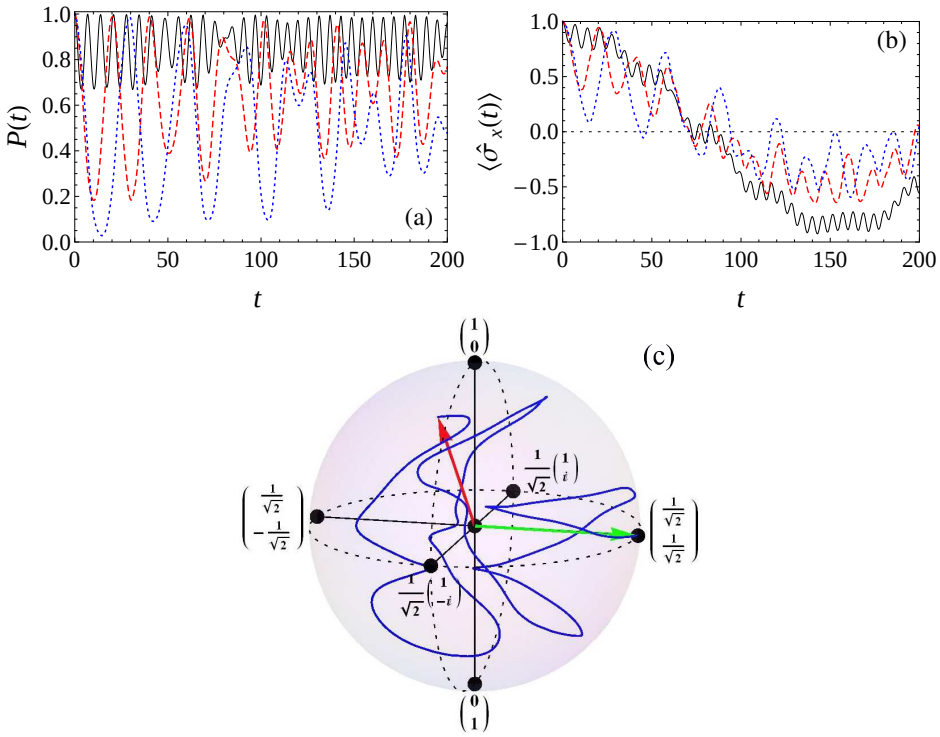

Figure 6.7: (Color online) (*a*) Purity, (*b*) spin component, and (*c*) spatial trajectory of the spin inside the Bloch sphere for the driven BEC with $\alpha = 0.2$, $\Delta = 0.1$, $d_0 = 1$ resulting in the same Rabi frequency as in Figure (6.6). In Figures (*a*) and (*b*) the lines correspond to: $\widetilde{g}_1 N = 0$ (black solid line), $\widetilde{g}_1 N = 10$ (red dashed line), and $\widetilde{g}_1 N = 20$ (blue dotted line). At $\widetilde{g}_1 N = 0$, the time dependence of $\langle \sigma_x \rangle$ is rather accurately described by $\cos(\Omega_R t)$ formula, corresponding to a relatively small variation in the purity, $1 - P(t) \ll 1$. With the increase in $\widetilde{g}_1 N$, the purity variation increases and the behavior of $\langle \sigma_x \rangle$ deviates stronger from the conventional $\cos(\Omega_R t)$ dependence. (*c*) Here the interaction is fixed to $\widetilde{g}_1 N = 20$. The green and red vectors correspond to the initial and final states of the spin, respectively. Here the final time is fixed to $t_{\rm fin} = T_{\rm sf}$, see (6.36).

$\Psi_\alpha(x,0)$ by a coordinate-dependent SU(2) rotation [161] of the state with $\langle \sigma_x \rangle = 1$ in (6.30) as

$$\Psi_\alpha(x,0) = e^{-i\alpha x \widehat{\sigma}_z} \Psi_0(x,0) = \frac{\psi_{\rm in}(x)}{\sqrt{2}} \begin{bmatrix} e^{-i\alpha x} \\ e^{i\alpha x} \end{bmatrix}. \tag{6.37}$$

The expectation value of the velocity (6.31) at each component $\psi_{\rm in}(x)\exp(\pm i\alpha x)$ is zero, and, as a result, the α-induced separation of spin components vanishes, making, as can be easily seen [161], the spinor (6.37) the stationary state of the spin-orbit coupled BEC in the Gross-Pitaevskii approximation.

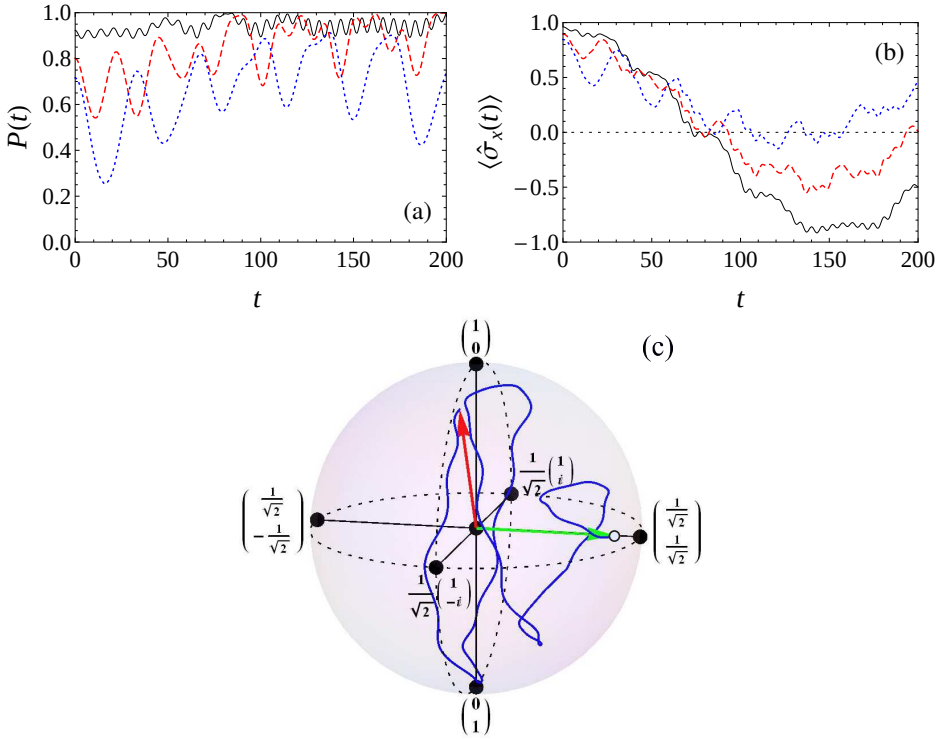

Figure 6.8: (Color online) (*a*) Purity, (*b*) spin component, and (*c*) trajectory of the spin inside the Bloch sphere for a driven BEC with initial phases as in (6.37) and $\alpha = 0.2$, $\Delta = 0.1$, $d_0 = 1$. In Figures (*a*) and (*b*) the black solid line is for $\widetilde{g}_1 N = 0$, the red dashed line is for $\widetilde{g}_1 N = 10$, and the blue dotted line is for $\widetilde{g}_1 N = 20$. In Figure (*c*) the interaction is $\widetilde{g}_1 N = 20$. The green and red vectors correspond to the initial and final states of the spin, respectively ($t_{\rm fin} = T_{\rm sf}$). The initial spin state (a solid-line circle with white filling) is inside the Bloch sphere since $\langle \sigma_x(t=0)\rangle = \sqrt{P(0)}$, and $P(0) < 1$ due to the mixed character in the spin subspace of the state in (6.37).

In terms of the spin density matrix (6.24), the state (6.37) is mixed. For a Gaussian condensate with the width w, we get the following expression for the purity at $t = 0$

$$P_{\alpha}^{[\mathrm{G}]}(0) = \exp\left[-2\,(\alpha w)^2\right]. \tag{6.38}$$

Instead, in the case of a Thomas-Fermi wave function as in (6.8), in the limit $\alpha w_{\rm TF} \gg 1$ the initial purity behaves as

$$P_{\alpha}^{[\mathrm{TF}]}(0) \sim \frac{\cos^2(2\alpha w_{\rm TF})}{(\alpha w_{\rm TF})^4}. \tag{6.39}$$

Both cases are characterized by a rapid decrease as $\alpha w_{\rm TF}$ is increased [4].

In the absence of external driving, the spin components and purity of (6.37) state remain constant. With the driving, spinor components evolve with time and the observables show evolution quantitatively different from that presented in Figure 6.7. In Figure 6.8 we show the analog of Figure 6.7 for the initial state in (6.37), with $\psi_{\rm in}(x) = \psi_0(x)$ given by (6.2)-(6.5). By comparing these Figures one can see that the inclusion of the spin-dependent phases in (6.37) strongly reduces the oscillations in the $x-$component of the spin, making the spin trajectory more regular and decreasing the variations in the purity $P(t)$ compared to the initial state without these phase factors.

A general effect of the interatomic interaction can be seen in both Figures 6.7 and 6.8. Namely, for smaller interactions $\widetilde{g}_1 N$, the destructive role of the interatomic repulsion on the spin state purity is reduced and the spin dynamics becomes more regular. As a result, at smaller $\widetilde{g}_1 N$ the spin trajectory is located closer to the Bloch sphere.

As a conclusion of this Chapter, to preserve the evolution within a high-purity spin-qubit state, with the spin being always close to the Bloch sphere, the spin-orbit coupling should be weak and, due to this weakness, the spin-rotation Rabi frequency should be small and spin rotation should take a long time. The destructive effect of both the spin-orbit coupling and interatomic repulsion on the purity of the spin state can be controllably and considerably reduced, although not completely removed, by introducing spin-dependent Bragg-like phase factors in the initial spinor wave function.

[4] It is interesting to mention that an increase in spin-orbit coupling strength after a certain value leads to a less efficient spin driving as shown with perturbation theory approach by [181].

Chapter 7

Spin dynamics of Bose-Einstein condensate in a random potential

In this Chapter we consider motion of spin-orbit coupled condensates in a random potential. We demonstrate two types of random spin dynamics: precessional, due to the displacement of the entire wavepacket and "anomalous", arising due to the spin-dependent velocity forming the distribution of spin polarization inside the condensate. We consider different stages of the wavepacket evolution to see how they modify the spin dynamics. The expansion of the condensate is accompanied by its fragmentation, where the condensate becomes sparse - the effect perfectly seen in the spin dynamics. In addition, we demonstrate the effects of interatomic interaction on the random spin evolution.

7.1 Introduction

Disorder plays a crucial role in the spin dynamics of spin-orbit coupled systems. In the presence of spin-orbit coupling spin of a moving particle precesses with the rate proportional to the particle movement. With a disorder, randomization of the momentum leads to spin dephasing process, known as the Dyakonov-Perel mechanism of exponential in time spin relaxation. In the BEC the effects of disorder on spin dynamics are qualitatively different from those in solids. First, here one can see the effect of randomness on a single state, taking into account the role of the anomalous spin-dependent velocity. Second, one can explore experimentally different regimes of disorder. Third, one can study the effect of interatomic interactions on the BEC spin dynamics, that is impossible for electron spins dynamics in random potentials.

Usually, the researchers are interested in very long times to observe the localization in nonlinear systems [189]. In the presence of spin-orbit coupling this long-term behavior including the phase diagram was studied in Ref. [190]. Here we consider relatively short time scales, where preliminary to the localization dynamics is established. Our interest is in relatively short-term behavior due to the fact that spin polarization is sufficiently large only at relatively short times.

7.2 Hamiltonian and random potential

We consider, similar to Chapters 5 and 6, a one-dimensional spin-orbit coupled condensate of interacting atoms tightly bound in the transverse directions and subjected to a random optical field producing a disorder potential. The effective Hamiltonian is

$$\widehat{H}(t<0)=\frac{\widehat{p}^2}{2M}+\frac{M\omega_0^2}{2}x^2+U_{\rm rnd}(x)+g_1|\Psi|^2, \tag{7.1}$$

$$\widehat{H}(t>0)=\frac{\widehat{p}^2}{2M}+\alpha\widehat{\sigma}_z\widehat{p}+U_{\rm rnd}(x)+g_1|\Psi|^2, \tag{7.2}$$

where, as in previous Chapters, $\Psi(x,t)\equiv[\psi_\uparrow(x,t),\psi_\downarrow(x,t)]^T$ normalized to the number of particles N. Here all units and dimensionless parameters are the same as in the Chapter 6 with length $a_{\rm ho}=\sqrt{1/M\omega_0}$ and velocity $v_{\rm ho}=\sqrt{\omega_0/M}$.

The random potential $U_{\rm rnd}(x)$ produced by distribution of "impurities" with random positions x_j and the mean concentration $n_{\rm im}$ has the form

$$U_{\rm rnd}(x)=U_0\sum_j s\left(j\right)f\left(x-x_j\right). \tag{7.3}$$

Here $s\left(j\right)$ is a random function of j with the values ±1, and $\langle s\left(j\right)\rangle=0$. As a result, $\langle U_{\rm rnd}(x)\rangle=0$. As the single impurity potential we take $f(z)=\exp\left(-z^2/w_{\rm im}^2\right)$ and assume white-noise distribution of impurities resulted in [1]:

$$\langle U_{\rm rnd}(x')U_{\rm rnd}(x'')\rangle=\left\langle U_{\rm rnd}^2\right\rangle\exp\left[-\frac{(x'-x'')^2}{2w_{\rm im}^2}\right], \tag{7.4}$$

[1] For the averaging technique, see: A.L. Efros and B.I. Shklovskii, Electronic Properties of Doped Semiconductors (Springer, Heidelberg, 1989).

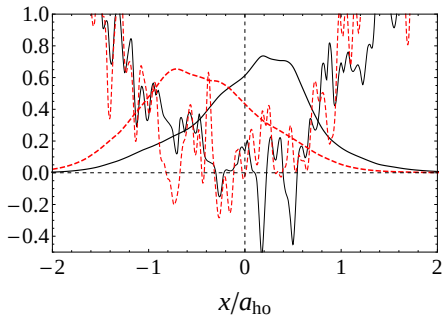

Figure 7.1: Two realization of the noninteracting BEC ground state and corresponding effective potentials in the sum of the parabolic and random potentials (scaled with factor 0.2). Here and in what follows we use numerical parameters $U_0 = \omega_0$, $w_{\rm im} = a_{\rm ho}/32$, and $n_{\rm im} = 80/a_{\rm ho}$, resulting in $\tau\omega_0 \approx 4$ (see Eq. (7.5)).

where the variation $\langle U^2_{\rm rnd}\rangle = U_0^2 n_{\rm im} w_{\rm im}\sqrt{\pi/2}$. Corresponding momentum relaxation time and localization length in the narrow potential limit ($a_{\rm ho} \gg w_{\rm im}$) are given by:

$$\frac{1}{\tau} = \frac{\pi}{v_{\rm ho}} n_{\rm im} U_0^2 w_{\rm im}^2, \qquad \ell = v_\varepsilon \tau = \frac{1}{\pi}\frac{v_{\rm ho}^2}{n_{\rm im} U_0^2 w_{\rm im}^2}. \tag{7.5}$$

We will consider relatively weak disorder, where the initial wave packet can spread, that is $\ell \gg a_{\rm ho}$. We take as the initial condition the ground state in the Hamiltonian $\widehat{H}(t<0)$ with

$$\Psi(x, t=0) = \psi_0(x)[1,1]^T/\sqrt{2}, \tag{7.6}$$

where $\psi_0(x)$ is the ground state wave function in the absence of spin-orbit coupling. Two realizations of $\psi_0(x)$ for corresponding random potentials are shown in Fig. 7.1.

To study the dynamics, we introduce a random force F_Ψ acting on the condensate, defined as the derivative of the potential energy with respect to small "rigid" displacement as $\Psi(x,t) \to \Psi(x+\delta x, t)$. For a given realization of $U_{\rm rnd}(x)$ one obtains

$$F_\Psi = -\frac{1}{N}\int_{-\infty}^{\infty} U_{\rm rnd}(x)\partial_x |\Psi(x,t)|^2 dx. \tag{7.7}$$

In the limit $w_{\rm im} \ll a_{\rm ho}$ the disorder-averaged variation can be presented as:

$$\langle F_\Psi^2\rangle = \frac{4\pi}{N^2} U_0^2 n_{\rm im} w_{\rm im}^2 \int \left(\partial_x |\Psi(x,t)|^2\right)^2 dx. \tag{7.8}$$

7.3 Condensate parameters and spin dynamics

We concentrate on three density-based quantities describing orbital motion: expectation value of coordinate $\langle x\rangle$, and two shape-related parameters such as the

packet width W and the normalized participation ratio ζ defined as:

$$W(t) = \sqrt{\left\langle (x - \langle x \rangle)^2 \right\rangle}, \qquad \zeta(t) = \left(\frac{\sqrt{2\pi}}{N^2} \int_{-\infty}^{\infty} |\Psi|^4 \, dx \right)^{-1}, \tag{7.9}$$

correspondingly. Here we consider the case where the effect of spin-orbit coupling on the gross quantities $W(t)$ and $\zeta(t)$ is relatively weak and spin-orbit coupling serves mainly as a tool to study the real-space evolution. From Eq. (7.8) and second Eq. (7.9) the random force is estimated as $\left\langle F_\Psi^2 \right\rangle^{1/2} \sim \sqrt{n_{\rm im}} w_{\rm im} U_0 \zeta^{-3/2}(t)$. The value of $\left\langle F_\Psi^2 \right\rangle$ is strongly sensitive to the value of $\zeta(t)$ since, in contrast to the potential, the force imposed by a single impurity, is determined by the spatial derivative of the condensate density. Thus, the force rapidly decreases with the increase in $\zeta(t)$. Below we skip t-dependence for brevity.

As we have considered in Chapter 6, the spin state is fully described by the reduced density matrix $\widehat{\rho}(t)$ with the components defined by Eq. (6.24). Consequently, the system purity in the spin subspace is given by

$$P = \frac{2}{N^2} \left(\frac{N^2}{2} + 2(|\rho_{12}|^2 - \rho_{11}\rho_{22}) \right), \tag{7.10}$$

where $\rho_{12} = N \left(\langle \widehat{\sigma}_x \rangle - i \langle \widehat{\sigma}_y \rangle \right)/2$. The evolution in the off-diagonal density matrix component is given by $\rho_{12}(t) = |\rho_{12}(t)| e^{i\phi_{12}(t)}$. With the choice of the initial state in Eq. (7.6), $\rho_{11} = \rho_{22} = 1/2$, and we obtain $P(t) = 4|\rho_{12}|^2/N^2$. If $|\rho_{12}| = N/2$ is conserved, the purity remains $P = 1$, and the spin dynamics is reduced to spin precession determined by the phase $\phi_{12}(t)$ as $\langle \sigma_x \rangle = \cos\phi_{12}$ and $\langle \sigma_y \rangle = -\sin\phi_{12}$. However, as we found in Chapter 6, spin-orbit coupling leads, in addition to the spin precession, to the reduced $|\rho_{12}|$, decreasing the purity of the spin state and modifying the spin dynamics. This reduction allows one to match the orbital and spin dynamics, and see the orbital motion via the spin measurement.

To describe the effect of disorder on the spin motion, one needs two contributions to the spin dynamics, which we will denote as "precessional" and "anomalous". Spin precessional mechanism, which appears due to the wavepacket displacement and resulting phase $\phi_{12}(t)$, is characterized by the spin precession length $L_{\rm so} = 1/M\alpha$ and the spin precession angle $\langle x \rangle / L_{\rm so}$. The "anomalous" mechanism is related to ρ_{12}, and appears since in the presence of spin-orbit coupling the velocity operator acquires the spin-dependent term (as in Eq. (5.8))

$$\widehat{v} = \frac{\widehat{p}}{M} + \alpha \widehat{\sigma}_z. \tag{7.11}$$

The spin-dependent velocity and spin precession play different role at different stages of the wavepacket motion, as we will show below.

7.4 Results and discussions

Since the initial spin in Eq. (7.6) is parallel to the x-axis, the expectation value of the velocity vanishes, $\langle \widehat{v} \rangle = 0$, the expectation value $\langle \widehat{\sigma}_z(t) \rangle = 0$ is conserved,

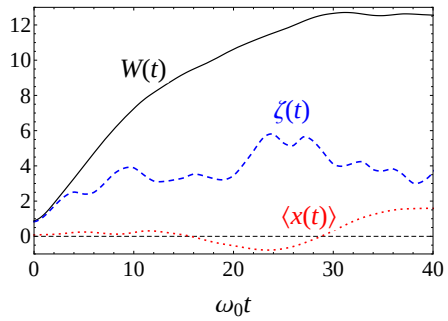

Figure 7.2: Dynamics of the noninteracting BEC parameters marked near the lines. The dependence of these parameters on spin orbit coupling here is very weak. The picture shows the fragmentation of the wave packet, where $W(t)$ becomes larger than $\zeta(t)$.

and $P(t) = \langle\widehat{\sigma}_x\rangle^2 + \langle\widehat{\sigma}_y\rangle^2$. Here the entire spin evolution is related to ρ_{12}. From definition of ρ_{12} (see Eq. (6.24) in Chapter 6) follows that the spin dynamics is strongly sensitive on the structure of the condensate in terms of the difference between $\psi_\uparrow(x, y)$ and $\psi_\downarrow(x, t)$ components.

In Figure 7.2 we present the time dependence of the BEC parameters obtained by numerical solution of the Schrödinger equation for Hamiltonian (7.2). Next, we discuss this picture and match it with the corresponding spin dynamics.

At $t = 0$ the condensate in the ground state is displaced by the random field from the center of the harmonic potential. This displacement is characterized by expectation value $\langle x(0)\rangle \sim \left\langle F^2\right\rangle^{1/2}/M\omega_0^2 \sim a_{\rm ho}\sqrt{a_{\rm ho}}/\sqrt{\ell}$. At the first stage after collapsing the harmonic potential, the condensate starts to move due to the random force in the direction of $\langle x(0)\rangle$. The spin precession angle becomes $\phi_{12}(t) = 2(\langle x(t)\rangle - \langle x(0)\rangle)/L_{\rm so}$. The behavior of $\langle\sigma_y\rangle = -\omega_0^2 t^2\,\langle x(0)\rangle\,/L_{\rm so}$ is due to the spin precession. The time dependence of $\langle\sigma_x\rangle = \sqrt{P - \langle\sigma_y\rangle^2}$ has a different origin. In the purely precessional mechanism with $P = 1$ one expects $\langle\sigma_x\rangle = \sqrt{1 - \langle\sigma_y\rangle^2}$, and, therefore, a very smooth quartic $\sim t^4$ behavior. However, here the time dependence of $P(t)$ plays an important role. At small t the components of the wave function behave as (similar to Eq. (4.17) in Chapter 4):

$$\psi_{\uparrow,\downarrow}(x, t) = \psi_0(x \mp \alpha t, 0). \tag{7.12}$$

As a result, it can be shown that the purity decreases parabolically as $1 - M\alpha^2 E_{\rm kin} t^2$, where $E_{\rm kin} \approx \omega_0/4$ is the initial kinetic energy of the condensate. In addition, the condensate starts to spread due to the quantum mechanical Heisenberg uncertainty. As a result of this spread the force and the acceleration $d^2\langle x(t)\rangle/dt^2$ rapidly decrease. Thus, time dependence of spin allows tracing the displacement and, therefore, to track the main features of the random potential. The behavior of $\langle\sigma_x(t)\rangle$ at this stage is always due to the separation $\psi_\uparrow(x, t)$

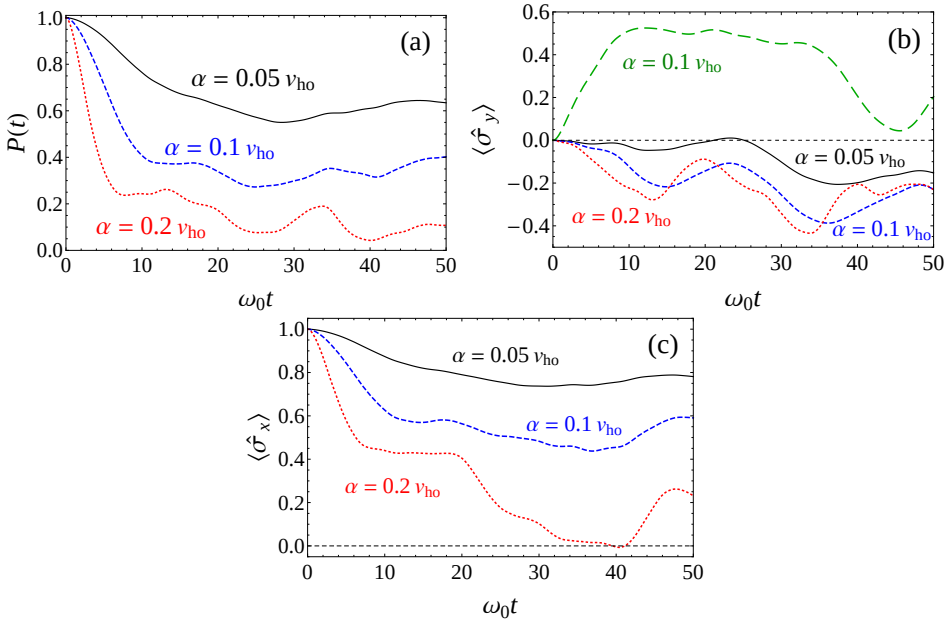

Figure 7.3: (a) Purity of the spin state, (b) and (c) corresponding time dependence spin components of the condensate for different values of α presented near the lines. The upper curve in (b) is for the realization of random potential in Fig. 7.1 with $\langle x(0)\rangle < 0$. This behaviors of $\langle\sigma_y\rangle$ is initially due to the spin precession. Here $\widetilde{g}_1 = 0$.

and $\psi_\downarrow(x,t)$, demonstrating that two mechanisms of spin dynamics are at work simultaneously. On the time scale of wavepacket broadening ($t\omega_0 \sim 1$), the effect of precession angle $(1-\cos\phi_{12})$ is of the order of $a_{\rm ho}^2/L_{\rm so}^2 \times a_{\rm ho}/\ell$, while the change in the purity is of the order of $\alpha^2/v_{\rm so}^2$. Comparison of these two expressions shows that the effect of components separation is larger than the effect of spin precession by a factor of $(1-P(\omega_0^{-1}))/\phi_{12}^2 \sim \ell/a_{\rm ho}$. As a result, in the weak disorder regime, evolution of the x-component is due to change in the purity, while the y-component evolves due to the spin precession. The behavior of the purity and spin components is shown in the Figure 7.3.

At the second stage, the fragmentation of the condensate in the random potential starts and ζ becomes less than the width W as can be seen in Fig. 7.2. The fragmentation begins at time t of the order of τ. The density distribution becomes relatively sparse, that is presented by several peaks of different width (in agreement with the result of Ref. [189]), rather than by a single peak. The number of strongest peaks can be estimated as W/ζ. The local structure of the potential plays here an important role. At this stage, the purity is related to the details of the wave function components. The $P(t)$ shows a crossover to the oscillating plateau at time satisfying condition $2\alpha t \sim \zeta(t)$. If $2\alpha\tau \le a_{\rm ho}$, then the purity does

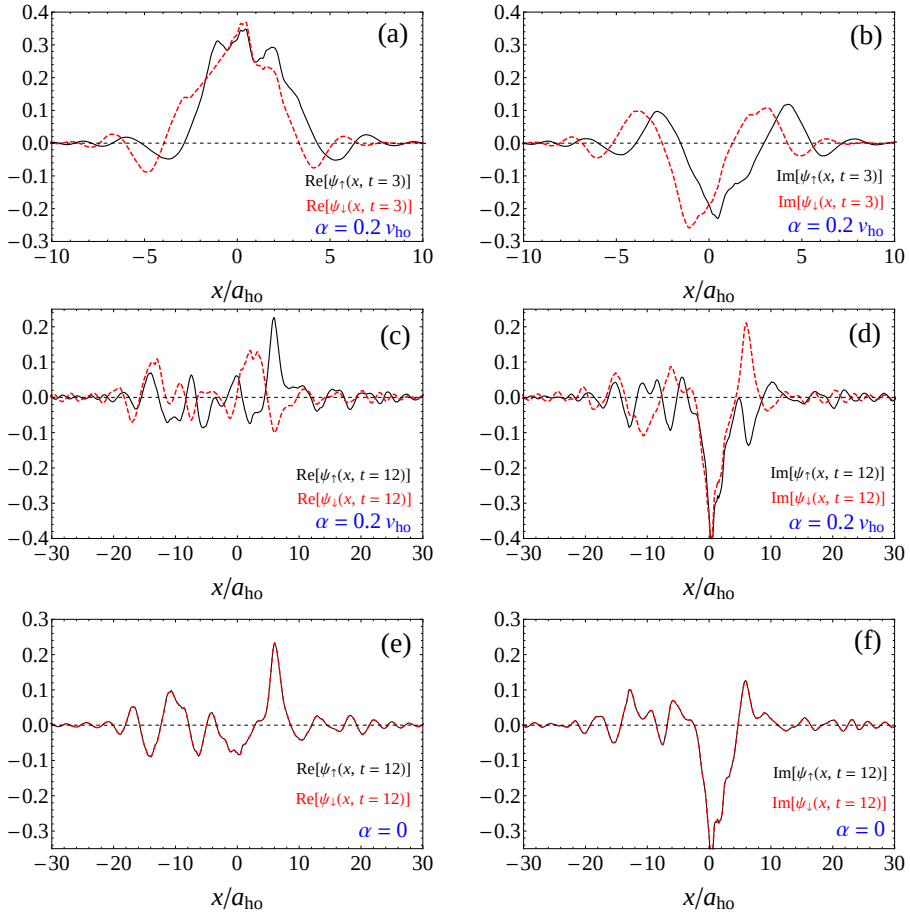

Figure 7.4: Wavefunctions $\psi_\uparrow(x,t)$ and $\psi_\downarrow(x,t)$ at different times and α. Plots (a) and (b) correspond to relatively short time, where condensate is not yet fragmented and functions are very similar. Wavefunctions (c) and (d) after the fragmentation are considerably different while in the absence of spin-orbit coupling (e) and (f) demonstrated the same behavior.

not decrease to zero and the spin $\left(\langle\sigma_x\rangle^2+\langle\sigma_y\rangle^2\right)^{1/2}$ remains finite and approximately a constant. The oscillations clearly correlate with the expectation value of $\langle x\rangle$ changing in time due to a non-vanishing force $\left\langle F_\Psi^2\right\rangle^{1/2}$. Indeed the packet still moves as the whole, $\langle x\rangle$ changes, and the spin precesses with $\langle\sigma_y\rangle\sim\langle x\rangle/L_{\rm so}$ as can be seen in the corresponding time dependence.

Now we address the effect of moderately strong repulsive interaction with $\widetilde{g}_1 N\sim 1$, where dimensionless $\widetilde{g}_1$ is defined as in Chapter 6. Repulsion between the bosons increases both the initial packet width and the value of ζ. This interaction-induced broadening decreases the effect of fluctuations in the disorder potential

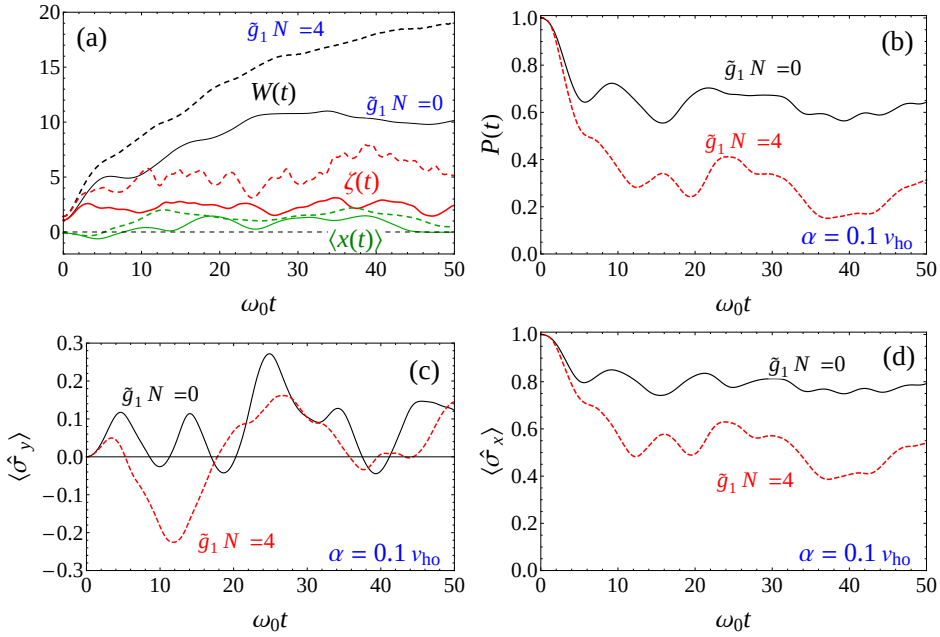

Figure 7.5: (a) BEC parameters, (b) purity of the spin state and (c), (d) spin components in the presence and absence of interactions, as marked near the plots.

and the force acting on the condensate. The repulsion makes the packet spread, and the purity decrease faster (similar to Figure 6.4 in Chapter 6). Repulsion between spin-projected components of the wavepacket decreases the purity since it reduces $|\rho_{12}|$. The calculated behavior of the purity and spin presented in the Fig. 7.5 agrees with these arguments. As a result, the effect of disorder in the spin dynamics weakens.

As a conclusion of this Chapter: we have investigated spin dynamics of spin-orbit coupled condensates in a random potential. Ground state of the condensate is displaced from origin of the harmonic trap depending on realization of the randomness, where spin precession depends on the initial displacement. The evolution of the condensate can be described by analyzing the spin dynamics, which depends on the details of wave function, rather than on the density of the condensate.

Conclusions

In this Thesis we have presented theoretical studies of various types of Bose-Einstein condensates (BECs) in $D = 1$, $D = 2$, and $D = 3$ dimensions. For three-dimensional condensates we considered thermodynamics and magnetic properties of triplons (spin $S_z = -1$ excitation) and existence of quasiequilibrium states of Bose atoms in optical lattices. For two-dimensional case, we studied collapse of spin-orbit coupled condensates. For one-dimensional condensates, we explored interference and spin dynamics - in harmonic and random potentials in the presence of spin-orbit coupling. The main results can be summarized as follows:

- **Macroscopic properties of triplons in quantum magnets**
  - The quantum anomalous density has an important qualitative effect on the specific heat and magnetic susceptibility of these systems.
  - The qualitative results related to the instabilities arising in the condensate, when the external magnetic field exceeds the corresponding critical value, are seen as the divergence in the magnetic susceptibility and changes in the Bogoliubov mode.
  - In this supercritical regime the speed of sound acquires an imaginary part and the dependence of its real part on the external field becomes almost flat.
- **The effects of disorder in dimerized quantum magnets**
  - Two existing mean field approximations have been reformulated and applied for the "dirty boson" problem to study properties of $Tl_{1-x}K_xCuCl_3$ quantum magnets.
  - These approaches qualitatively explain the magnetization data if a certain modification of the model parameters similar to the virtual crystal approximation usually applied to electron spectrum of alloys is taken into account.
  - Even when the system becomes considerably disordered, the Bose-Einstein condensation does not support formation of the pure Bose glass phase.

  - The randomness leads to a nontrivial behavior of the sound-like mode speed when external field H_{ext} is fixed and the disorder parameter x is experimentally varied. The speed increases for small x, reaches a maximum value and then decreases.

- **Quasiequilibrium itinerant and localized bosons**

  - Optical lattice characterized by the tunneling J and on-site repulsion U parameters is considered. These energies are related to the corresponding typical times of atomic motion.
  - The time $t_{\text{osc}} = 1/z_0 J$ (z_0 is the number of the nearest-neighbor lattice sites) is oscillation time of an atom in a potential well of the lattice site and the wandering time is $t_{\text{wan}} = 1/U$, characterizing interaction-related jumps between the neighboring lattice sites.
  - The quasiequilibrium coexistence of localized and itinerant Bose atoms is possible under condition $t_{\text{osc}}/t_{\text{wan}} > 2.75$.

- **Collapse of spin-orbit coupled BECs**

  - The anomalous spin-dependent velocity determined by the spin-orbit coupling can prevent collapse of a quasi two-dimensional BEC.
  - For the Rashba coupling with the spectrum axially symmetric in the momentum space, this velocity leads to a centrifugal component in the two-dimensional density flux.
  - If this flux is sufficiently strong to overcome the effect of interatomic attraction, spin-orbit coupling prevents collapse of the two-dimensional BEC.
  - In the case of effectively one-dimensional balanced Rashba-Dresselhaus couplings, the anomalous velocity splits the initial state into spin-polarized wave packets and thus decreases the interatomic attraction. The pattern of collapse for this regime is established.

- **Interference of spin-orbit coupled BECs**

  - The superposition of two freely moving spin-orbit coupled condensates gives rise to interference effects strongly dependent on their spin states at the collision time.
  - The interference - characterizing both the density and the flux - is strong when the spin states of the two condensates are parallel, and it disappears when the spin states are orthogonal.
  - The system can exhibit a spin-dependent quantum backflow behavior, which is relatively robust against synthetic spin-orbit coupling and magnetic field.
  - The ability to control the interference by synthetic spin-orbit coupling and magnetic field can be useful for investigating the quantum properties of atomic condensates and for the interference

of macroscopic spin-orbit coupled BEC-based qubits for quantum information applications.

- **Macroscopic spin qubit in spin-orbit coupled BECs**
  - The dynamics of freely expanding and harmonically driven macroscopic spin-qubits based on spin-orbit coupled BECs in a synthetic Zeeman field strongly depends on the interaction between the bosons.
  - The effects of the repulsion can be interpreted in terms of the increase in the spatial width of the condensate and the corresponding decrease in the spin dipole oscillation frequency with the interaction strength.
  - The joint influence of the repulsion and spin-orbit coupling can spatially separate and modify the spin components much stronger than just the spin-orbit coupling and results in stronger irregularities in the spin dynamics.
  - To preserve the evolution in a pure spin-qubit state, with the spin being always on or close to the Bloch sphere, the spin-orbit coupling should be weak and, due to this weakness, the evolution should take a long time.
  - The destructive effect of the spin-orbit coupling on the purity of the spin state can be controlled by introducing spin-dependent Bragg-like phase factors in the initial spinor wave function.
- **Spin dynamics of BECs in a random potential**
  - Motion of the condensate on a short time scale and its structure can be studied based on time dependence of the condensate spin.
  - Two mechanisms of spin dynamics taking place simultaneously can be clearly seen here: a precessional, related to the time-dependent phase difference between the spinor components and an "anomalous" one due to the change in the spatial overlap of the spinor components.
  - The strong interatomic interaction makes the dynamics only weakly disorder-dependent.

Resumen

El condensado de Bose-Einstein (CBE) es uno de los primeros fenómenos predichos por la física cuántica macroscópica. El aspecto más notable de este efecto es la condensación en el espacio de momentos y no en el de coordenadas. A la temperatura de transición las partículas empiezan gradualmente a condensarse en el estado de momento cero. En ausencia de interacciones interatómicas a temperatura $T = 0$ todas las partículas tienen momento cero. La primera aplicación excelente de ésta teoría fue en Helio líquido, lo que demostró excitaciones similares a las de Bogoliubov y la superfluided. En los 60 la idea de los CBE fue aplicada a excitones producidos ópticamente en sólidos. Los intentos de encontrar nuevos tipos de condensados atómicos continuaron ya que se consideraba de gran interés ver condensados de otros tipos de átomos, lo que solo sería posible a temperaturas extremadamente bajas, donde los efectos cuánticos dominan la física del sistema. Esto fue conseguido mediante técnicas de enfriamiento con láser, y en 1995 tres grupos de investigación informaron de CBEs de átomos alcalinos: E. Cornell y C. Wieman (de JILA), W. Ketterle (del MIT) y R. Hulet (de la universidad de Rice). Estos importantes resultados dieron acceso a los investigadores a sistemas cuánticos macroscópicos con propiedades controlables, incluyendo el control de interacciones interatómicas. Un campo en rápido desarrollo de gran interés para experimentales y teóricos fue creado en la física. La forma de pensar de una nueva generación de físicos fue fuertemente modificada debido a la observación de nuevos fenómenos cuánticos a escala macroscópica como la habilidad de controlar la distribución de partículas en el espacio de momentos, interferencia macroscópica, fascinantes propiedades no lineales y muchas otras.

El fenómeno de los CBEs es muy amplio y trae constantemente nuevos resultados para sistemas nuevos. El descubrimiento de CBEs de quasipartículas tales como magnones en fuerte desequilibrio (o “triplones” en equilibrio) en imanes cuánticos y clásicos y de polaritones ópticos en microcavidades cuánticas son éxitos recientes. Los condensados atómicos ópticamente producidos pueden ser puestos en redes ópticas, explorando así nuevos campos relacionados con la física del estado sólido. Muy recientemente fue descubierto que aunque los átomos sean bosones pueden ser caracterizados por un pseudoespín 1/2 ópticamente producido. Este pseudoespín puede ser acoplado al momento del átomo, llevando a la realización de gases de átomos fríos y CBEs con acoplamiento espín-órbita (AEO). Estos novedosos tipos de CBEs son estudiados en esta tesis.

La tesis consiste de cuatro partes en las que se discuten diferentes temas. La primera parte (capítulos 1 y 2) está dedicada a CBEs de triplones en imanes cuánticos. En el primer capítulo presentamos las propiedades macroscópicas del sistema. Bajo la aproximación Hartree-Fock-Bogoliubov estudiamos la velocidad del sonido, calor específico y la susceptibilidad magnética. Aquí demostramos la importancia cualitativa de los promedios anómalos, lo que nos permite explicar los resultados experimentales disponibles y predecir nuevos tales como la inestabilidad de campo alto de los CBEs. En el segundo capítulo desarrollamos una teoría sobre el efecto del desorden en los CBEs de triplones tomando como prototipo de estudio la solución ampliamente investigada $Tl_{1-x}K_xCuCl_3$. Consideramos fases inducidas por el desorden y demostramos que, además de los efectos del desorden, una renormalización de los parámetros del material debería ser hecha para concordar con los experimentos. La segunda parte (capítulo 3) trata de bosones fríos en redes ópticas. En este capítulo analizamos la coexistencia de átomos localizados y delocalizados en redes ópticas con un factor entero de relleno a temperatura cero. Demostramos que esta coexistencia sólo es posible en un régimen de cuasi-equilibrio y buscamos condiciones para la realización de tal coexistencia. En la tercera parte (capítulo 4) consideramos CBEs de dos dimensiones. En el capítulo 4 abordamos el sistema de átomos atractivos en el régimen de resonancia de Feshbach y estudiamos la dinámica y el posible colapso de un cuasi-CBE con AEO bidimensional. Consideramos dos realizaciones diferentes del AEO tales como del tipo Rashba y del tipo de Rashba-Dresselhaus equilibrado y demostramos cómo el colapso depende del tipo de acoplamiento. La presentación de la cuarta parte (capítulos 5-7) está relacionada con la realización de CBEs de una dimensión. En el quinto capítulo nos centramos en el rol del campo magnético sintético en la interferencia macroscópica de los CBE con AEO de una dimensión. Exploramos diferentes regímenes de la interferencia y encontramos que los campos magnéticos sintéticos del tipo Zeeman pueden cambiar significativamente el patrón de interferencia. En el capítulo 6 consideramos la dinámica guiada de un qubit espín macroscópico basado en un CBE y demostramos que la velocidad anómala, que aparece debido al AEO, lleva a consecuencias no triviales en la capacidad de manipulación coherente de espines. Además las interacciones interatómicas tienen un papel importante en la dinámica del espín. En el capítulo 7 consideramos la evolución del espín del condensado en un potencial aleatorio y estudiamos la relajación del espín inducida por el desorden. Demostramos que el CBE en un potencial desordenado puede tener mecanismos de relajación de espín, los cuales no pueden ser observados en sólidos, donde han sido un tema de gran interés durante décadas. Al final, presentamos unas extensas conclusiones. Los principales resultados presentados en la tesis pueden ser resumidos como sigue:

- **Propiedades macroscópicas de los triplones en imanes cuánticos.**

Al ser bosones con espín $S = 1$, las cuasi-partículas características en aislantes magnéticos pueden transformarse en CBEs. El ejemplo mas interesante es el de los triplones, que aparecen si el hueco en el espectro de excitaciones del triplete separándolo de el del singlete del estado fundamental puede ser cerrado por el efecto Zeeman del campo magnético. El campo divide las excitaciones del espín en tres ramas con $S_z = 0, \pm 1$. Cuando el desplazamiento de Zeeman de la rama

$S_z = -1$ excede el hueco inicial en el espectro, una población finita de triplones, la cual puede ser considerada como la reconstrucción del estado fundamental, es formada. En campos relativamente débiles, donde la concentración de triplones es pequeña, se puede hacer una teoría en términos de un gas de Bose débilmente interactivo de un CBE de triplones. La observación de un modo espín-volteado del tipo Bogoliubov, la huella dactilar de un CBE en un gas de Bose interactivo, es posible siempre y cuando tengamos el fuerte apoyo de este CBE de triplones. La teoría está normalmente basada en la aproximación de Hartree-Fock-Popov (HFP), despreciando los términos anómalos de densidad. La desventaja de esta aproximación es la predicción de una densidad de triplón discontinua, a lo largo de la transición. Aunque esta aproximación nos da una buena explicación cuantitativa del calor específico C_v, no está claro si cualitativamente captura toda la física relevante. Por esta razón es interesante estudiar el comportamiento de un CBE de triplones usando una aproximación más precisa para ver si el análisis más allá de la aproximación HFP revela nuevos aspectos. La aproximación de campo medio mejora considerablemente la situación teniendo en cuenta términos anómalos de densidad en el condensado. La clave de esta aproximación está en encontrar la velocidad de excitaciones del tipo Bogoliubov. La aproximación Hatree-Fock-Bogoliubov desarrollada aquí nos lleva a una densidad continua en concordancia con el experimento. Aplicando esta aproximación al CBE de triplones demostramos que cuando el campo magnético externo $H_{\rm ext}$ excede el valor crítico, $H_{\rm ext}^{\rm cr}$, la velocidad del sonido se vuelve compleja y el CBE está sometido a una inestabilidad.

Encontramos dos valores característicos de $H_{\rm ext}$. Primero, cuando los triplones forman el CBE, $H_{\rm ext}^{\rm BEC}$ y segundo, $H_{\rm ext}^{\rm cr} > H_{\rm ext}^{\rm BEC}$, cuando el CBE muestra inestabilidad dinámica. Investigamos propiedades macroscópicas del triplón condensado teniendo en cuenta la densidad anómala. Demostramos que estas medias tienen un efecto cualitativo en el calor específico de la susceptibilidad magnética. El resultado cualitativo de nuestra aproximación está relacionado con las inestabilidades dinámicas que aparecen en el condensado. Cuando el campo magnético excede el valor crítico estas inestabilidades llevan a divergencias en la susceptibilidad magnética. En este dominio, la velocidad del sonido adquiere una parte imaginaria y la dependencia de su parte real en $H_{\rm ext}$ se hace débil. Estas dos predicciones pueden ser verificadas en experimentos de susceptibilidad magnética y de dispersión de neutrones.

- **Efectos del desorden en imanes cuánticos atenuados.**

El desorden es importante en varios sistemas de partículas tales como como ^{4}He, átomos fríos en redes ópticas y cuasi-partículas tales como polaritones y excitones. Aunque estos sistemas sean adecuados para estudiarlos experimentalmente, la teoría de grupos desordenados de bosones interactivos es compleja y básicamente no existen soluciones exactas. Para abordar este problema Yukalov y Graham desarrollaron una aproximación de campo medio estocástica autoconsistente para los sistemas Bose con una repulsión interpartícula arbitrariamente fuerte y una fuerza arbitraria de desorden. Una cuestión interesante aquí concierne a la existencia de una fase en un cristal de Bose, es decir, la fase donde la fracción del condensado no es cero, mientras que la superfluided

no aparece aún.

El efecto del desorden en los imanes, que puede ser producido mezclándolo con otros elementos químicos, puede ser lo suficientemente fuerte para ser observado en propiedades físicas tal como la magnetización dependiente de la temperatura. Hasta ahora el compuesto mas investigado mostrando triplones CBE es $TlCuCl_3$. Para estudiar el efecto del desorden, soluciones sólidas como $Tl_{1-x}K_xCuCl_3$ han sido experimentalmente investigadas.

En el $Tl_{1-x}K_xCuCl_3$ la magnetización inducida exhibe un mínimo en forma de corona a una temperatura crítica $T_{\rm cr}(H_{\rm ext})$ para campos magnéticos fijados $H_{\rm ext} \geq H_{\rm ext}^{\rm cr}$ de forma similar a los compuestos primogénitos correspondientes al triplón CBE.

Hemos reformulado y aplicado dos aproximaciones de campo medio conocidas para el problema del "bosón sucio" para estudiar propiedades de imanes cuánticos aleatorios. Demostramos que estas aproximaciones pueden explicar cualitativamente los datos de magnetización si se tiene en cuenta una cierta modificación de los parámetros modelo, similar a la aproximación de cristal virtual que normalmente se aplica a propiedades de las aleaciones. La aleatoriedad en las soluciones de compuestos magnéticos manifiesta en sí misma una dualidad: (i) mediante la modificación de parámetros internos y (ii) mediante la localización del triplón. Éstas deberían ser tenidas en cuenta simultáneamente para una descripción adecuada de los datos experimentales. Aunque el sistema se considera desordenado, la fase del cristal de Bose no se forma. Los vínculos aleatorios dan lugar a comportamientos no triviales de la velocidad del pseudomodo: cuando se fija $H_{\rm ext}$, crece para x pequeñas, alcanza un máximo y luego decrece. Esta dependencia puede ser sistemáticamente estudiada, por ejemplo, midiendo la relación de dispersión entre el modo de Bogoliubov y la dispersión de neutrones.

- **Cuasi-equilibrio de bosones itinerantes y localizados.**

Aquí consideramos N átomos en una red óptica de N_L posiciones en desequilibrio, con el factor de relleno $\nu \equiv N/N_L$. El proceso de cargado en desequilibrio dura $t_{\rm non}$, más tiempo que el tiempo de equilibrio local $t_{\rm loc}$, pero menos que el tiempo de relajación $t_{\rm rel}$ necesario para que le sistema alcance el equilibrio total, que es $t_{\rm loc} \ll t_{\rm non} \ll t_{\rm rel}$. En el intervalo de tiempo $t_{\rm non} \ll t \ll t_{\rm rel}$, el sistema puede ser tratado como en cuasi-equilibrio, de tal forma que los átomos itinerantes y localizados están en equilibrio entre ellos, mientras que el sistema como un todo aún no ha sido equilibrado pero cambia lentamente.

Consideramos una red óptica caracterizada por la frecuencia de tunelamiento J y repulsión *in-situ* U. Estos parámetros de energía están relacionados con sus correspondientes tiempos típicos. La energía $z_0 J$ (z_0 es el número de vecinos próximos) define el tiempo $t_{\rm osc} = 1/z_0 J$, durante el cual un átomo oscila en un pozo de potencial de una posición de la red. Cuanto más pequeño sea $z_0 J$, más largo será este tiempo de oscilación. La energía U define el tiempo $t_U = 1/U$, el cual determina la escala de tiempo relacionada con la interacción. La condición de coexistencia es $t_{\rm osc}/t_U > 2.75$. Esto significa que el tiempo de oscilación tiene que ser lo suficientemente largo en comparación con el tiempo relacionado con la

interacción. De otra forma, los átomos no podrían ser localizados.

• **Colapso de los condensados de Bose-Einstein con acoplamiento espín-órbita.**

Los aspectos fundamentales del colapso de un condensado libre están determinados por la interacción de sus energías cinéticas positiva y negativa de atracción dependientes de el tamaño característico del condensado a. Para $D = 3$ la dependencia de la energía total en a es no monótona y el colapso para $a \to 0$ ocurre con cualquier fuerza de interacción ya que para a pequeñas domina la atracción. Para $D = 2$ las energías de interacción y cinética escalan con a^{-2} y el colapso ocurre solo para atracciones lo suficientemente fuertes. El AEO juega un papel importante en la física de los CBEs con átomos interactivos. Hemos demostrado que la velocidad dependiente del espín anómala determinada por el AEO puede evitar el colapso de un quasi-CBE no uniforme de dos dimensiones. Para el acoplamiento de Rashba con el espectro axial simétrico esta velocidad nos lleva a una componente centrífuga en el flujo de densidad de dos dimensiones. Como resultado el AEO puede evitar el colapso si este flujo es lo suficientemente fuerte para superar las atracciones interatómicas. En el caso efectivo de acoplamientos equilibrados de Rashba-Dresselhaus en una dimensión la velocidad anómala divide el estado inicial en paquetes de onda con espín polarizado, disminuye la densidad del condensado y, por la tanto, puede evitar el colapso. Nuestro método puede ser generalizado directamente para el caso intermedio, donde los acoplamientos de Dresselhaus y Rashba tienen fuerzas diferentes. Estos resultados muestran que se puede conseguir un control sobre el colapso usando AEOs experimentalmente realizables y, por tanto, extender la habilidad de estudiar varios regímenes en CBEs de partículas atractivas.

• **Interferencia de condensados de Bose-Einstein con acoplamiento espín-órbita.**

La interferencia de dos CBEs expandiéndose libremente es una manifestación cuántica macroscópica. Puede ser observado preparando los dos condensados en trampas espacialmente separadas, que después serán liberados. Después, los condensados pueden expandirse y en un momento dado se superpondrán, produciendo un patrón de interferencia. Aquí consideramos el control del tiempo de vuelo de la interferencia de dos condensados de una dimensión produciendo su estado entrelazado, lo cual podría ser necesario en información cuántica mediante AEO de Rashba-Dresselhaus equilibrado y un campo magnético sintético.

Hemos demostrado que la superposición de dos condensados con AEO moviéndose libremente tiene como resultado efectos de interferencia fuertemente dependientes en el estado del espín del condensado en el momento de la colisión. La interferencia es nítida cuando los estados de los espines de los dos condensados son paralelos, y desaparece cuando son ortogonales. Estos efectos pueden ser claramente observados en experimentos de tiempo de vuelo, y son realizables con la tecnología actual. Es más, el sistema también exhibe un flujo opuesto cuántico dependiente del espín, lo cual puede ser útil para investigar las propiedades cuánticas del condensado y para qubits macroscópicos basados en BECs aplicados

en información cuántica.

- **Qubit de espín macroscópico en un condensado Bose-Einstein con acoplamiento de espín-óribta.**

Una de las futuribles aplicaciones de los CBEs con AEO es la realización de un qubit espín macroscópico. Sus correspondientes puertas pueden ser producidas en términos del AEO y de un campo magnético sintético externo. Debido al AEO, un movimiento mecánico periódico del condensado conduce la dinámica del espín y puede causar transiciones de volteamiento del espín a la frecuencia de Rabi dependiendo del AEO. Esta técnica, similar a la resonancia eléctrica dipolo-espín, funciona para qubits basados en el espín de un solo electrón. Para los qubits espín macroscópicos de un CBE, la física es diferente en al menos dos aspectos. Primero, un efecto relativo del AEO comparado con la energía cinética puede ser mucho mas fuerte que en semiconductores. Segundo, la interacción entre los bosones puede tener un fuerte efecto en toda la dinámica de los espines.

Estudiamos la dinámica de qubits espín macroscópicos libres y dirigidos basado en cuasi-CBEs con AEO de una dimensión en un campo sintético de Zeeman. La evolución resultante depende fuertemente en el AEO de una forma no trivial y en interacciones entre los bosones. Por un lado, el AEO nos lleva a la dinámica dirigida del qubit espín. Por otro lado, nos lleva a una velocidad anómala dependiente del espín causando una división de espín del paquete de ondas inicial y reduciendo la pureza del estado de espín. Esta influencia destructiva del AEO se acentúa por la repulsión interatómica. La influencia conjunta de la repulsión y del AEO puede separar y modificar espacialmente los componentes de espín de una forma más fuerte que sólo el AEO. Sin embargo, la frecuencia de Rabi de volteo de espín se mantiene casi invariable en presencia de interacciones interatómicas ya que solo conducen a fuerzas internas y no cambian el momento del condensado. Para preservar durante la evolución un estado de alta pureza del qubit-espín, con el espín siempre cercano a la esfera de Bloch, el AEO debería ser débil y, debido a esta debilidad, la frecuencia de Rabi de rotación del espín debería ser pequeña. El efecto destructivo tanto del AEO como de la repulsión interatómica puede ser reducido de manera controlable introduciendo factores de fase dependientes del espín del tipo Bragg en la función de onda espinor inicial.

- **Dinámica de espín CBE en un potencial aleatorio.**

La presencia de espín con AEO de una partícula en movimiento muestra precesión con la tasa proporcional al momento de la partícula. En un sistema desordenado la aleatorización del momento en el tiempo nos conduce a un proceso de desfasamiento del espín, conocido como mecanismo Dyakonov-Perel de relajación de espín exponencial en un tiempo similar al movimiento de estrechamiento.

Aquí hemos investigado la dinámica del espín de un condensado con AEO en un potencial aleatorio en una escala de tiempos relativamente corta, donde el patrón real de localización es premoldeado pero no completamente realizado. Nos concentramos en un AEO relativamente débil con una influencia despreciable en las cantidades totales relacionadas con la densidad. La evolución aleatoria del valor esperado de la posición del condensado y su anchura se manifiesta claramente en

la dinámica del espín. Sin embargo, en un fuerte contraste con las características relacionadas con la densidad, la pureza en el subespacio del espín y la resultante dinámica del espín dependen de las componentes de la función de onda espinor y no tanto de la distribución de densidad del condensado. Dos mecanismos de la dinámica del espín pueden ser claramente visto aquí - (i) uno de precesión causado por la diferencia de fase entre los componentes de la función de onda espinor y (ii) y otro anómalo causado por el cambio en la superposición de los componentes del espinor. Estos dos mecanismos tienen lugar simultáneamente. El efecto de la interacción entre partículas cambia cuantitativamente todos los parámetros disminuyendo la pureza del estado de espín y modificando la dinámica de espín resultante.

Bibliography

[1] T. Matsubara and H. Matsuda, *Prog. Theor. Phys.* **16**, 569 (1956).

[2] H. Matsuda and T. Tsuneto, *ibid* **46**, 411 (1970).

[3] M. Tachiki and T. Yamada, *J. Phys. Soc. Jpn.* **28**, 1413 (1970).

[4] E.G. Batyev and S.L. Braginskii, *JETP* **60**, 781 (1984).

[5] E.G. Batyev, *ibid* **62**, 173 (1985).

[6] V. E. Demidov O. Dzyapko, S. O. Demokritov, G. A. Melkov, and A. N. Slavin, *Phys. Rev. Lett.* **100**, 047205 (2008).

[7] G.E. Volovik, *J. Low. Temp. Phys.* **153** 266 (2008).

[8] I. Affleck, *Phys.Rev* B, **43**, 3215 (1991).

[9] T. Giamarchi and A. M. Tsvelik, *Phys. Rev.* B, **59**, 11398 (1999).

[10] T. Giamarchi, C. Rüegg, and O. Tchernyshyov, *Nature Phys.* **4**, 198 (2008).

[11] T. Nikuni, M. Oshikawa, A. Oosawa, and H. Tanaka, *Phys. Rev. Lett.* **84**, 5868 (2000).

[12] A. Oosawa, H. A. Katori, and H. Tanaka, *Phys. Rev.* B, **63**, 134416, (2001).

[13] Ch. C. Rüegg, D. F. McMorrow, B. Normand, H. M. Ronnow, S. E. Sebastian, I. R. Fisher, C. D. Batista, S. N. Gvasaliya, Ch. Niedermayer, and J. Stahn, *Phys. Rev. Lett.* **98**, 017202 (2007).

[14] M. B. Stone, C. Broholm, D. H. Reich, P. Schiffer, O. Tchernyshyov, P. Vorderwisch, and N. Harrison, *New J. Phys.* **9**, 31 (2007).

[15] A. A. Aczel, Y. Kohama, M. Jaime, K. Ninios, H. B. Chan, L. Balicas, H. A. Dabkowska, and G. M. Luke, *Phys. Rev.* B, **79**, 100409(R) (2009).

[16] A. Paduan-Filho, K. A. Al-Hassanieh, P. Sengupta, and M. Jaime, *Phys. Rev. Lett.* **102**, 077204 (2009).

[17] N. Laflorencie and F. Mila, *Phys. Rev. Lett.* **102**, 060602 (2009).

[18] A. A. Tsirlin and H. Rosner, *Phys. Rev.* B, **83**, 064415 (2011).

[19] T. Dodds, B.-J. Yang, and Y. B. Kim, *Phys. Rev.* B **81**, 054412 (2010).

[20] J. Sirker, A. Weiße, and O. P. Sushkov, *Europhys. Lett.* **68**, 275 (2004).

[21] T. D. Stanescu, B. Anderson, and V. Galitski, *Phys. Rev.* A, **78**, 023616 (2008).

[22] M. A. Continentino and A. S. Ferreira, *J. Magn. Magn. Mater.* **310**, 828 (2007).

[23] E. Ya. Sherman, P. Lemmens, B. Busse, A. Oosawa, and H. Tanaka, *Phys. Rev. Lett.* **91**, 057201 (2003).

[24] A. Oosawa, K. Kakurai, T. Osakabe, M. Nakamura, M. Takeda, and H. Tanaka, *J. Phys. Soc. Jpn.* **73** 1446 (2004).

[25] Y. Kulik and O. P. Sushkov, *Phys. Rev.* B, **84**, 134418 (2011).

[26] Ch. Rüegg, N. Cavadini, A. Furrer, H.-U. Güdel, K. Krämer, H. Mutka, A. Wildes, K. Habicht, and P. Vorderwisch, *Nature* **423**, 62 (2003).

[27] A. Rakhimov, E. Ya. Sherman, and C. K. Kim *Phys. Rev.* B, **81**, 020407(R) (2010).

[28] M. Crisan I. Tifrea, D. Bodea, and I. Grosu, *Phys. Rev.* B, **72**, 184414 (2005).

[29] V. I. Yukalov, *Ann. Phys.* **323**, 461 (2008)

[30] G. Misguich and M. Oshikawa, *J. Phys. Soc. Jpn.* **73**, 3429 (2004)

[31] J. Jensen, *Phys. Rev.* B, **83**, 064420 (2011).

[32] J. Keeling, *Phys. Rev.* B, **74**, 155325 (2006).

[33] F. Yamada, T. Ono, H. Tanaka, G. Misguich, M. Oshikawa, and T. Sakakibara, *J. Phys. Soc. Jpn.* **77**, 013701 (2008).

[34] N. P. Proukakis and B. Jackson, *J. Phys. B: At. Mol. Opt. Phys.* **41**, 203002 (2008).

[35] H. Kleinert, S. Schmidt, and A. Pelster, *Ann. Phys.* (Leipzig), **14**, 214 (2005).

[36] J. O. Andersen, *Rev. Mod. Phys.* **76**, 599 (2004).

[37] V. I. Yukalov and E. P. Yukalova, *Laser Phys. Lett.* **2**, 506 (2005).

[38] H. T. C. Stoof, K. B. Gubbels, and D. B. M. Dickerscheid, *Ultracold Quantum Fields*, Springer, 2009.

[39] A. Rakhimov, Chul-Koo Kim, Sang-Hoon Kim, and Jae-Hyung Yee, *Phys. Rev.* A, **77**, 033626 (2008).

[40] W. H. Dickhoff and D. Van Neck, *Many-Body Theory Exposed*, World Scientific, 2005.

[41] A. Griffin, T. Nikuni, and E. Zaremba, *Bose-Condensed Gases at Finite Temperatures*, Cambridge University Press, 2009.

[42] L. Pitaevskii and S. Stringari, *Bose-Einstein Condensation (International Series of Monographs on Physics)*, Oxford University Press, 2003.

[43] M. Grether, M. de Llano, and G. A. Baker, *Jr., Phys. Rev. Lett.* **99**, 200406 (2007).

[44] R. Dell'Amore, A. Schilling, and K. Krämer, *Phys. Rev.* B, **79**, 014438 (2009).

[45] R. Dell'Amore, A. Schilling, and K. Krämer, *Phys. Rev.* B, **78**, 224403 (2008).

[46] K. Huang, *Statistical Mechanics*, Wiley, 1987.

[47] L. D. Landau and E. M. Lifshitz, *Statistical Physics, in: Course of Theoretical Physics*, vol. **5**, Butterworth-Heinemann Publ., 1980.

[48] V. I. Yukalov, *Phys. Rev.* E **72**, 066119 (2005).

[49] D. C. Roberts and M. Ueda, *Phys. Rev.* A, **73**, 053611 (2006).

[50] H. Tanaka, A. Oosawa, T. Kato, H. Uekusa, Y. Ohashi, K. Kakurai, and A. Hoser, *J. Phys. Soc. Jpn.* **70**, 939 (2001).

[51] C. E. Creffield, *Phys. Rev.* A, **79**, 063612 (2009).

[52] M. Modugno, C. Tozzo, and F. Dalfovo, *Phys. Rev.* A, **70**, 043625 (2004).

[53] S. Sinha and Y. Castin, *Phys. Rev.* Lett. **87**, 190402 (2001).

[54] N. Argaman and Y.B. Band, *Phys. Rev.* A, **83**, 023612 (2011).

[55] M.-C. Chung and A. B. Bhattacherjee, *New J. Phys.* **11**, 123012 (2009).

[56] D. L. Mills, *Phys. Rev. Lett.* **98**, 039701 (2007).

[57] V. M. Kalita, I. Ivanova, and V. M. Loktev, *Phys. Rev.* B, **78**, 104415 (2008).

[58] V. M. Kalita and V. M. Loktev, *JETP Lett.* **91**, 183 (2010).

[59] V. M. Kalita and V. M. Loktev, *Low Temp. Phys.* **36**, 665 (2010).

[60] A. Schilling and H. Grundmann, *Ann. Phys.* **327**, 2301 (2012).

[61] A. Schilling, H. Grundmann, and R. Dell'Amore, *J. Phys.: Conf. Ser.* **400**, 032081 (2012).

[62] G. M. Falco, A. Pelster, and R. Graham, *Phys. Rev.* A, **75**, 063619 (2007).

[63] A. V. Lopatin and V. M. Vinokur, *Phys. Rev. Lett.* **88**, 235503 (2002).

[64] S. Giorgini, L. Pitaevskii, and Stringari, *Phys. Rev.* B, **49**, 12938 (1994).

[65] C. Gaul, N. Renner, and C. A. Müller, *Phys. Rev.* A, **80**, 053620 (2009).

[66] C. Gaul and C. A. Müller, *Phys. Rev.* A, **83**, 063629 (2011).

[67] L. Zhang, *Phys. Rev.* B, **47**, 14364 (1993).

[68] R. Graham and A. Pelster, *Int. Journ. of Bifurcation and Chaos* **19**, 2745 (2009).

[69] I. A. Shelykh, A. V. Kavokin, Y. G. Rubo, T. C. H. Liew, and G. Malpuech, *Semicond. Sci. Technol.* **25**, 013001 (2010).

[70] L. V. Butov, A. C. Gossard, and D. S. Chemla, *Nature* **418**, 751 (2002).

[71] B. Shapiro, *J. Phys.* A, **45** 143001 (2012).

[72] V. I. Yukalov and R. Graham, *Phys. Rev.* A, **75**, 023619 (2007).

[73] V. I. Yukalov, E. P. Yukalova, K. V. Krutitsky, and R. Graham, *Phys. Rev.* A, **76**, 053623 (2007).

[74] K. Huang and H. F. Meng, *Phys. Rev. Lett.* **69**, 644 (1992). G. A. Melkov, A. A. Serga, B. Hillebrands, and A. N. Slavin, *Nature* **443**, 430 (2006).

[75] A. Oosawa and H. Tanaka, it Phys. Rev. B, **65**, 184437 (2002).

[76] F. Yamada, H. Tanaka, T. Ono, and H. Nojiri, *Phys. Rev.* B, **83**, 020409 (2011).

[77] H. Tanaka, Y. Shindo, and A. Oosawa, *Prog. of Theor Phys. Suppl.* **159**, 189 (2005).

[78] A. Zheludev and D. Hüvonen, *Phys. Rev.* B, **83**, 216401 (2011).

[79] F. Yamada, H. Tanaka, T. Ono, and H. Nojiri, *Phys. Rev.* B, **83**, 216402 (2011).

[80] G. E. Astrakharchik, J. Boronat, J. Casulleras, and S. Giorgini, *Phys. Rev.* A, **66**, 023603 (2002).

[81] O. Nohadani, S. Wessel, and S. Haas, *Phys. Rev. Lett.* **95**, 227201 (2005).

[82] M. P. A. Fisher, P. B. Weichman, G. Grinstein, and D. S. Fisher, *Phys. Rev.* B, **40**, 546 (1989).

[83] V. I. Yukalov, *Phys. Part. Nucl.* **42**, 460 (2011).

[84] S. Pilati, S. Giorgini, and N. Prokofev, *Phys. Rev. Lett.* **102**, 150402 (2009).

[85] H. Tanaka, K. Goto, M. Fujisawa, T. Oho, and Y. Uwatoko, *Physica* B, **329-333**, 697 (2003).

[86] K. Goto, M. Fujisawa, H. Tanaka, Y. Uwatoko, A. Oosawa, T. Osakabe, and K. Kakurai, *J. Phys. Soc. Jpn.* **75**, 064703 (2006).

[87] K. Goto, T. Osakabe, K. Kakurai, Y. Uwatoko, A. Oosawa, J. Kawakami, and H. Tanaka, *J. Phys. Soc. Jpn.* **76**, 053704 (2007).

[88] Y. Shindo and H. Tanaka, *J. Phys. Soc. Jpn.* **73**, 2642 (2004).

[89] R. Yu, L. Yin, N. S. Sullivan, J. S. Xia, C. Huan, A. Paduan-Filho, N. F. Oliveira Jr, S. Haas, A. Steppke, C. F. Miclea, F. Weickert, R. Movshovich, E.-D. Mun, B. L. Scott, V. S. Zapf, and T. Roscilde, *Nature* **489**, 379 (2012).

[90] A. Paduan-Filho, *Brazilian J. Phys.* **42**, 292 (2012).

[91] M. H. W. Chan, K. I. Blum, S. Q. Murphy, G. K. S. Wong, and J. D. Reppy, it Phys. Rev. Lett. **61**, 1950 (1988).

[92] H. Manaka, I. Yamada, H. Mitamura, and T. Goto, *Phys. Rev.* B, **66**, 064402 (2002).

[93] M. R. Andrews, D. M. Kurn, H.-J. Miesner, D. S. Durfee, C. G. Townsend, S. Inouye, and W. Ketterle, *Phys. Rev. Lett.* **79**, 553 (1997).

[94] V. I. Yukalov, *Laser Physics* **19**, 1 (2009).

[95] T. Roscilde and S. Haas, *J. Phys.* B, **39**, 153 (2006).

[96] T. Hong, A. Zheludev, H. Manaka, and L.-P. Regnault, *Phys. Rev.* B, **81**, 060410 (2010).

[97] G. M. Falco, T. Nattermann, and V. L. Pokrovsky, *Phys. Rev.* B, **80**, 104515 (2009).

[98] D. Jaksch and P. Zoller, *Ann. Phys.* (N.Y.) **315**, 52 (2005).

[99] O. Morsch and M. Oberthaler, *Rev. Mod. Phys.* **78**, 179 (2006).

[100] C. Moseley, O. Fialko, and K. Ziegler, *Ann. Phys.* **17**, 561 (2008).

[101] I. Bloch, J. Dalibard, and W. Zwerger, *Rev. Mod. Phys.* **80**, 885 (2008).

[102] J.K. Freericks and H. Monien, *Phys. Rev.* B, **53**, 2691 (1996).

[103] N. Elstner and H. Monien, *Phys. Rev.* B, **59**, 12184 (1999).

[104] S. Wessel, F. Alet, M. Troyer, and G.G. Batrouni, *Phys. Rev.* A, **70**, 053615 (2004).

[105] B. Capogrosso-Sansone, N. V. Prokofiev, and B. V. Svistunov, *Phys. Rev.* B, **75**, 134302 (2007).

[106] B. Capogrosso-Sansone, S.G. Söyler, N. Prokofiev, and B. Svistunov, *Phys. Rev.* A, **77**, 015602 (2008).

[107] D.B. Dickerscheid, D. van Oosten, P.J. Denteneer, and H.T.C. Stoof, *Phys. Rev.* A, **68**, 043623 (2003).

[108] A. E. Meyerovich, *Phys. Rev.* A, **68**, 051602 (2003).

[109] L. I. Plimak, M. K. Olsen, and M. Fleischhauer, *Phys. Rev.* A, **70**, 013611 (2004).

[110] F. Gerbier, *Phys. Rev. Lett.* **99**, 120405 (2007).

[111] V.I. Yukalov and E.P. Yukalova, *Phys. Rev.* A, **78**, 063610 (2008).

[112] V.I. Yukalov and E.P. Yukalova, *Phys. Lett.* A, **373**, 1301 (2009).

[113] F.A. Buot, *Phys. Rep.* **234**, 73 (1993).

[114] K.P. Marzlin and V.I. Yukalov, *Eur. Phys.* J. D **33**, 253 (2005).

[115] V.O. Nesterenko, A.N. Novikov, F.F. de Souza Cruz, and E.L. Lapolli, *Laser Phys.* **19**, 616 (2009).

[116] L.Y. Yang, L.B. Fu, and J. Liu, *Laser Phys.* **19**, 678 (2009).

[117] V.I. Yukalov, E.P. Yukalova, and V.S. Bagnato, *Laser Phys.* **19**, 686 (2009).

[118] A. Zenesini, H. Lignier, C. Sias, O. Morsch, D. Ciampini, and E. Arimondo, *Laser Phys.* **20**, 1182 (2010).

[119] V.I. Yukalov, *Laser Phys. Lett.* **7**, 467 (2010).

[120] D.I. Pushkarov, *Quasiparticle Theory of Defects in Solids* (World Scientific, Singapore, 1991).

[121] N.N. Bogoliubov, *Lectures on Quantum Statistics* (Gordon and Breach, New York, 1970), Vol. 2.

[122] V.I. Yukalov and E.P. Yukalova, *Phys. Rev.* A, **76**, 013602 (2007).

[123] N.M. Hugenholtz and D. Pines, *Phys. Rev.* **116**, 489 (1959).

[124] I. Danshita and P. Naidon, *Phys. Rev.* A, **79**, 043601 (2009).

[125] F. Cinty, P. Jain, M. Boninsegni, A. Micheli, P. Zoller, and G. Pupillo, *Phys. Rev. Lett.* **105**, 135301 (2010).

[126] F. Dalfovo, S. Giorgini, L. P. Pitaevskii, and S. Stringari, *Rev. Mod. Phys.* **71**, 463 (1999).

[127] Yu. Kagan, E. L. Surkov, and G. V. Shlyapnikov, *Phys. Rev. Lett.* **79**, 2604 (1997).

[128] S. L. Cornish, N. R. Claussen, J. L. Roberts, E. A. Cornell, and C. E. Wieman, *Phys. Rev. Lett.* **85**, 1795 (2000).

[129] F. Kh. Abdullaev, J. G. Caputo, R. A. Kraenkel, and B. A. Malomed, *Phys. Rev.* A, **67**, 013605 (2003).

[130] Y. Kagan, A.E. Muryshev, and G.V. Shlyapnikov, *Phys. Rev. Lett.* **81**, 933 (1998).

[131] C.A. Sackett, H.T.C. Stoof, and R.G. Hulet, *Phys. Rev. Lett.* **80**, 2031 (1998).

[132] C. Sulem and P. L. Sulem, The Nonlinear Schrödinger Equation: Self-Focusing and Wave Collapse (Applied Mathematical Sciences) Springer, NY (1999).

[133] L. Bergé, *Phys. Rep.* **303**, 259 (1998).

[134] E.I. Rashba, in *Modern Problems in Condensed Matter Sciences* Vol. 2 (Eds. V. M. Agranovich and A. A. Maradudin) p. 543 (Amsterdam, Notrh-Holland, 1982).

[135] M. Ueda and A. J. Leggett, *Phys. Rev. Lett.* **80**, 1576 (1998).

[136] Y.-J. Lin, R. L. Compton, K. Jiménez-Garcia, J. V. Porto, and I. B. Spielman, *Nature* **462**, 628 (2009).

[137] C. Wang, C. Gao, C.-M. Jian, and H. Zhai, *Phys. Rev. Lett.* **105**, 160403 (2010).

[138] Y.-J. Lin, K. Jiménez-García, and I. B. Spielman, *Nature* **471**, 83 (2011).

[139] H. Zhai, *Int. J. Mod. Phys. B* **26**, 1230001 (2012).

[140] V. Galitski and I. B. Spielman, *Nature* **494**, 49 (2013).

[141] A. M. Dudarev, R. B. Diener, I. Carusotto, and Q. Niu, *Phys. Rev. Lett.* **92**, 153005 (2004).

[142] K. Osterloh, M. Baig, L. Santos, P. Zoller, and M. Lewenstein, *Phys. Rev. Lett.* **95**, 010403 (2005).

[143] J. Ruseckas, G. Juzeliūnas, P. Öhberg, and M. Fleischhauer, *Phys. Rev. Lett.* **95**, 010404 (2005).

[144] G. Juzeliūnas, J. Ruseckas, and J. Dalibard, *Phys. Rev.* A, **81**, 053403 (2010).

[145] T.-L. Ho and S. Zhang, *Phys. Rev. Lett.* **107**, 150403 (2011).

[146] Y. Li, G. Martone and S. Stringari, EPL **99**, 56008 (2012).

[147] G. Martone, Y. Li, L. P. Pitaevskii, and S. Stringari, *Phys. Rev.* A, **86**, 063621 (2012).

[148] B. M. Anderson, G. Juzeliūnas, V. M. Galitski, and I. B. Spielman, *Phys. Rev. Lett.* **108**, 235301 (2012).

[149] J.-Y. Zhang S.-C. Ji, Z. Chen, L. Zhang, Z.-D. Du, B. Yan, G.-S. Pan, B. Zhao, Y.-J. Deng, H. Zhai, S. Chen, and J.-W. Pan,*Phys. Rev. Lett.* **109**, 115301 (2012).

[150] Y. Zhang, L. Mao, and Ch. Zhang, *Phys. Rev. Lett.* **108**, 035302 (2012).

[151] X.-J. Liu, M. F. Borunda, X. Liu, and J. Sinova, *Phys. Rev. Lett.* **102**, 046402 (2009).

[152] P. Wang, Z.-Q. Yu, Z. Fu, J. Miao, L. Huang, Sh. Chai, H. Zhai, and J. Zhang, *Phys. Rev. Lett.* **109**, 095301 (2012).

[153] L. W. Cheuk, A. T. Sommer, Z. Hadzibabic, T. Yefsah, W. S. Bakr, and M. W. Zwierlein, *Phys. Rev. Lett.* **109**, 095302 (2012).

[154] M. Iskin and A. L. Subasi, *Phys. Rev.* A, **87**, 063627 (2013).

[155] T. Ozawa and G. Baym, *Phys. Rev. Lett.* **109**, 025301 (2012).

[156] R. Barnett, S. Powell, T. Graß, M. Lewenstein, and S. Das Sarma, *Phys. Rev.* A, **85**, 023615 (2012).

[157] S. Sinha, R. Nath, and L. Santos, *Phys. Rev. Lett.* **107**, 270401 (2011).

[158] C. Chin, R. Grimm, P. Julienne, and E. Tiesinga, *Rev. Mod. Phys.* **82**, 1225 (2010).

[159] E. N. Adams and E. I. Blount, *J. Phys. Chem. Solids* **10**, 286 (1959).

[160] N.R. Cooper, *Advances in Physics* **57**, 539 (2008).

[161] I. V. Tokatly and E. Ya. Sherman, *Phys. Rev.* B, **82**, 161305 (2010).

[162] D. L. Campbell, G. Juzeliunas, and I. B. Spielman, *Phys. Rev.* A, **84**, 025602 (2011).

[163] Y. Castin and J. Dalibard, *Phys. Rev.* A, **55**, 4330 (1997).

[164] M. R. Andrews, C. G. Townsend, H.-J. Miesner, D. S. Kurn, D. M. Durfee, and W. Ketterle, *Science*, **275**, 637 (1997).

[165] Y. B. Band, *J. Phys. Chem.* B, **112**, 16097 (2008).

[166] G. R. Allckok, *Ann. Phys.(NY)* **53**, 253, 286, 311 (1969).

[167] A. J. Bracken and G. F. Melloy, *J. Phys. A: Math. Gen*, **27**, 2197 (1994).

[168] J. G. Muga, J. P. Palao, and R. Sala, *Phys. Lett.* A, **238**, 90 (1998).

[169] J. G. Muga and C. R. Leavens, *Phys. Rep.*, **338**, 353 (2000).

[170] J. A. Damborenea, I. L. Egusquiza, G. C. Hegerfeldt, and J. G. Muga, *Phys. Rev.* A, **66**, 052104 (2002).

[171] M. V. Berry, *J. Phys. A: Math. Theor.*, **43**, 415302 (2010).

[172] J. M. Yersley, J. J. Halliwell, R. Hartshorn, and A. Whitby, *Phys. Rev.* A, **86**, 042116 (2012).

[173] M. Palmero, E. Torrontegui, J. G. Muga, and M. Modugno, *Phys. Rev.* A, **87**, 053618 (2013).

[174] L. S. Levitov and E. I. Rashba, *Phys. Rev.* B, **67**, 115324 (2003).

[175] Yu. V. Pershin, A. James, J. A. Nesteroff, and V. Privman, *Phys. Rev.* B, **69**, 121306(R) (2004).

[176] M. M. Glazov and E. Ya. Sherman, *Phys. Rev. Lett.*, **107**, 156602 (2011).

[177] Ch. Qu, Ch. Hamner, M. Gong, Ch. Zhang, and P. Engels, *Phys. Rev.* A, **88**, 021604 (2013).

[178] T. Byrnes, K. Wen, and Y. Yamamoto, *Phys. Rev.* A, **85**, 040306 (2012).

[179] K. C. Nowack, F. H. L. Koppens, Yu. V. Nazarov, and L. M. K. Vandersypen, *Science*, **318**, 1430 (2007).

[180] E. I. Rashba and Al. L. Efros, *Phys. Rev. Lett.*, **91**, 126405 (2003).

[181] R. Li, J. Q. You, C. P. Sun. and F. Nori, *Phys. Rev. Lett.*, **111**, 086805 (2013).

[182] E. Ya. Sherman and D. Sokolovski, *New J. Phys.*, **16**, 015013 (2014).

[183] D. V. Khomitsky, L. V. Gulyaev, and E. Ya. Sherman, *Phys. Rev.* B, **85**, 125312 (2012).

[184] M. Bukov L. D'Alessio, and A. Polkovnikov, arXiv:1407.4803.

[185] J. A. Budagosky and A. Castro, *J. Phys.* B*: At. Mol. Opt. Phys.* **88** 15 (2015).

[186] B. Xiong, J.-H. Zheng, and D.-W. Wang in arXiv:1410.8444

[187] M. A. Garcia-March, G. Mazzarella, L. Dell'Anna, B. Juliá-Díaz, L. Salasnich, and A. Polls, *Phys. Rev.* A, **89**, 063607 (2014);

[188] R. Citro and A. Naddeo, arXiv:1405.5356

[189] Ch. Skokos, D. O. Krimer, S. Komineas, and S. Flach, *Phys. Rev.* E **79**, 056211 (2009).

[190] L. Zhou, H. Pu, and W. Zhang, *Phys. Rev.* A, **87**, 023625 (2013).

"Learn from yesterday, live for today, hope for tomorrow.
The important thing is to not stop questioning."

Albert Einstein